JANUARI 2004 ECN-C--04-009

# Final Report MissionN & Miracle

# Micro Crystalline Silicon in the Netherlands, Novem projects 146.120-025 and 146.120-018

W.J. Soppe, C. Devilee, A.C.W. Biebericher, C. Smit (TU Delft), R.A.C.M.M. van Swaaij (TU Delft), I. Houston (TU Eindhoven), M.C.M. van de Sanden (TU Eindhoven), A. Gordijn (Universiteit Utrecht), J.K. Rath (Universiteit Utrecht), R.E.I Schropp (Universiteit Utrecht), H. Donker (TU Delft), A. Goossens (TU Delft)

# Verantwoording

Dit is het Eindrapport van de Novem-projecten 146.120-025 en 146.120-018-3 en beschrijft de resultaten behaald in de periode van 1 juli 2001 tot 1 juli 2003 binnen de projecten MissionN en Miracle.

## Distributie

Novem	1-3
A.B.M. Hoff	4
C.A.M. van der Klein	5
G.P. Wyers	6
J.H. Bultman	7
W.J. Soppe	8
C. Devilee	9
A.C.W. Biebericher	10
C. Smit, TU Delft	11
R.A.C.M.M. van Swaaij, TU Delft	12
I. Houston, TU Eindhoven	13
M.C.M. van de Sanden, TU Eindhoven	14
A. Gordijn, Universiteit Utrecht	15
R.E.I. Schropp, Universiteit Utrecht	16
H. Donker, TU Delft	17
A. Goossens, TU Delft	18
Centraal archief	19
Archief ECN Zonne-energie	20-23

# Authorisatie

	Name	Signature	Date
Gecontroleerd	A.C. Veltkamp		14/01/2004
Goedgekeurd	A.C. Veltkamp		14/01/2004
Geauthoriseerd	G.P. Wyers		14/01/2004

## Samenvatting

Dit rapport vormt een verslaglegging van onderzoekswerk dat in het kader van de projecten MissionN en Miracle is uitgevoerd aan de ontwikkeling van nieuwe depositiemethoden van micro-kristallijn silicium ( $\mu$ c-Si). Dit werk is verricht op een vijftal verschillende locaties: TU-Eindhoven, Dimes-Delft, TAC-Delft, Universiteit Utrecht en ECN. Er zijn twee nieuwe depositiemethoden voor het maken van intrinsieke  $\mu$ c-Si lagen voor zonnecellen onderzocht: Expanding Thermal Plasma (ETP) en Microwave Plasma Enhanced Chemical Vapour Deposition MWPECVD. Voor beide methoden is aangetoond dat snelle groei (> 1 nm/s) van  $\mu$ c-Si mogelijk is. In dit project is echter vooralsnog gebleken dat deze snelle groei voor beide systemen gepaard gaat met een te hoge porositeit van de  $\mu$ c-Si lagen, waardoor de vereiste elektronische kwaliteit van de lagen nog niet is behaald. De rendementen van de cellen die met i-lagen gefabriceerd met een van deze beide methoden zijn gemaakt hebben daarom ook niet de project doelstelling (8 %) bereikt maar zijn blijven steken op 1.9 % en 0.5 % voor respectievelijk ETP en MWPECVD. De met MWPECVD gegroeide lagen hebben hierbij extra te lijden gehad van post-oxidatie door vacuümonderbreking daar de verschillende lagen van de cel op verschillende locaties moesten worden gemaakt.

Op succesvolle wijze is een nieuwe, en effectievere methode voor het groeien van gedoteerde (n, p) µc-Si lagen ontwikkeld: de "layer by layer" (LBL) methode. Hiermee kunnen over een breed temperatuurgebied (van 150 tot 400 °C) gedoteerde µc-Si lagen worden gegroeid met een veel hogere dopingefficiency dan de conventionele continue depositie methode.

Het onderzoek naar het groeimechanisme van  $\mu$ c-Si met ATR-FTIR en spectrale ellipsometrie heeft aangetoond dat de depositie van  $\mu$ c-Si altijd begint met een amorfe kiemlaag (ook als het substraat een kristallijn-Si wafer is). De amorfe kiemlaag gaat via een gemengde a-Si/ $\mu$ c-Si tussenlaag over in een volledig  $\mu$ c-Si laag. Diktes van de kiemlaag en gemengde tussenlaag worden beinvloed door verhouding van de procesgassen SiH<sub>4</sub> en H<sub>2</sub>. De substraat temperatuur heeft slechts een gering effect op de uiteindelijke kristalfractie van de laag.

Het werk aan nieuwe karakteriseringstechnieken van μc-Si heeft een aantal veelbelovende methoden opgeleverd (Transient Absorption Spectroscopy, Time of Flight measurements), die in de toekomst zullen worden ingezet voor analyse van μc-Si.

# **CONTENTS**

SUMM	IARY	7
1.	INTRODUCTION	9
2. 2.1 2.2 2.3 2.4 2.5 2.6 2.7 2.8 2.9 2.10	MICROWAVE PECVD Overview of depositions of µc-Si layers by MWPECVD Optical Emission Spectroscopy Thickness homogeneity Solar cells Vacuum-break experiment Dark conductivity FTIR SIMS measurements Conclusions Publications and Presentations	11 11 14 18 19 22 23 25 27 28 29
3. 3.1 3.2 3.3 3.4 3.5 3.6 3.7 3.8 3.9 3.10	CHARACTERISATION OF SI LAYERS DEPOSITED BY ETP Introduction Initial characterisation of material Spectroscopic Ellipsometry Amorphous silicon Microcrystalline silicon ATR-FTIR Construction of new deposition setup Future work Publications Presentations	31 31 33 34 35 39 40 40 41 41
4.1 4.2 4.3 4.4	MICROCRYSTALLINE SILICON FILMS AND SOLAR CELLS DEPOSITED BY ETP Introduction and aim Experimental Results on ETP microcrystalline silicon layers Results on ETP microcrystalline silicon solar cells	43 44 44 45 48
5. 5.1 5.2 5.3 5.4	CHARACTERIZATION OF µC-SI Introduction Raman / Photoluminescence spectroscopy Transient Absorption spectroscopy Time of Flight measurements	51 51 51 53 54
6. 6.1 6.2 6.3 6.4 6.4.1	LBL DEPOSITIONS OF DOPED MICROCRYSTALLINE SI LAYERS Introduction Development of the µc-Si doped layers Applications in Solar cells Characterization: Collaboration with partners PDS 61	57 57 57 60 61
6.4.2 6.4.3 6.4.4 6.5 6.6 6.7	Raman spectroscopy Electrical conductivity Optical properties Characterization of cells Comparison of ETP and MWPECVD cells with reference cells and advice: Published/presented articled related to this projects:	62 63 63 63 63
7	CONCLUSIONS	65

ECN-C--04-009 5

APPENDIX A	DEPOSITION OF HYDROGENATED MICROCRYSTALLINE SILICON AT GROWTH RATES IN EXCESS OF 1 NM/S USING THE	
	EXPANDING THERMAL PLASMA TECHNIQUE	67
APPENDIX B	DEPO 2 SPECIFICATIES	95

#### **SUMMARY**

This report summarizes results obtained in the projects MissionN and Miracle, on the development of new deposition methods for microcrystalline silicon ( $\mu$ c-Si). The research has been carried out on five different locations in the Netherlands: TU-Eindhoven, Dimes-Delft, TAC-Delft, Utrecht University and ECN. Two new deposition methods for growth of intrinsic  $\mu$ c-Si layers for solar cell applications have been investigated: Expanding Thermal Plasma (ETP) and Microwave Plasma Enhanced Chemical Vapour Deposition MWPECVD. For both methods it is shown that fast growth (> 1 nm/s) of  $\mu$ c-Si is possible. In this project however, it has been found that these high growth rates are accompanied with high porosity of the layers. As a result the required electronic quality of  $\mu$ c-Si for solar cell application has not been obtained yet. Efficiencies of cells with i-layers deposited by one of these methods did not meet the project aim of 8% but were limited to 1.9 % and 0.5 % for respectively ETP and MWPECVD. Cells made with MWPECVD grown i-layers suffered extra from post oxidation resulting from vacuum interruption since different layers of these cells had to be manufactured at different locations.

A new and more effective method for deposition of doped  $\mu$ c-Si layers was developed successfully: the Layer-by-Layer method. With this method doped layers can be made in a wide temperature regime (150 - 400 °C), with a much higher doping efficiency than by the conventional continuous deposition method.

Research on the growth mechanisms of  $\mu$ c-Si by ATR-FTIR and spectral ellipsometry has shown that deposition of  $\mu$ c-Si always starts with an amorphous incubation layer (even when a crystalline Si wafer is used as substrate). The amorphous incubation layer continues into an a-Si/ $\mu$ c-Si mixed layers and then continues into an almost full crystalline  $\mu$ c-Si layer. Thicknesses of incubation and mixed layer can be controlled by the ratio of SiH<sub>4</sub> and H<sub>2</sub>. The substrate temperature has little or no effect on the final crystal fraction of the layer.

Work on development of new and advanced characterization tools for  $\mu$ c-Si has yielded some promising methods: (Transient Absorption Spectroscopy and Time of Flight measurements) which will be applied in future for analysis of  $\mu$ c-Si.

#### 1. INTRODUCTION

Microcrystalline silicon ( $\mu$ c-Si) is receiving much interest from the PV community because this material can be fabricated as thin layers at low temperatures. In solar cells, the material does not suffer from degradation like amorphous silicon does. In the past few years, solar cells and modules, based on microcrystalline silicon layers, have been made both on laboratory scale [1,2,3] and on pilot production scale [4]. A severe handicap for a large-scale production of solar cells based on  $\mu$ c-Si is that with conventional deposition techniques such as, e.g., RF-PECVD the growth rate of the intrinsic Si layer is unacceptably low. Alternative techniques, which enable larger growth rates such as VHF-PECVD, have the disadvantage that it is more difficult to obtain homogeneous deposition on large areas.

In the projects MissionN and Miracle we investigate two new deposition techniques – Expanding Thermal Plasma (Delft and Eindhoven) and Microwave PECVD (Petten) – which should enable both large deposition rates of intrinsic  $\mu$ c-Si and homogeneous deposition on large areas.

The aim of the projects is to evaluate the potential of these deposition techniques for growing intrinsic  $\mu$ c-Si layers with device quality. The quality the  $\mu$ c-Si layers has to be proven finally by incorporating them in solar cells that should have an efficiency of at least 8 %.

Complementary to these activities, work will be carried out in Utrecht to improve the quality of  $\mu$ c-Si p- and n-layers by the Layer By Layer (LBL) deposition technique, and in Delft to develop new characterization techniques.

ECN-C--04-009

<sup>[1]</sup> J. Meier et al., J. of Non-Cryst. Sol. 227-230, 1250 (1998).

<sup>[2]</sup> O. Vetterl et al., Solar Energy Mat. Sol. Cells 62, 97 (2000).

<sup>[3]</sup> K. Saito, et al., Proc. of the 2nd World Conf. on Photovoltaic Solar Energy Conversion, Vienna, 1998, p. 351.

<sup>[4]</sup> K. Yamamoto et al., Proc. of the 26 IEEE Photovoltaic Specialists Conference, Anaheim, 1997, p. 575.

#### 2. MICROWAVE PECVD

A.C.W. Biebericher, C. Devilee and W. Soppe, ECN

## 2.1 Overview of depositions of µc-Si layers by MWPECVD

In the first year of the project we have shown that by using microwave PECVD, it is possible to grow microcrystalline Si layers at low temperatures with sufficient high deposition rates (>1 nm/s) and with sufficient high crystallinity. Growth rate increases and crystal fraction decreases with increasing SiH<sub>4</sub>/H<sub>2</sub> ratio (see *Figure 2-1*), so in practice one has to find a balance between these two requirements.

During the second year of the project there was a strong focus on improvement of the electronic quality of the silicon layers. Emphasis was put on reduction of the oxygen concentration of deposited films both during deposition and after deposition (post oxidation) and on reduction of the general defect density. Oxygen contamination of the deposited layers is determined by FTIR analysis and by dark conductivity measurements, whereas the general defect density is determined by optical subbandgap absorption (typically at 0.8 eV).

In order to reduce oxygen contamination during the depositions, we reduced the leak rate of the deposition chamber (to less than 1E-03 mbar l/s), and installed gas purifiers in the process gas lines (which reduce  $O_2$  and  $H_2O$  to less than 1 ppm).

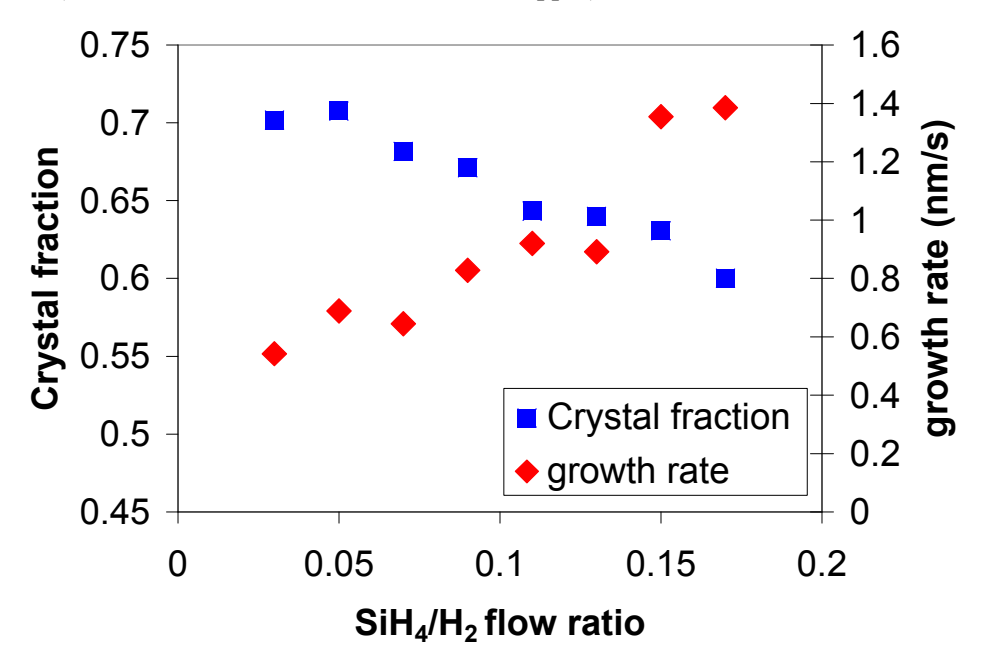


Figure 2-1: Crystal fraction (obtained from Raman spectroscopy) and growth rate for various  $SiH_4/H_2$  flow ratios.  $T_{substrate} = 250$  °C; p = 0.1 mbar.

In Figure 2-2, an overview of deposition rates  $r_d$  and crystalline fractions of layers grown in the second year of the project is shown. Note that these data comprise a large number of different deposition conditions (temperature, pressure, total flow, flow ratios). The silicon layers were deposited on sheets of alkaline-free glass (Schott AF45). All depositions were preceded by deposition of a thin seed layer (5 min. flow ratio SiH<sub>4</sub>/H<sub>2</sub> equal to 0.01) to reduce the amorphous incubation phase. The figure shows that  $\mu$ c-Si with high crystalline fraction can be obtained for a broad range of deposition rates.

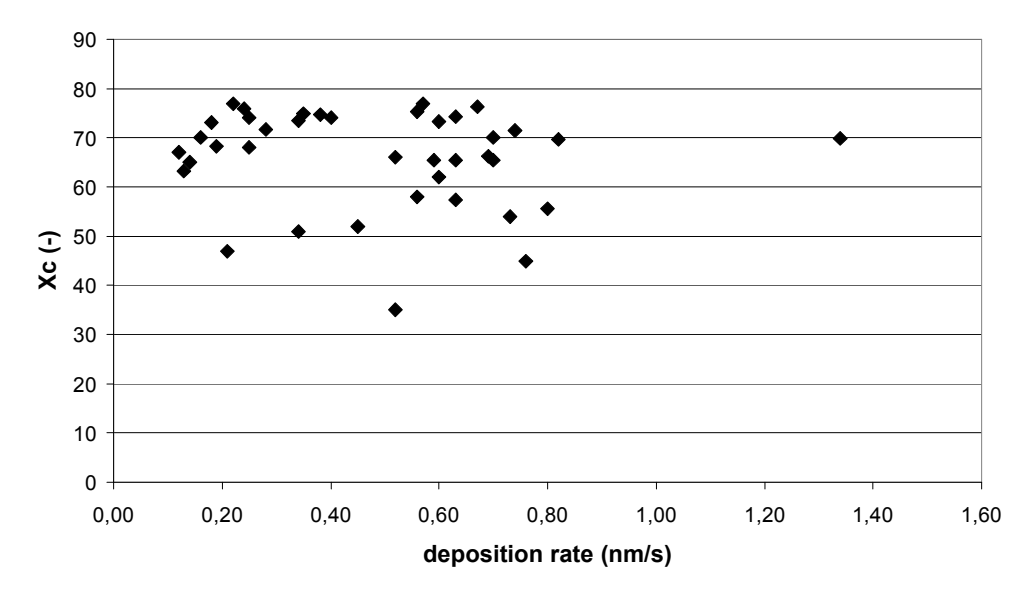


Figure 2-2: Overview over the crystalline fraction  $X_c$  as a function of the deposition rate for depositions under various conditions.

Rapid post-oxidation of the silicon layers is primarily due to porosity of the layers. We have found evidence that porosity is related to the residence time of the process gases during deposition. The residence time is defined as  $\tau_{res} = V \times p/\Phi$ , where V is the volume of the deposition chamber, p is the pressure and  $\Phi$  is the total flow of the process gases. We estimate the net volume of the deposition chamber to be about 0.25 m³. With  $\Phi = 200$  sccm, and p = 0.1 mbar, the residence time is about 7.5 s. The relation between porosity and residence time will be discussed later in this chapter, but in *Figure 2-3* we already show an overview of deposition rates  $r_d$  and crystalline fractions versus the residence time. It can be observed that the crystalline fraction and the deposition rate seem to be independent of the residence time, except for small values of  $\tau_{res}$ . The increase of  $r_d$  for small  $\tau_{res}$  can be attributed to two possible effects: 1) lower pressure leads to a wider plasma region around the quartz tube. This will increase the density of reactive H species in the region of the SiH<sub>4</sub> inlet and enhance the dissociation of SiH<sub>4</sub>, 2) shorter residence times enhance the probability of SiH<sub>3</sub> and H species, required for growth, to reach to substrate before they recombine.

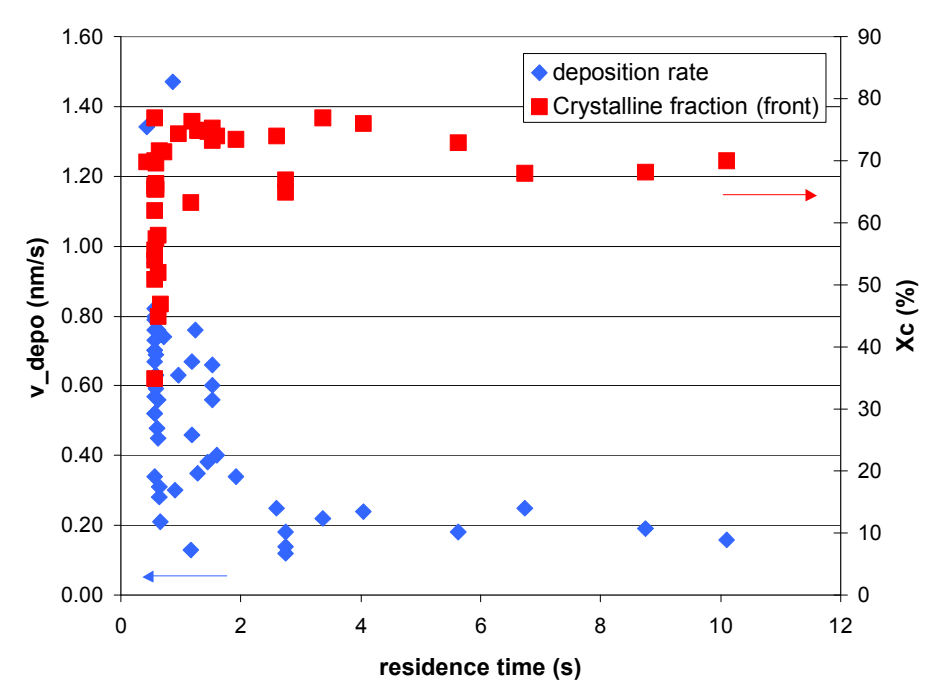


Figure 2-3: Overview over the deposition rate and the crystalline fraction determined at the front side of the layer, as a function of the residence time, for depositions performed under various conditions.

As shown in the figures above, it is possible to grow microcrystalline silicon with high deposition rates and high crystalline fractions. The crystalline fraction could be increased even further more if the seed layers could be improved. The crystalline fraction and the deposition rate are also slightly affected by the argon flow, which is added in some amount to obtain stable plasma, and the substrate temperature as shown in the figures below.

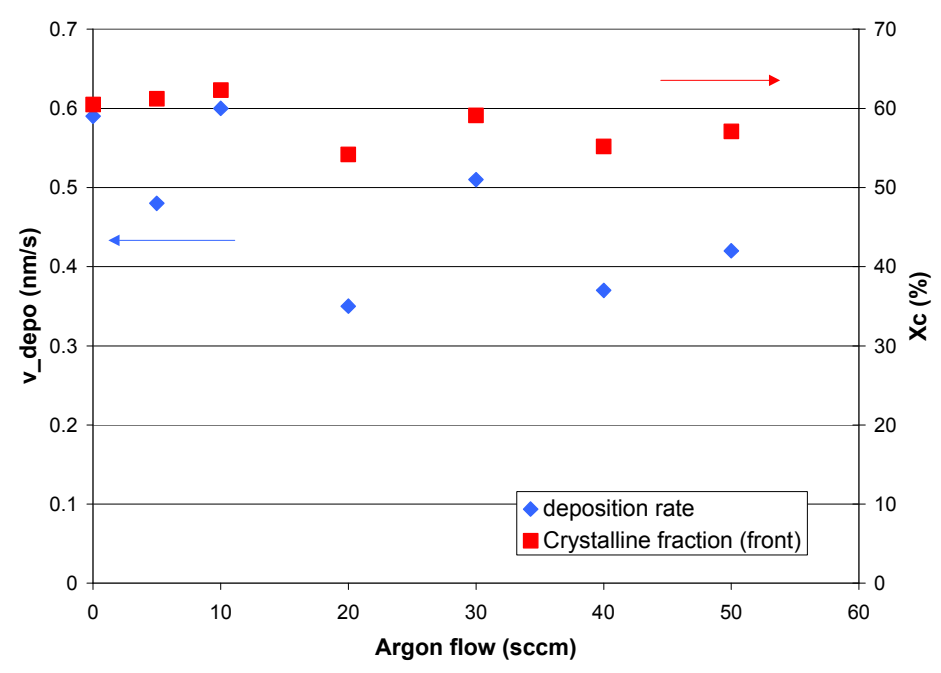


Figure 2-4: The effect of the argon flow on the deposition rate and the crystalline fraction on the front side of the layer. Deposition conditions:  $H_2$ =200 sccm,  $SiH_4$  = 18 sccm, p=0.1 mbar, T=250 °C, P=2´500 W.

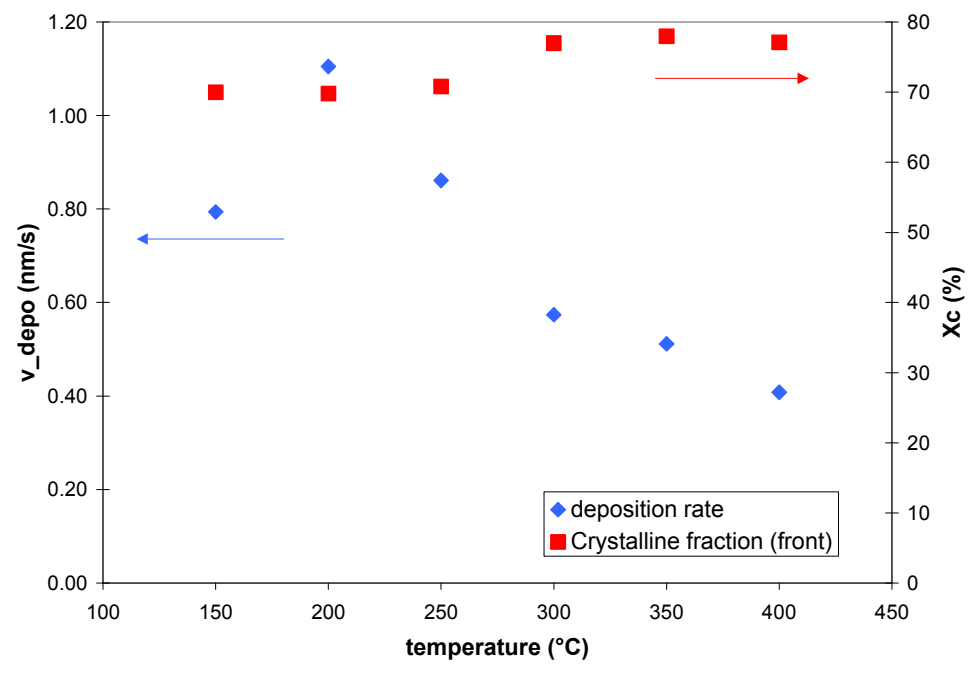


Figure 2-5: The effect of the substrate temperature on the deposition rate and the crystalline fraction at the front side of the layer.

## 2.2 Optical Emission Spectroscopy

We apply Optical Emission Spectroscopy (OES) in order to monitor certain plasma characteristics in situ. Most important features in spectrum from 200 to 900 nm are the Si\* peak at 288 nm, the SiH\* peak at 413 nm and the hydrogen Balmer peaks ( $H_{\alpha}$  at 656 nm and  $H_{\beta}$  at 486 nm) resulting from dissociation of the process gases SiH<sub>4</sub> and H<sub>2</sub>. Typical OES spectra are shown in *Figure 2-6*.

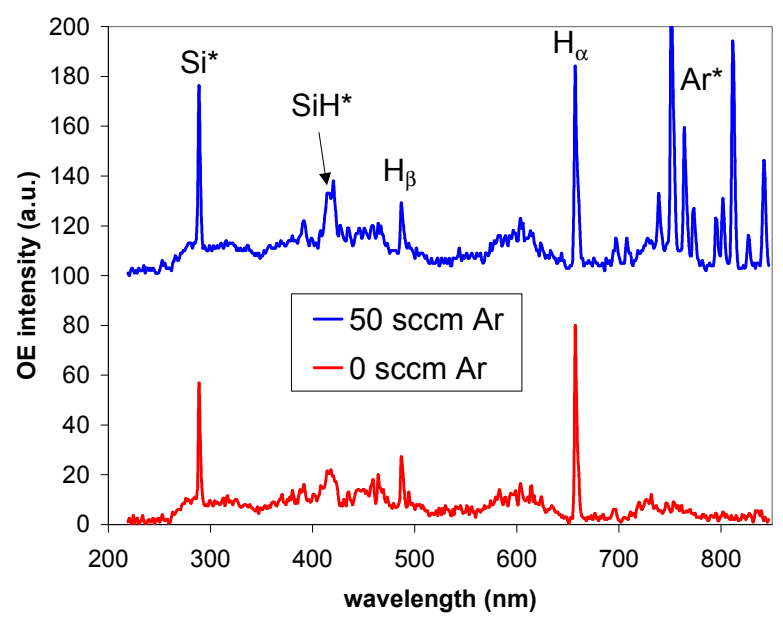


Figure 2-6: OES spectra of plasmas with and without Ar dilution.

For quantitative evaluation of the spectra it should be kept in mind that the emission intensity  $I_{\lambda}^{A}$  from a specific species A depends on its concentration [A] but also on other factors [5]:

$$I_1^A = a_1^A \bullet [A]$$
 where  $a_1^A = K \int_0^\infty Q(p, n_e) s_1^A(e) N_e(e) de$  (1)

Where K = a constant depending on the sensitivity of the detector,

 $S_1^A = cross$  section for excitation of the emitting species to a given excited state caused by an electron of energy  $\varepsilon$ ,

 $N_e$  = number of electrons in the energy range de present in the volume of the reactor viewed by the detector,

 $Q(p,n_e)$  = quantum yield for emission from the given excited state as a function of discharge pressure and electron density.

In the second year of the project the position of the view port for OES has been relocated. Originally the view port was located at the front side of the deposition chamber at a distance of approximately 40 cm of the plasma source. The new position at the left side of the reactor chamber is located 20 cm of the plasma source, which results in a more intense spectrum. In *Figure 2-7* the OES system is depicted. Only photons emitted from just above the substrate surface are collected now with the system. The second improvement for OES was the replacement of the kodial glass view port by a sapphire view port, which has a higher transmission in the UV regime. This was important for improved measurements of one of the dominant peaks in the OES spectra: the Si\* peak at 288 nm.

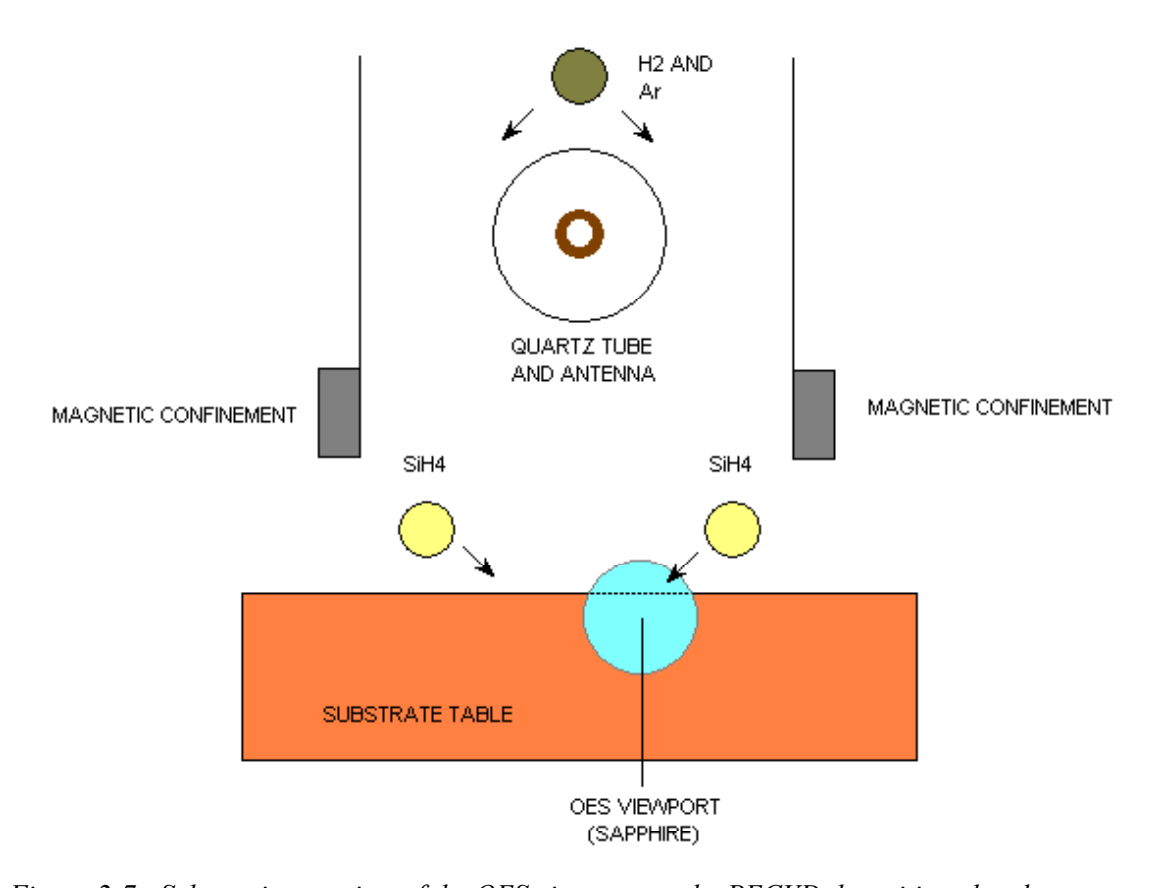


Figure 2-7: Schematic overview of the OES view port at the PECVD deposition chamber.

Several measurements for the investigation of the deposition parameters and their interactions have been obtained, along with OES measurements of the individual depositions. The main results of these measurements are shown in *Figure 2-8a-d* and in *Figure 2-9*.

<sup>[5].</sup> A. Grill, Cold Plasma in Materials Fabrication, IEEE Press, Piscataway, USA, 1994

#### General trends are:

- SiH\* and Si\* emission intensities increase with increasing SiH<sub>4</sub>/H<sub>2</sub> fractions,
- SiH\* and Si\* emission intensities attain the highest levels for small residence times, probably because the electron density  $N_e$  at the substrate level is higher for lower pressures (this will be discussed in Section 2.3)
- Emission intensities of the species SiH\*, Si\*,  $H_{\alpha}$  and  $H_{\beta}$  seem to be independent of the pressure. Apparently the decrease of the species [A] (see equation 1) at lower pressures is compensated by the increase of the electron density  $N_e$  at the substrate level such that the product remains constant.
- Emissions of Si\* and  $H_{\alpha}$  have a minimum for substrate temperature between 100-300 °C, where emission of SiH\* and  $H_{\beta}$  seem independent of the substrate temperature.

Fig. 2.8-a

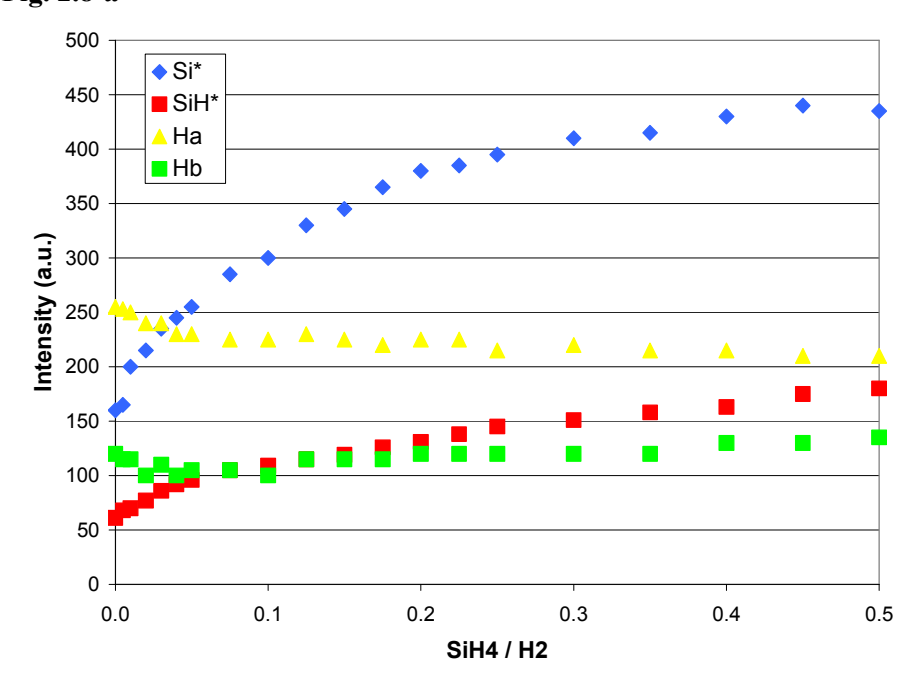
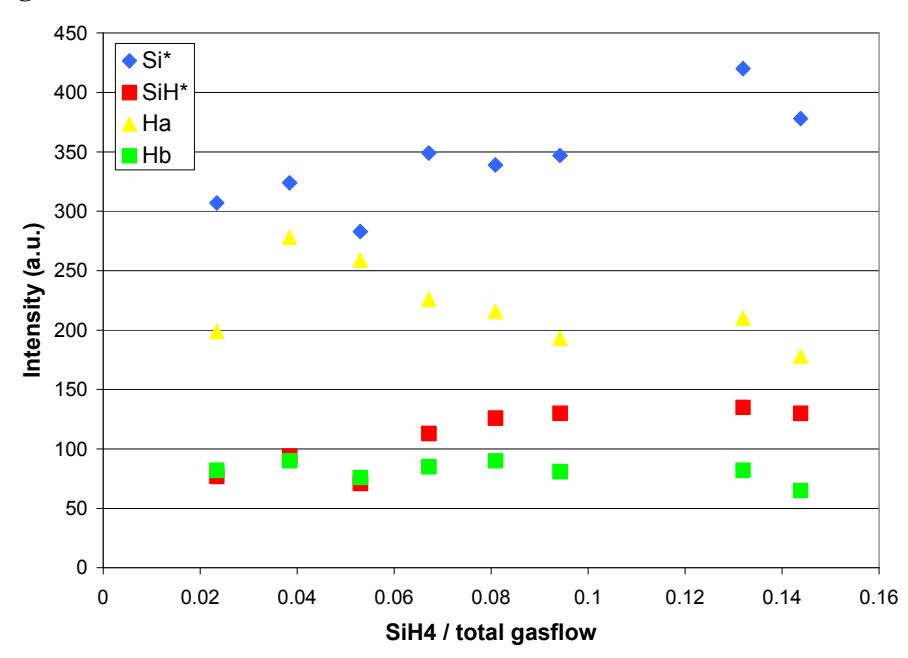
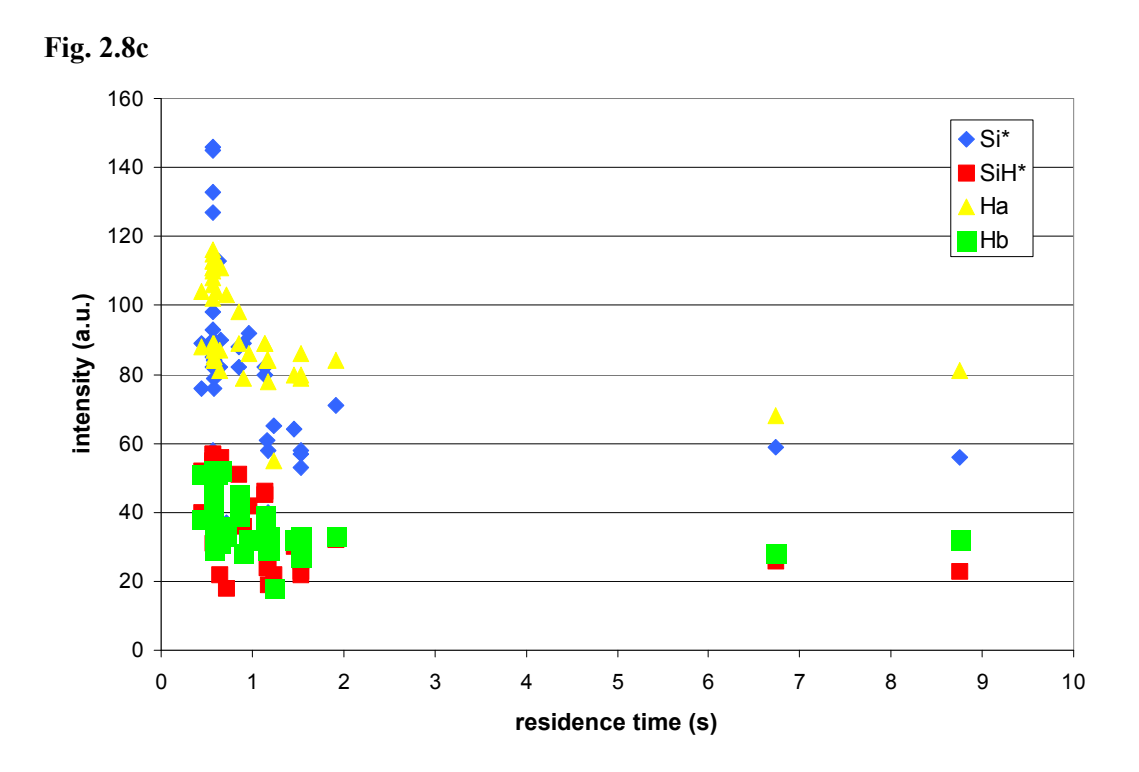


Fig. 2.8b





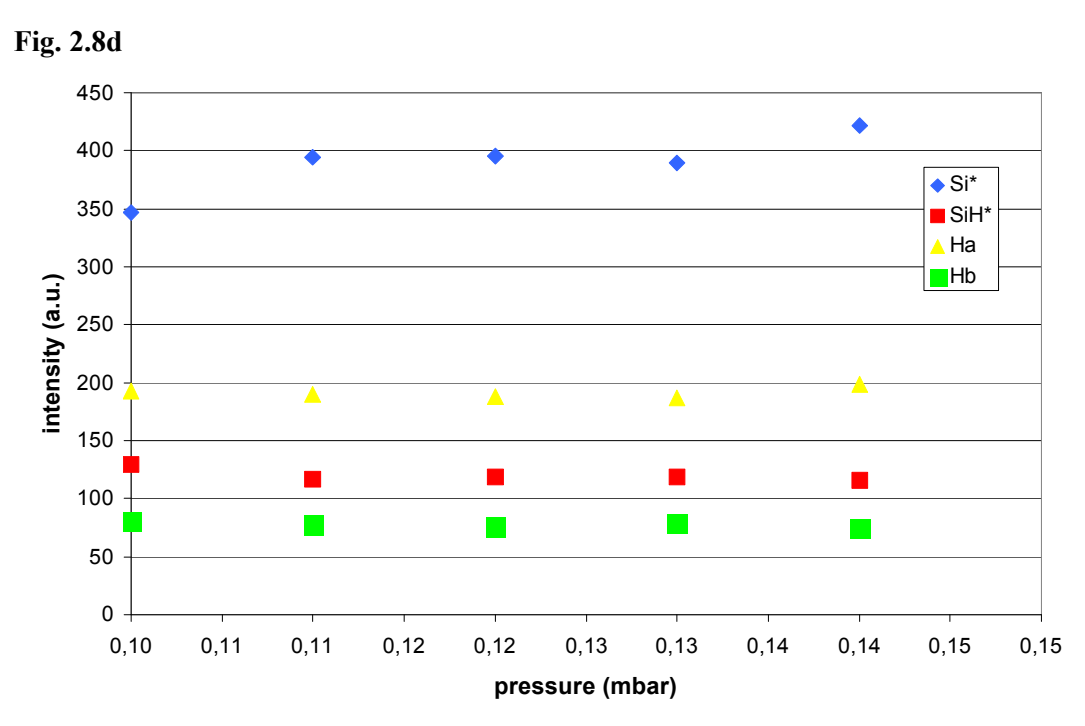


Figure 2-8: Peak intensity of the dominant peaks in the OES spectra as a function of the SiH4/H2 ratio (a), silane dilution (b), residence time and pressure (d).

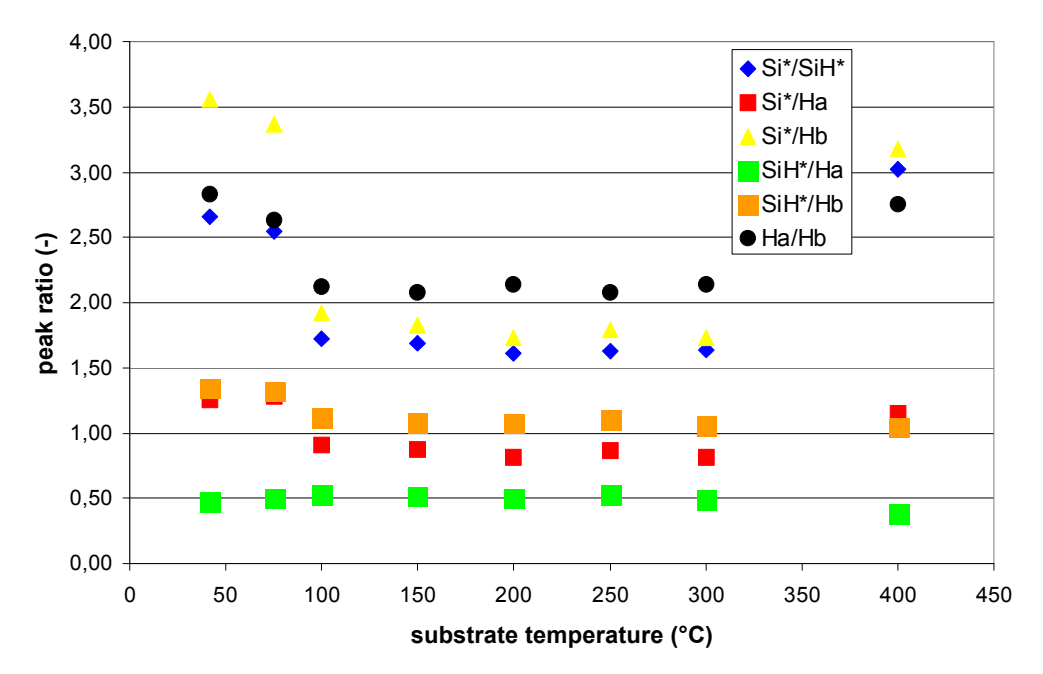


Figure 2-9: Peak ratio from OES spectra as a function of substrate temperature.

### 2.3 Thickness homogeneity

One of the goals of this research was to deposit homogeneous on large areas. The following picture shows the results of multi-probe measurements performed on a hydrogen plasma in the in-line reactor.

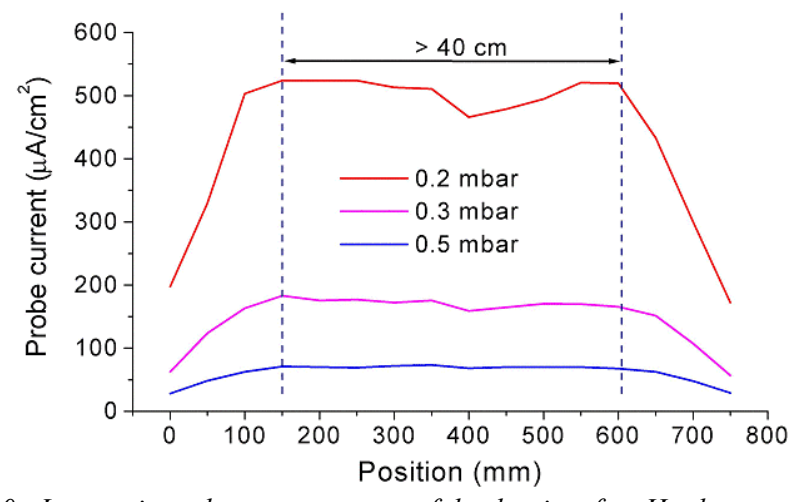


Figure 2-10: Langmuir probe measurements of the density of an  $H_2$  plasma at substrate level. The power is 2000 W.

The probe current represents the plasma density at substrate level. It is clear that the plasma density is homogeneous over a large width of more than 40 cm. The plasma density, near the substrate, has increased drastically at a pressure of 0.2 mbar, thereby enhancing the deposition rate of microcrystalline silicon. This increase in plasma density and deposition rate can be attributed to fact that the plasma has extended towards the substrate. The electrons have a larger mean free path and confinement of the electrons becomes better at low pressures. This homogeneity of the plasma density is an indirect indication for homogeneous deposition. We also measured the thickness of the samples by a step profiler.

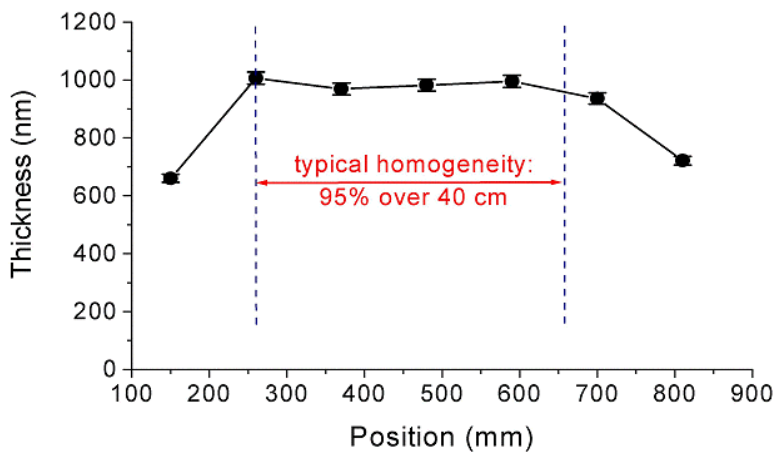


Figure 2-11: Thickness homogeneity in the batch PECVD reactor.

The lab-scale reactor and the in-line system are comparable with respect to the geometry of the plasma source. *Figure 2-11* shows the typical variation of the thickness of a deposition in the lab-scale system. The thickness homogeneity is better than 95% over a deposition width of 40 cm.

#### 2.4 Solar cells

In cooperation with DIMES and Utrecht University we made complete solar cells. In all cases the absorbing i-layer was deposited by MW-PECVD.

For the cell of the Utrecht University the structure is depicted in *Figure 2-12*. The cell structure of the DIMES cells can be seen in *Figure 2-13*.

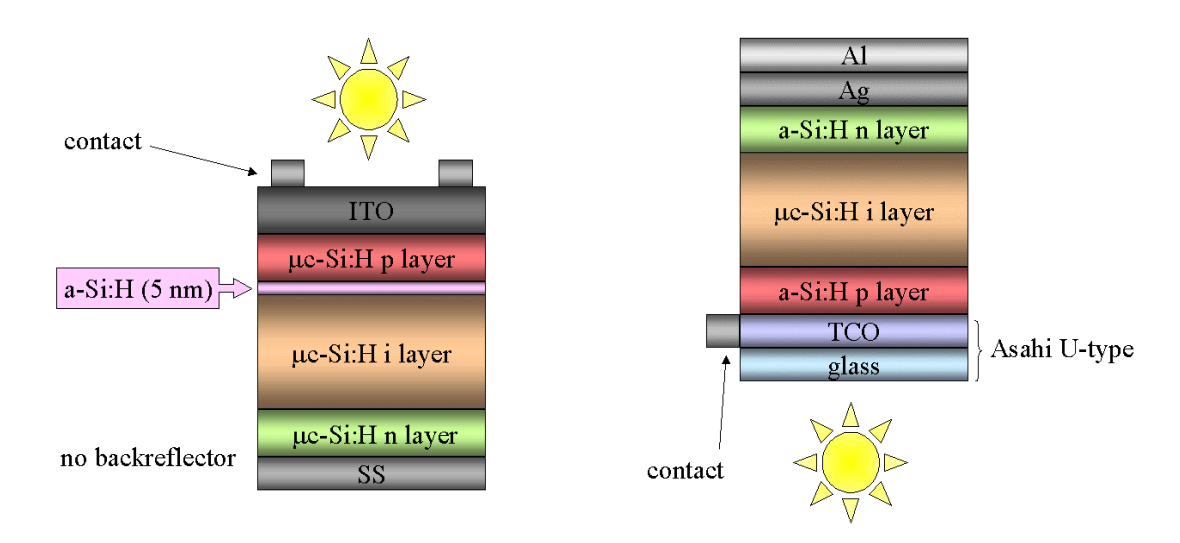


Figure 2-12: Cell structure of a Utrecht cell. Figure 2-13: Cell structure of a DIMES cell[6].

ECN-C--04-009

.

<sup>[6].</sup> In some cases DIMES used microcrystalline doped layers

DIMES or Utrecht University made the first doped layer of a device, subsequently the 'device' was sent to ECN, the intrinsic layer was deposited by MWPECVD and then the 'device' was sent back to DIMES or UU to complete it with the second doped layer and contacts.

Several parameters, like the argon flow, silane dilution and thickness of the intrinsic layers have been varied over a wide range (see  $Table\ 2-I$ ). It turned out that all the cells showed low efficiencies due to small  $J_{sc}$ .  $V_{oc}$ 's were rather good and fill factors were moderate ( $Table\ 2-2$ ). Main reason for the performances of the cells is probably the porosity of the intrinsic layers, in combination with the vacuum break, leading to a strong post-oxidation of the i-layers. Evidence for the high porosity is provided by dark conductivity, FTIR and SIMS measurements, which will be discussed in the next sections.

A high porosity of the layers not only results in a large concentration of oxygen due to post-oxidation, it also results in a higher defect density.

The level of the defect densities of the MW-grown layers (see table 2 and *Figure 2-14*) which is in the range of  $5\times10^{16}$  -  $2\times10^{17}$  cm<sup>-3</sup> is fairly good, though, and should allow for much higher cell efficiencies than obtained so far in the project [7].

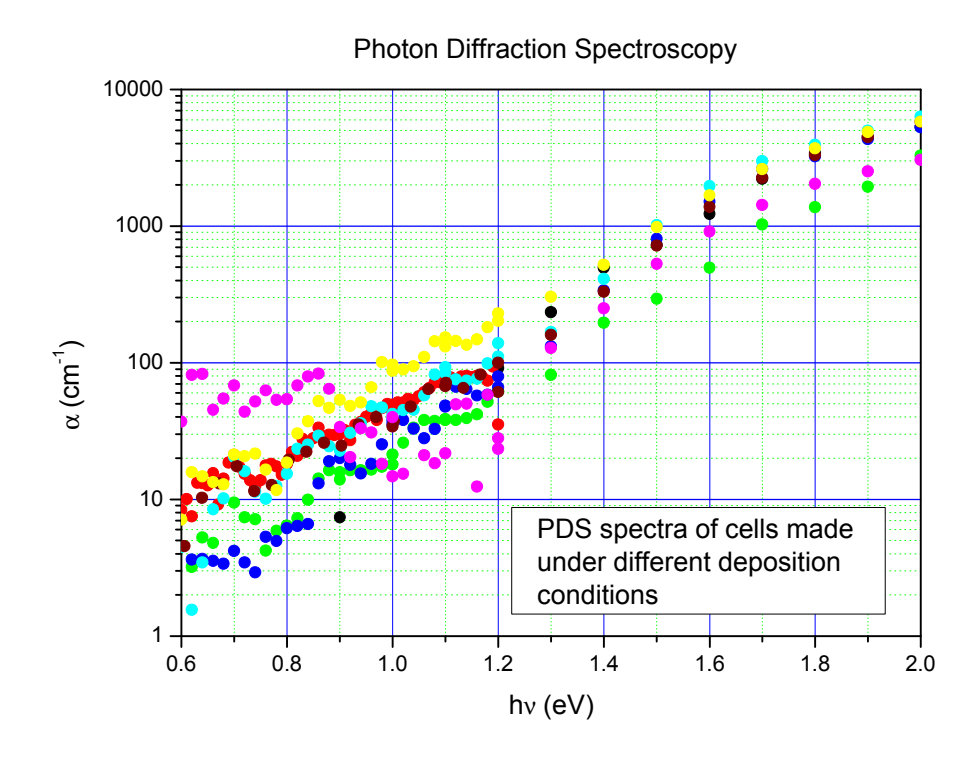


Figure 2-14: Optical absorption data of intrinsic Si layers grown by MWPECVD.

Other potential problems for the production of good devices are the quality of the seed layers and possible damaging of the SnO<sub>2</sub>:F layers by the MW plasma. We found that amorphous players give rise to a large amorphous incubation phase when growing a microcrystalline seed layer on top of them. This incubation phase probably provides a bandgap barrier (and thus a transport barrier) for the current between i- and p-layer.

Investigation of the effect of the plasma on SnO<sub>2</sub>:F layers showed that the layers were largely reduced to metallic Sn (and became opaque) when exposed to pure hydrogen, pure argon and combined hydrogen-argon plasmas for a typical deposition time of the seed layer (5-10 minutes). However, the transparency SnO<sub>2</sub>:F layers covered with a p-layer, showed to be

<sup>[7]</sup> M. Kondo, Solar Energy Mat. & Sol. Cells, 78 (2003) 543.

unaffected by MW plasmas. Apparently, the p layer can protect the SnO<sub>2</sub>F layers reasonable well, although an extra protecting ZnO layer covering the SnO<sub>2</sub>:F layer would be preferable.

Table 2-1 Deposition conditions of i-layers made by MWPECVD of the produced cells.

Deposition	Cell	T (*C)	p (mbar)	H <sub>2</sub> (secm)	SiH <sub>4</sub> (sccm)	Ar (sccm)	d (nm)
20213	Utrecht1	250	0.1	200	18	50	1696
20236	A1583	175	0.1	200	15	50	1274
20237	B1583	175	0.1	200	5	50	1467
20238	C1583	175	0.1	200	5	5	666
20239	A1584	175	0.07	200	30	25	1810
20240	D1583	175	0.07	200	20	25	2594
20241	B1584	175	0.07	100	15	12	2115
20242	C1584	175	0.06	50	7	10	1758
20243	D1584	175	0.22	50	4	10	1444
20247		275	0.1	200	10	0	1805
20248	C706-I	230	0.13	200	10	0	966
20249	C706-II	230	0.13	200	10	0	624
20250	C707-I	230	0.13	200	10	0	453
20251	C707-II	230	0.1	30	3	0	1375
20252	C708-I	220	0.1	200	10	0	1379
20253	C708-II	220	0.1	30	3	0	
20255	A1596-III	150	0.1	20	2	0	
20256	A1569-II	115	0.11	50	5	0	
20278	A1706-II	175	0.07	100	13	12	936

Table 2-2 Structural and electrical properties of the produced cells. Defect density is obtained

from optical absorption measurements at the subbandgap energy level of 0.8 eV.

Deposition	cell structure	r <sub>d</sub> (nm/s)	X <sub>c, top</sub> (%)	X <sub>c, bottom</sub> (%)	$V_{oc}(mV)$	J <sub>sc</sub> (mA/cm²)	FF	eff. (%)	N <sub>d</sub> (cm <sup>-3</sup> )
20213	ss/mc-n/i/mc-i/mc-n/TCO	1.18			212	3	28	0.17	1.80E+17
20236	glas/SnO/a-Si p, i, a-Si-n/Ag	0.78	0.56	0	524	0.9	38	0.19	6.50E+16
20237	glas/SnO/a-Si p, i, a-Si-n/Ag	0.44	0.72	0.61	493	0.6	37	0.11	
20238	glas/SnO/a-Si p, i, a-Si-n/Ag	0.25	0.63	0	519	1.8	31	0.28	
20239	glas/SnO/a-Si p, i, a-Si-n/Ag	1.01	0.71	0.58	535	1.4	36	0.27	
20240	glas/SnO/a-Si p, i, a-Si-n/Ag	1.73	0.7	0.56	617	1	29	0.18	
20241	glas/SnO/a-Si p, i, a-Si-n/Ag	0.86	0.74	0.6	617	2.1	40	0.51	6.10E+16
20242	glas/SnO/a-Si p, i, a-Si-n/Ag	0.49	0.74	0.52	514	1.5	43	0.33	1.53E+17
20243	glas/SnO/a-Si p, i, a-Si-n/Ag	0.44	0.75	0.52	490	1.2	39	0.21	1.94E+17
20247		0.60							1.85E+17
20248	glas/SnO/c-Si p, i, c-Si-n/Ag	0.57	0.75	0.61					
20249	glas/SnO/c-Si p, i, c-Si-n/Ag	0.52	0.73	0.61					
20250	glas/SnO/c-Si p, i, c-Si-n/Ag	0.76	0.68	0.67	95	1.1	29	0.03	
20251	glas/SnO/c-Si p, i, c-Si-n/Ag	0.35	0.76	0.75	149	1.2	36	0.07	
20252	glas/SnO/ZnO/c-Si p, i, c-Si-n/Ag	0.66			147	1.1	29	0.05	
20253	glas/SnO/ZnO/c-Si p, i, c-Si-n/Ag				185	2.3	43	0.18	
20255	glas/SnO/a-Si p, i, a-Si-n/Ag				356	0.2	40	0.02	
20256	glas/SnO/a-Si p, i, a-Si-n/Ag				337	0.2	38	0.03	
20278	glas/SnO/a-Si p, i, a-Si-n/Ag	0.52			671	1.62	47.8	0.52	

ECN-C--04-009 21

### 2.5 Vacuum-break experiment

In order to determine the effect of vacuum breaks on the electric performance of the solar cells, a dedicated experiment has been performed in cooperation with DIMES. A scheme of this experiment is shown in the following figure. Three devices are involved; one with a microcrystalline i-layer deposited at ECN and two entirely amorphous Si devices which were completely produced by DIMES.

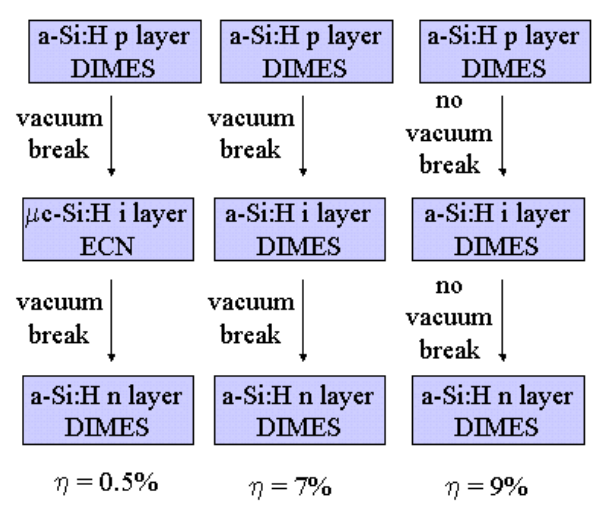


Figure 2-15: Scheme of vacuum-break experiment.

It appeared that the vacuum break does have negative effects on the cell performances. This becomes clear from the graph below.

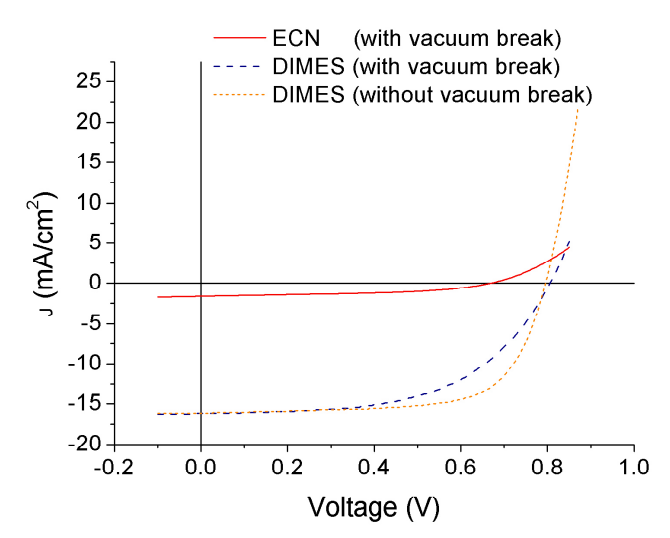


Figure 2-16: IV curves of the three devices of the vacuum-break experiment.

The DIMES device with vacuum break shows a reduction in the efficiency, mainly caused by a doubling of the series resistance and a consequent reduction of the fill factor ( $\sim 0.57$  instead of  $\sim 0.7$ ) with respect to the cell made without vacuum break. The current has decreased only a little. The initial efficiency of the amorphous silicon cell manufactured with vacuum break was

7% as compared to 9% for the cell without vacuum break. It can be concluded that vacuum breaks do have a negative effect on a-Si cells.

The experiment unfortunately does not inform us on the effect of a vacuum break in the manufacturing of  $\mu$ c-Si cells, with non-porous  $\mu$ c-Si layers, and it can also not predict what cell efficiencies could be obtained using the present MW-grown i-layers in a cell manufacturing process without vacuum break. The amorphous i-layers in the DIMES cells are of good quality: they are compact and little vulnerable to post-oxidation. The cells with the MWPECVD grown i-layers will be much more vulnerable for post-oxidation.

## 2.6 Dark conductivity

A setup for dark conductivity has been build as a new characterization technique for electrical characterization of the Si films. Validation of the setup was performed by a measurement on an amorphous-silicon reference sample from Utrecht University. The results matched the expected values (i.e.  $E_a \approx 0.91$  eV and  $\sigma_d \approx 1 \times 10^{-10}$  S/cm). The activation energy is a measure for the position of the Fermi level in the band gap. In case of intrinsic microcrystalline silicon the activation energy should be 0.55 eV. Lower values point to the presence of oxygen in the layers.

#### Reproducibility

In the course of the second year of the project it was found that dark conductivity measurements of porous samples were difficult to reproduce. Therefore we have carried out experiments in order to investigate the origin of these reproducibility problems.

Four depositions have been performed under identical deposition conditions. From FTIR measurements it could be shown that the resulting  $\mu$ c-Si layers are highly porous. Next, the  $\mu$ c-Si samples have been measured three times each. *Figure 2-17* shows the result of one of the samples.

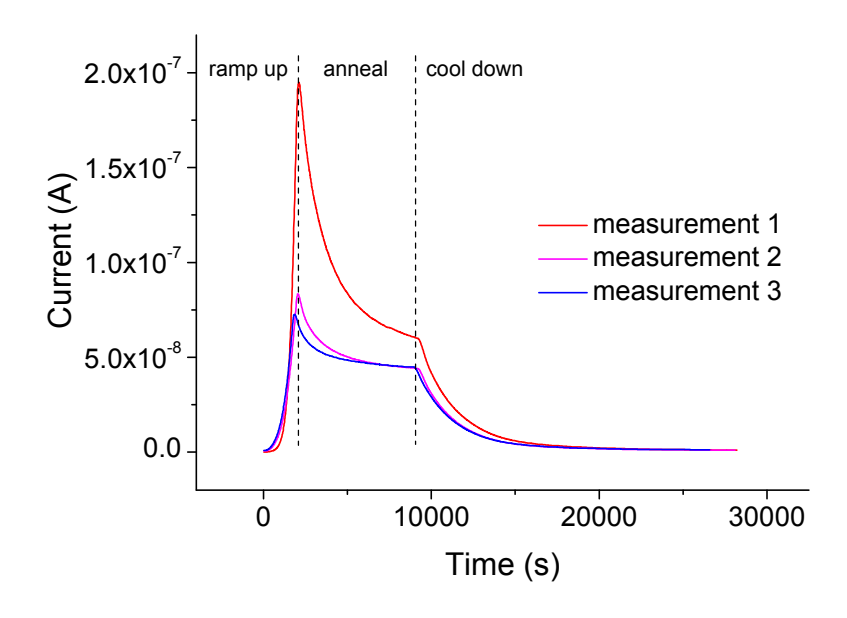


Figure 2-17: Current vs. time in the different phases of a dark conductivity measurement.

The sample has been annealed at 120°C for 2 hours, the ramp-up rate was 3°C/min. and the ramp-down rate 0.5°C/min.

measurement	$E_a(eV)$	$\sigma_{dark}$ (S/cm)
1	0.4173	$4.0\ 10^{-8}$
2	0.3101	$4.4  10^{-8}$
3	0.2828	5.1 10 <sup>-8</sup>

ECN-C--04-009 23

The current, and thus the conductivity decreases during annealing. The decrease of the current (increase of the sheet resistance) during the anneal stage is likely due to evaporation of moisture from the layers. The effect of increasing sheet resistance during anneal is smaller for secondand third measurements. These results illustrate the lack of reproducibility of dark conductivity measurements of such porous layers. In order to reduce the moistening effect, the vacuum conditions of the dark conductivity set-up should be further improved.

During the measurement phase (the cool down phase) the conductivity of porous layers shows a non-Ahrenius behaviour, probably due to a slight re-moisturing of the layers. For these cases the curve of log(s) versus I/T does not yield a straight slope and the activation energy  $E_a$  is smaller at lower temperatures. This is illustrated in the figure below.

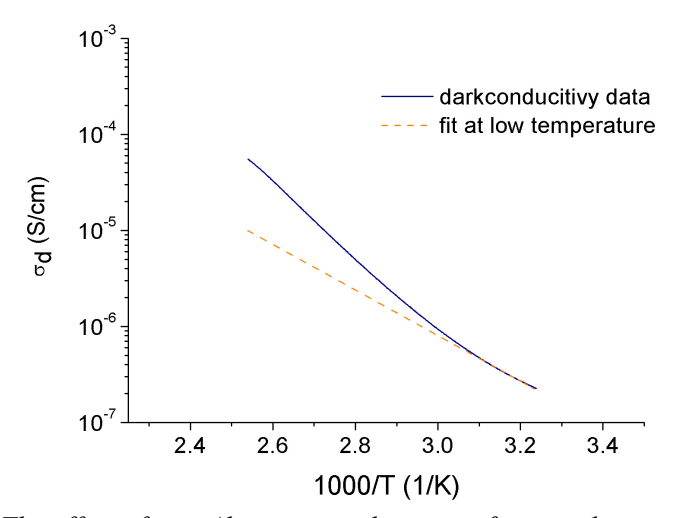


Figure 2-18: The effect of non-Ahrenius conductivity of porous layers: non-linear slope of log(s) versus 1/T.

Experimental results for layers grown at various deposition temperatures Figure 2-19 shows the activation energy of the dark conductivity obtained for a series of intrinsic  $\mu$ c-Si samples for which the deposition temperature was varied and other conditions were kept constant: SiH<sub>4</sub> flow was 18 sccm, H<sub>2</sub> flow was 200 sccm and Ar flow was 50 sccm. The power was adjusted at 1000 W and the pressure at 0.1 mbar. (Values for  $E_a$  as displayed are those of the first measurement)

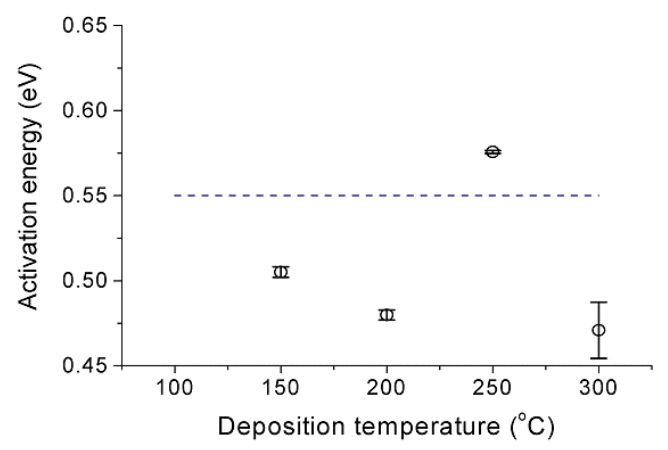


Figure 2-19: The activation energy for dark conductivity of intrinsic mc-Si grown at various deposition temperatures.

Figure 2-20 shows the conductivity results of this series. The photoconductivity, which is correlated to the defect density of the material, is not depending on the substrate temperature. The dark conductivity, in contrast, increases by two orders of magnitude. Consequently, the ratio of the photo- and dark conductivity decreases. For good electronic quality, the value of  $\sigma_{dark}$  should be below  $1\times10^{-8}$  S/cm and the ratio of  $\sigma_{photo}/\sigma_{dark}$  should be larger than 1000. The increase of the dark conductivity can possibly be attributed to, among others, the increased crystal fraction, 'better linked' crystal of the thermal activated doping of oxygen.

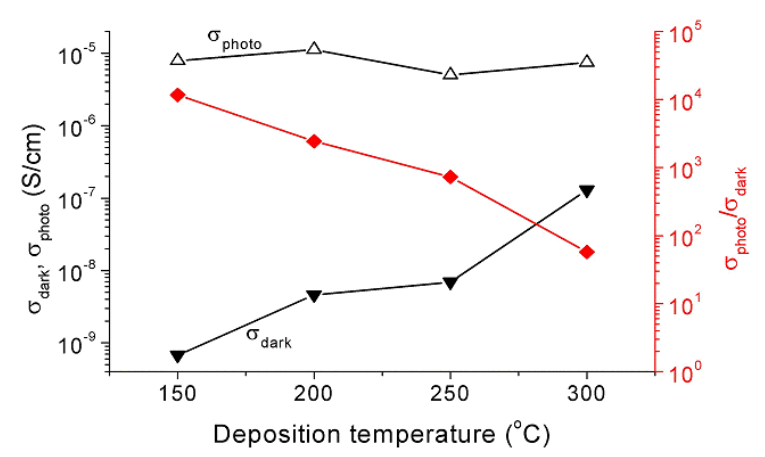


Figure 2-20: The photo- and dark conductivity of intrinsic mc-Si grown at various deposition temperatures.

#### 2.7 FTIR

As mentioned in the previous report [8], Fourier Transformed Infrared Spectroscopy (FTIR) shows that the layers deposited by MWPECVD contain a large amount of oxygen, which is either caused by post oxidation or is due to impurities originating from the deposition chamber and process gases.

Oxygen concentration, present inside the reactor chamber during depositions, was reduced in the second year of the project by improvement of the vacuum. This was done by enhancement of the encapsulation of the quartz tube and improvement of the sealing of the front and rear covers of the deposition system, and by the use of gas purifiers for all three used deposition gases.

Figure 2-21 shows that the 'as deposited' FTIR spectrum of a typical sample contains low concentrations of oxygen, which is reflected by the absence of the Si-O and Si-O<sub>2</sub> bands at 1070 cm<sup>-1</sup> and 1160 cm<sup>-1</sup>. Absence of visible absorption at these wavelengths indicates that the layers as deposited contain an oxygen concentration of less than 0.1 % (or  $< 5 \times 10^{19}$  cm<sup>-3</sup>). Device quality material should have oxygen concentrations below  $10^{19}$  cm<sup>-3</sup>. After deposition, the oxygen concentration increases with time, which is clearly illustrated by the spectrum collected after the sample has been exposed to air for 5 days. The absorption bands for this layer indicate an oxygen content of about 10 % (or  $5 \times 10^{21}$  cm<sup>-3</sup>). Therefore, it can be concluded that the deposited layers suffer from post oxidation, caused by porosity. Enhanced post-oxidation, due to porosity is a common effect for  $\mu$ c-Si layers. For layers grown with RF-PECVD, layers with higher porosity typically result from depositions with high plasma power and strong hydrogen dilution. In principle post-oxidation of intrinsic  $\mu$ c-Si layers can be avoided by 'sealing' through p- and n-layers, such that the entire solar cell is unaffected by this problem [9]. To achieve this, the deposition of all p, i, and n-layers should be performed without vacuum interruptions.

ECN-C--04-009 25

<sup>[8].</sup> W.J. Soppe et al, Progress Report MissionN & Miracle, Period 1 July 2001 to 30 June 2002.

<sup>[9].</sup> A.V. Shah, et al, Solar Energy Mat. Sol. Cells 78 (2003) 469-491.

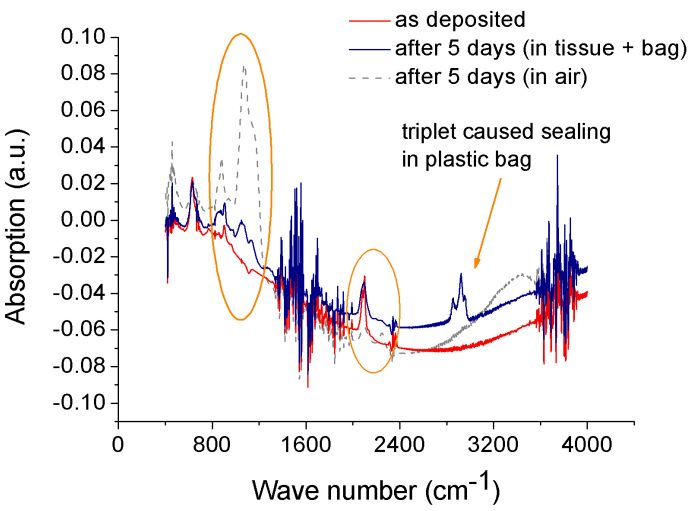


Figure 2-21: FTIR spectra of two pieces of one sample to show the effect of exposure to air and sealing on post-oxidation.

For the solar cells that have been produced in corporation with DIMES and Utrecht University, however, vacuum interruptions were inevitable. Therefore, it was necessary to find ways to prevent or at least reduce the post-oxidation of the intrinsic layers grown by MWPECVD. One way is depositing more dense layers. Another way is sealing of the samples after deposition. It appeared that wrapping the sample in a tissue (in a plastic bag, filled with nitrogen) could reduce the post-oxidation of the sample over a period of a few days (see *Figure 2-21*). In this case one observes an oxygen concentration in the range of 1 % (i.e. about 5×10<sup>21</sup> cm<sup>-3</sup>) after storage of 5 days. This value, though, is clearly beyond the criterion for device quality silicon. The sealing also gives rise to some extra absorption peaks in the IR spectrum of the samples. The triplet at ~2900 cm<sup>-1</sup> indicates the presence of carbon-hydrogen bonds. They originate from degassing of the plastic bag. They are only weakly bonded, as the peaks shrink after annealing (1 hour @ 250°C).

The density of a sample is reflected by the refractive index of the material. Interference fringes in the FTIR spectra provide a value for the refractive index provided that the thickness of the layer is well known. In the following figure, the refractive index is plotted vs. the residence time of the species in the reactor, i.e. pressure/total flow.

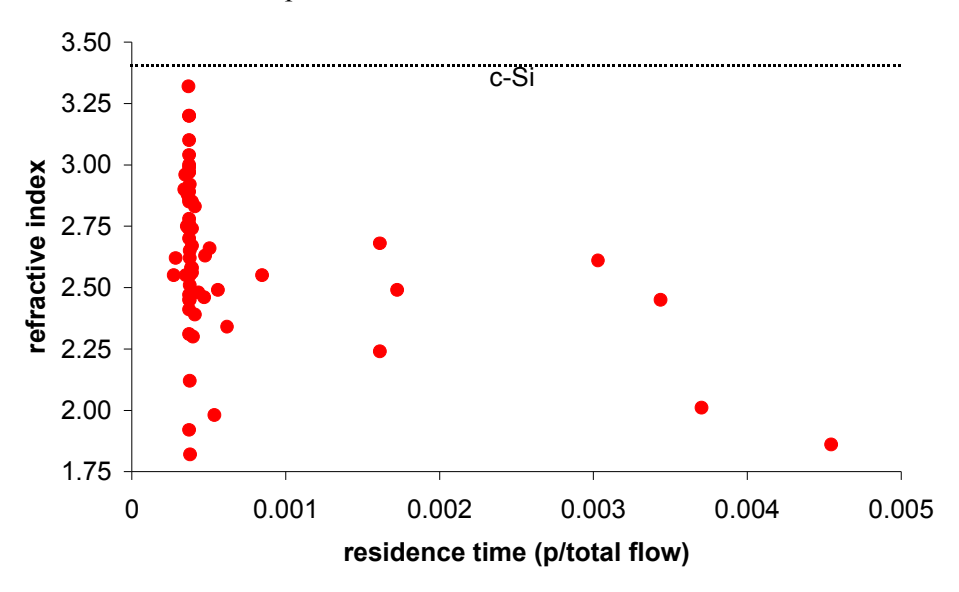


Figure 2-22: The refractive index, obtained by FTIR, as a function of the residence time.

It is clear that higher refractive indices, and therefore higher densities can be obtained for smaller residence times. The refractive index has also been obtained by reflection measurements in the visible wavelength regime and the results are in agreement with the results shown above. The refractive indices of the layers shown in

Figure 2-22 are smaller than for crystalline silicon wafers. This can be attributed to porosity of the layers. Dense  $\mu$ c-Si layers should have a refractive index of around 3.4 in the IR regime. Note that the refractive index is dependent of the wavelength. In the FTIR regime ( $\lambda \approx 10 \mu m$ ), n is typically 3.4 for silicon, whereas n is 3.9 at 630 nm (standard wavelength for optical properties in the visible wavelength regime).

A possible explanation for the behavior of the refractive index in

Figure 2-22 is the following. When the residence time becomes shorter, the balance of the dissociation chain:  $SiH_4 \rightarrow SiH_3 \rightarrow SiH_2 \rightarrow SiH \rightarrow Si$  will shift to the left. As a result, the amount of the very sticky SiH and Si species in the plasma will reduce. Arrival of sticky species at a substrate leads to dendritric growth with a large void fraction, as shown in the picture below. This open structure shown in this figure is the result of an extreme growth condition in which all species immediately stick to the surface upon arrival, and no diffusion on the surface takes place.

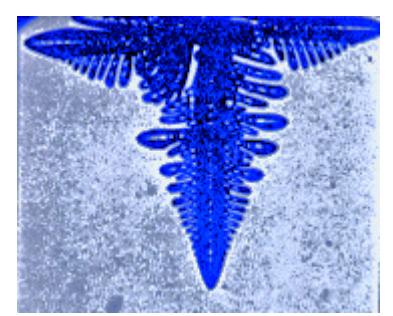


Figure 2-23: Dendritic growth as a result of 2-dimensional solidification of a metal. The finger-like shape of the solid results from instantaneous freezing of metal atoms at the growth surface, upon arriving from the melt.

The case of silicon growth from SiHx species is somewhat different because the sticking probability for all species is less than 1.0 and because of the presence of etching H atoms. But the trend will be similar: if the SiHx species arriving at the surface are stickier, the resulting layer will become more open.

#### 2.8 SIMS measurements

A few samples of  $\mu$ c-Si, deposited by MWPECVD have been analysed at the Philips Centre for Industrial Technology, in order to obtain quantitative data on oxygen and carbon contents of the layers. The SIMS measurements took place a few weeks after deposition. Deposition characteristics of these layers and average oxygen and carbon contents in the layers are presented in the table below.

Table 2	-3 Results o	f SIMS	measurements	for a numb	er o	f mc-Si laye	ers.
---------	--------------	--------	--------------	------------	------	--------------	------

Sample	SiH <sub>4</sub> (sccm)	H <sub>2</sub> (sccm)	Ar (sccm)	p (mbar)	T <sub>depo</sub> (C)	[O] (cm <sup>-3</sup> )	[C] (cm <sup>-3</sup> )
20253-4	3	30	0	0.1	220	5.1E21	
20254-4	5	50	0	0.1	220	4.3E21	
20255-4	2	20	0	0.1	150	4.8E21	1.0E21
20275-4	15	100	12	0.07	175	4.2E21	1.1E21

A visual presentation of the measurements is shown in *Figure 2-24*.

ECN-C--04-009 27

The O and C concentrations are high and do not show a depth gradient. We determined the refractive indices by means of reflection measurements and found for all layers values below 3.2 at 630 nm, which implies that the density of the layers is low. Assuming that the major part of the oxygen and carbon atoms has entered the layer after deposition, these measurements imply that the layers contain very effective diffusion paths through the whole layers. The relatively high carbon content in the layers may be due to post-carbonation resulting from the sealing bags, as mentioned in the previous section.

The SIMS data underline previous conclusions that - for porous layers as grown by MWPECVD so far - vacuum breaks during the processing are disastrous for the quality of the solar cells.

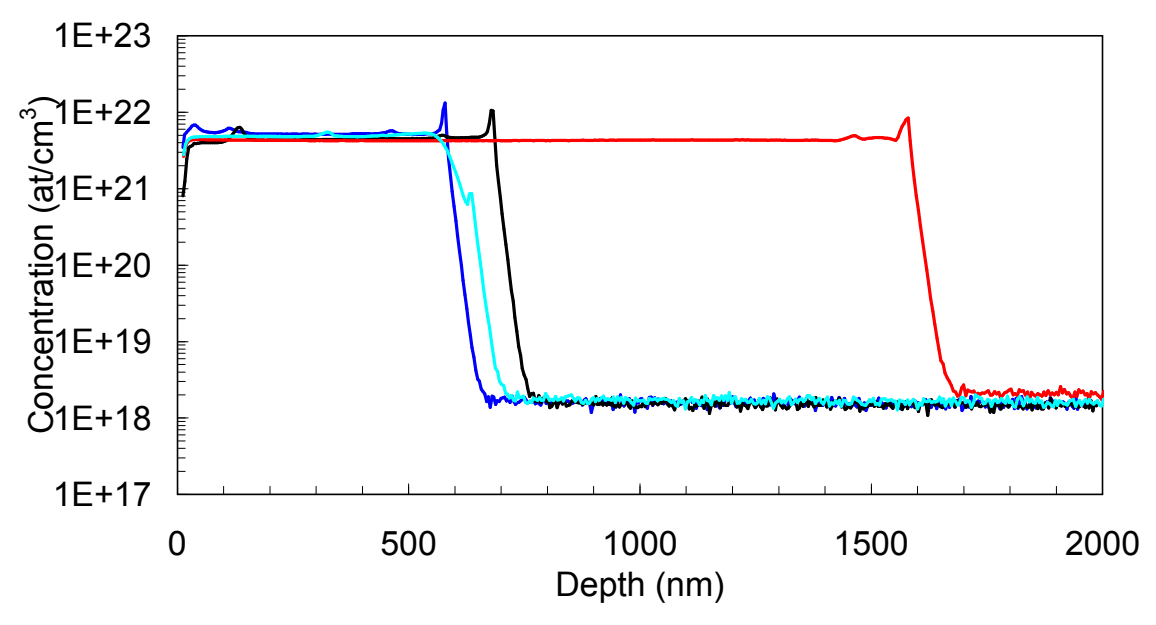


Figure 2-24: Oxygen profiles for mc-Si layers deposited by MWPECVD.

#### 2.9 Conclusions

The linear microwave source is a suitable plasma tool for growth of  $\mu c$ -Si, with large deposition rates and on large areas, using SiH<sub>4</sub> and H<sub>2</sub> as precursor gases. Deposition temperatures as low as 100 °C can be applied, which allows for polymer webs to be used as substrates. Addition of Ar to the plasma helps to obtain more stable plasma at low pressures but does not increase the crystallinity of the layers. Dark conductivity, FTIR and SIMS measurements show that most of the layers grown so far have rather high porosity, leading to fast post-oxidation when samples are stored in air. Even for samples sealed in bags filled with nitrogen, the oxygen content after 5 days of storage was well above the limit for device quality material. The post-oxidation, which was inevitable in this project since doped and intrinsic layers are deposited in different systems (leading to vacuum interruptions of several days), presumably is the main reason for the rather poor performances of the cells that have been manufactured so far. The defect density and the initial values of  $\sigma_{dark}$  and  $\sigma_{photo}$ , found for a series of layers indicate that - if the fabrication of cells could be performed without vacuum break - the present  $\mu c$ -Si material would provide cells with appreciably higher efficiencies. This conclusion urges for the construction of a 3-chamber MWPECVD system in which all active layers can be deposited without vacuum break.

Future work with the present one-chamber MWPECVD reactor will concentrate on growth of denser layers, in order to improve the electronic quality of the  $\mu$ c-Si layers. Further decrease of residence times seems to be a clue to obtain more compact layers, which will be less vulnerable to post-oxidation.

#### 2.10 Publications and Presentations

- 1. W.J. Soppe, A.C.W. Biebericher, C. Deviliee, H. Donker, H. Schlemm, *High rate growth of micro-crystalline silicon by microwave PECVD*, Presented at the WCPEC-3, May 11-18, 2003, Osaka, Japan,
- 2. A.C.W. Biebericher, C. Devilee, W.J.Soppe, *Low temperature deposition of microcrystalline silicon by microwave-PECVD*, 2nd aSiNet Workshop on Thin Silicon, February 19-21, 2003, Lisbon, Portugal.
- 3. Wim Soppe, Zonnecellen van microkristallijn silicium, ECN colloquium, 17-mrt-03
- 4. Wim Soppe, Camile Devilee, Arja Biebericher, Sacha Schiermeier, Harry Donker, J.K. Rath, *MICROWAVE PECVD OF MICRO-CRYSTALLINE SILICON*, Proceedings of the 29th IEEE PVSC, New Orleans, 2002, p 1174,
- 5. W.J. Soppe, C. Devilee, S.E.A. Schiermeier, H. Donker, J.K. Rath, *Microwave PECVD of micro-crystalline silicon*, Mat. Res. Soc. Symp. Proc. 715 (2002) A19.8.1.

ECN-C--04-009 29

### 3. CHARACTERISATION OF SI LAYERS DEPOSITED BY ETP

I.J. Houston, W.M.M. Kessels and M.C.M. v.d. Sanden, Eindhoven University of Technology

#### 3.1 Introduction

This report describes work carried out through the MissionN project at the Eindhoven University of Technology. Over the last two years this work has looked at many aspects of the deposition of microcrystalline silicon and can be divided into four main stages. Firstly, it was necessary to identify appropriate conditions for the deposition of microcrystalline silicon and extensive material characterisation was carried out which culminated in a paper currently submitted for publication to Thin Solid Films. The second and third phases of the research involved extensive investigations into the growth of the material. These investigations were made possible through the purchase of a spectroscopic ellipsometer (SE) and an atomic force microscope (AFM) by the Equilibrium and Transport in Plasmas group at the TU/e. The results from these techniques were combined with those obtained using an attenuated total reflection Fourier transform infrared (ATR-FTIR) setup, the application of which was explored by an MSc student. Finally a new deposition setup with greatly increased diagnostic capability was designed and constructed to allow these techniques to be combined in future measurements. A brief overview of each of these stages is included below. Additional material is included in the form of appendices. A list of publications and presentations is also given.

#### 3.2 Initial characterisation of material

The silicon layers deposited using the expanding thermal plasma (ETP) technique were extensively investigated and characterised using a broad range of techniques. The results are fully described in (Houston *et al.*) which is presented in Appendix A but a brief summary is included here for the sake of clarity and completeness.

It was shown that it is possible to use very high growth rates to deposit  $\mu$ c-Si:H films using the ETP technique by using dilution ratios  $R \ge 60$ . It is clear that the ETP technique is capable of depositing silicon thin films with a wide range of crystalline contents and material properties.

Raman spectroscopy revealed that crystalline fractions greater than 60 % are obtained at growth rates higher than 2 nm/s and XRD shows that the resultant  $\mu$ c-Si:H material exhibits a preferential crystalline orientation in the (220) direction although the material becomes randomly orientated at high crystalline contents. The results from TEM show the characteristic columnar structure typical of microcrystalline growth and confirm results from Raman which show that material grown at 250 °C with a dilution ratio R = 200 is almost polycrystalline. It was found that the substrate temperature had almost no effect on the crystalline content of the  $\mu$ c-Si:H although the crystallites within the  $\mu$ c-Si:H material became more randomly orientated at high substrate temperatures.

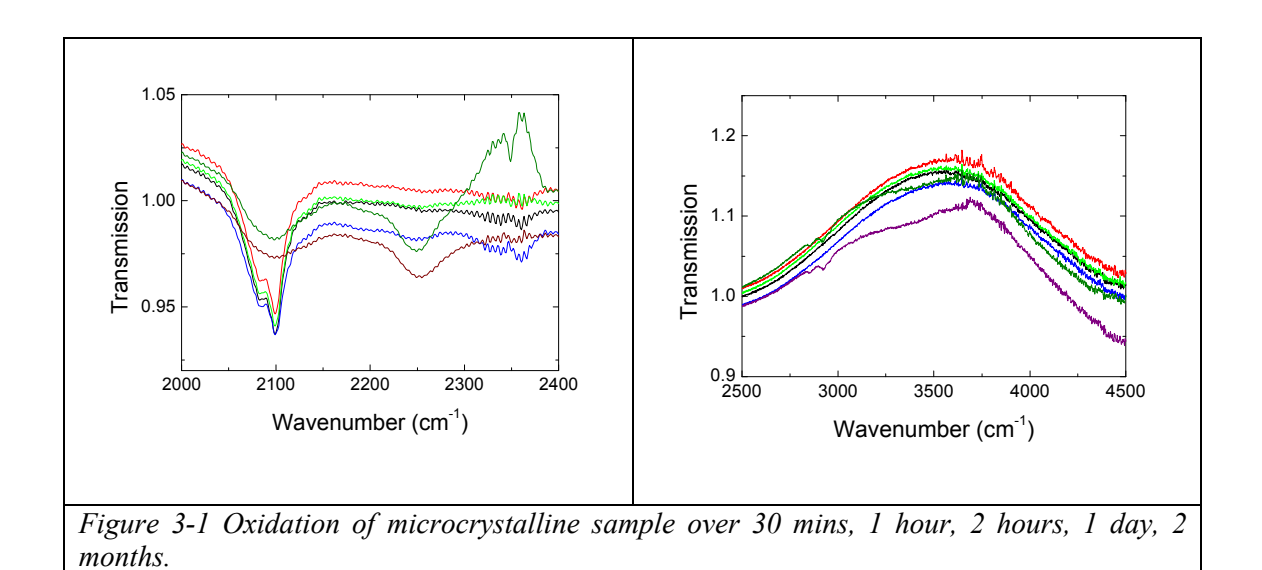
The atomic composition of the films was investigated by FTIR and ERD/RBS and it has been demonstrated that high *R*-values result in a decrease in silicon density and hydrogen concentration. A significant amount of molecular hydrogen was found to be present in the films. It has been shown that the atomic composition is affected by the substrate temperature and the results from FTIR and ERD/RBS suggest that the use of a substrate temperature of 300 °C could slightly increase the silicon density and significantly reduce the hydrogen content.

It was concluded that the results obtained from these investigations showed the potential of the ETP technique for the very high rate deposition of µc-Si:H films and provide a strong

foundation for further investigation to elucidate the optoelectronic material properties and the performance of the material in solar cells.

In addition to the above results, which have been submitted for publication, work was also carried out to investigate the oxidation of the films. The occurrence of oxidation has profound implications for the use of  $\mu c$ -Si:H in solar cells. A high degree of oxidation may be indicative of porous low quality material and results in material that is unsuitable for use in solar cells. Any method of mitigating or eliminating this effect would be of great interest. For this reason the extent to which ETP  $\mu c$ -Si:H oxidises and the underlying mechanism behind this process has been investigated. The timescale of oxidation as well as the influence of temperature is investigated and an attempt is made to limit the process.

The time dependence of oxidation is of critical importance. For several techniques such as ERD, FTIR and spectroscopic ellipsometry the occurrence of oxidation may have a significant effect on the results. It is vital to obtain knowledge regarding the timescale of oxidation in order to determine how quickly measurements should be carried out. FTIR was used to measure a  $\mu$ c-Si:H film deposited at R = 200 at various times after deposition (*Figure 3-1*).



In the two regions that are examined two effects are apparent. Firstly, the double peak structure at approximately 2100 cm<sup>-1</sup> (which is a characteristic of microcrystalline silicon) is seen to collapse after approximately one day of exposure to air. A peak then emerges at 2254 cm<sup>-1</sup>, which is known to correspond to a hydrogen atom bonded to a silicon atom that is bonded to three oxygen atoms. Hence it is clear that oxidation is not only a surface effect, but also involves the insertion of oxygen between silicon atoms in the bulk. This conclusion is supported by the emergence of peaks at 1060/1075 cm<sup>-1</sup> corresponding to Si-O-Si bonds and the size of these peaks shows that surface oxidation alone cannot account for all the oxygen within the material. In addition to these effects the appearance of the Si-O-H stretch at 3500 cm<sup>-1</sup> shows oxygen is also inserting between silicon and hydrogen.

From this we can conclude that as long as FTIR or SE are carried out within a day of deposition there is little need to consider the effects of oxygen incorporation. However, great care should be taken with ERD regarding the timescale of the measurements and the conclusions drawn from oxygen content results due to time dependency.

It is possible that the oxidation of  $\mu$ c-Si:H is thermally activated and this has been investigated by taking two samples after deposition and conducting FTIR measurements over time. One sample was removed from vacuum at 250 °C while the other was cooled to below 100 °C prior

to prior to removal. Oxidation was monitored by observing the Si-O-Si bonding peaks at 1060/1075 cm<sup>-1</sup>. It was found that oxidation is delayed by cooling prior to removal from vacuum but the level of oxidation over the long term is unaffected.

## 3.3 Spectroscopic Ellipsometry

Due to the paucity of information regarding the growth of  $\mu$ c-Si:H at very high growth rates the use of spectroscopic ellipsometry (SE) to elucidate the exact form of the layer evolution is of great interest. This technique has already been successfully employed in the analysis of  $\mu$ c-Si:H deposited at low growth rates<sup>1</sup> and now, with the advent of both spectroscopic ellipsometers capable of data collection over very small timescales and a technique which provides high growth rates for  $\mu$ c-Si:H, it should be possible to conduct similar investigations for high rate  $\mu$ c-Si:H.

The type of information that can be extracted from SE is heavily dependent upon the fitting method that is employed. In the ETP group at the TUE we have used a Lorentz oscillator model to fit our data and this is described below. This type of model provides the optical constants of the deposited material and also gives information on thickness and surface roughness. By observing these quantities with time we can draw conclusions regarding the growth of a particular layer.

In general the data is fitted using a multi layer model that is constructed to represent the structure of the material as accurately as possible. Typically a model is used which incorporates four layers (*Figure 3-2*). The bare substrate can be modelled using a layer of silicon and a layer of silicon oxide. The deposited material is modelled using a bulk layer and a surface roughness layer. The surface roughness layer is a 50/50 mix of voids and bulk material that is constructed using the Bruggeman effective medium approximation (BEMA). The bulk layer is constructed using Tauc-Lorentz oscillators to simulate the a-Si:H or μc-Si:H material. Amorphous silicon is simulated using only one oscillator whereas microcrystalline typically requires two.

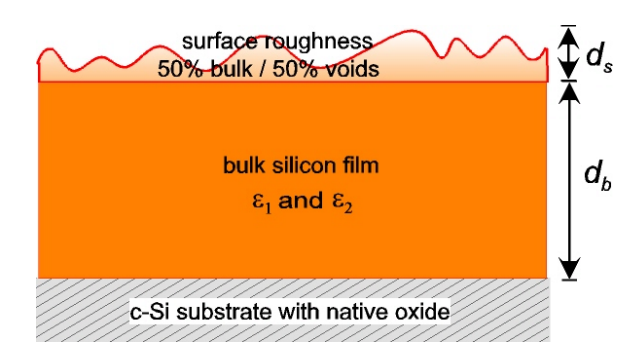


Figure 3-2: Multi-layer model used to model mc- and amorphous silicon.

The Tauc-Lorentz oscillator model simulates the response of a layer to light by using a four-parameter oscillator. The four parameters can be interpreted as the amplitude of the oscillator, its resonant position, its width and the energy gap of the material. The fitting of amorphous silicon can be achieved relatively easily using the Tauc-Lorentz oscillator model. The parameters that describe the oscillator do not vary during the course of the deposition and so fitting does not present a significant challenge. However, the growth of microcrystalline silicon is not homogeneous and so the modelling is more difficult. This requires two Tauc-Lorentz oscillators with parameters that vary with time. The initial phase of the growth is modelled

ECN-C--04-009

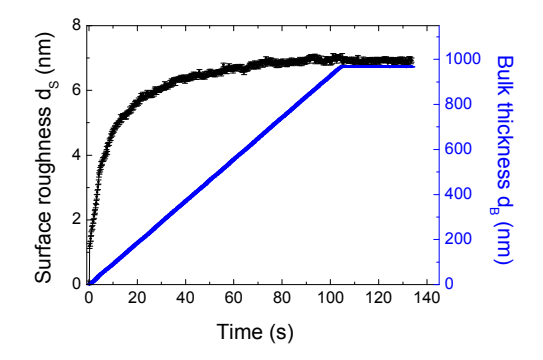
-

<sup>[1]</sup> R. W. Collins, A. S. Ferlauto, G. M. Ferreira, Chi Chen, Joohyun Koh, R. J. Koval, Yeeheng Lee, J. M. Pearce and C. R. Wronski, Solar Energy Materials and Solar Cells. 78, (2003) 143

using only one oscillator and as the deposition progresses two oscillators become necessary. As well as providing the optical constants of the material under consideration this method of fitting also allows us to observe the evolution of the surface roughness and bulk thickness of the material over time. This is used to determine the quality of the deposited material as well as the points at which phase changes occur.

## 3.4 Amorphous silicon

Spectroscopic ellipsometry studies were first conducted on a-Si:H as the analysis is significantly simpler than that of  $\mu$ c-Si:H. The results showing both bulk thickness and surface roughness as well as the optical constants of the material are presented below (*Figure 3-3*).



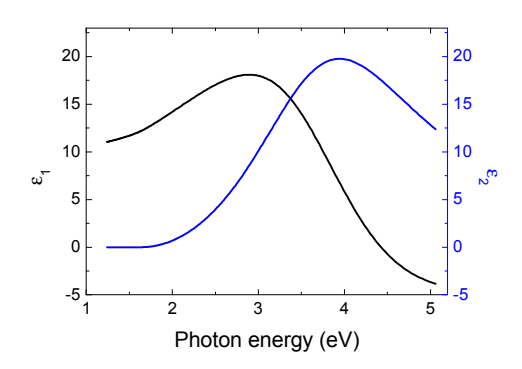


Figure 3-3-a: Results from amorphous silicon showing evolution of surface roughness and bulk thickness.

Figure 3-3-b: Optical constants of amorphous silicon as determined from SE.

The deposition rate of 10.3 nm/s found from SE agrees with the deposition rate of 10.1 nm/s obtained from FTIR measurements. In addition the optical constants found here for ETP a-Si:H are entirely consistent with those found in literature<sup>2</sup>. The results can also be compared to those from AFM (Figure 4). The surface roughnesses from the two techniques are compared and AFM produces significantly lower values. This is commonly observed and is likely due to the difference in the definition of surface roughness for the two techniques. Here AFM surface roughness is defined as the rms roughness and this may not correspond to the roughness calculated by SE. AFM may be insensitive to sub-surface effects that are detected by spectroscopic ellipsometry and interpreted as part of the surface layer.

34 ECN-C--04-009

\_

<sup>[2].</sup>A. S. Ferlauto, J. Koh, P.I. Rovira, C.R. Wronski, R.W. Collins, G. Ganguly, J. Non-Cryst. Sol. 266-269 (2000) 269

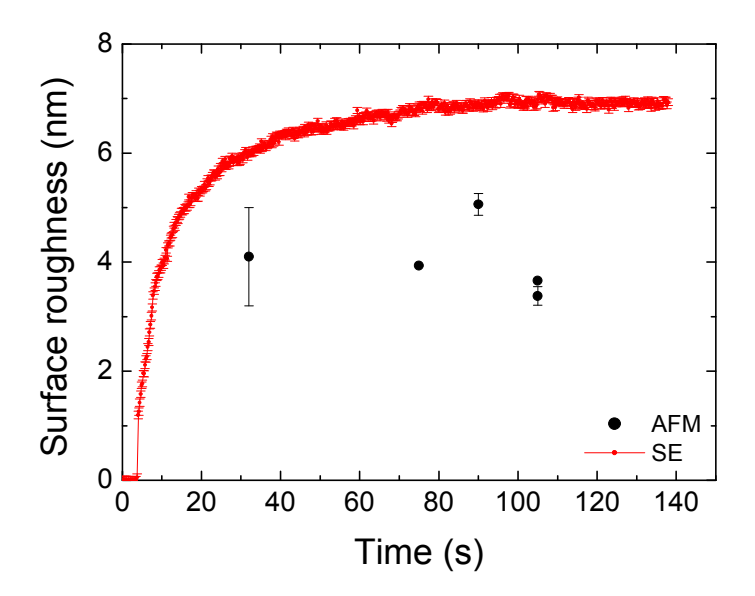


Figure 3-4: Comparison of surface roughness from SE and AFM for amorphous silicon.

It is notable that the results from SE contain no evidence of nucleation. In most results from low deposition rate material a small peak is seen in the surface roughness in the initial stages of deposition and this is generally ascribed to the initial nucleation of the material. It is likely that at these high growth rates (10 nm/s for this sample) the time resolution used here (0.6 s) is not sufficient to observe this effect.

The energy gap can also be calculated from these results<sup>3</sup>. This analysis provides a Tauc gap of 1.73 eV, which is perfectly consistent with amorphous material.

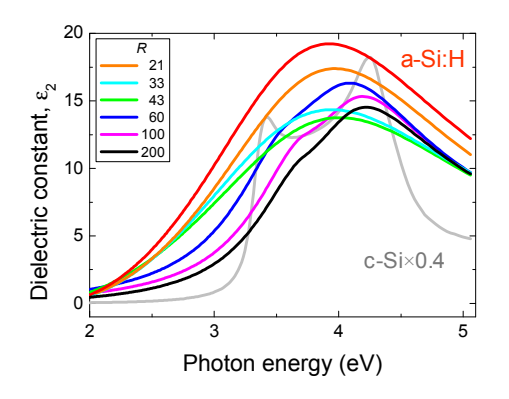
It is clear that spectroscopic ellipsometry is a powerful and reliable method for the analysis of amorphous silicon.

### 3.5 Microcrystalline silicon

The same conditions for the deposition of  $\mu$ c-Si:H which were considered previously (Houston *et al.*) were also investigated using SE in conjunction with other techniques in order to provide information on layer evolution.

SE is particularly sensitive to changes in material properties such as crystallinity and this is illustrated through comparison with results from Raman spectroscopy (*Figure 3-5*).

<sup>[3].</sup>J. Koh, Y. Lu, J. S. Burnham, C.R. Wronski, and R. W. Collins, Appl. Phys. Lett. 67 (1995) 2669.



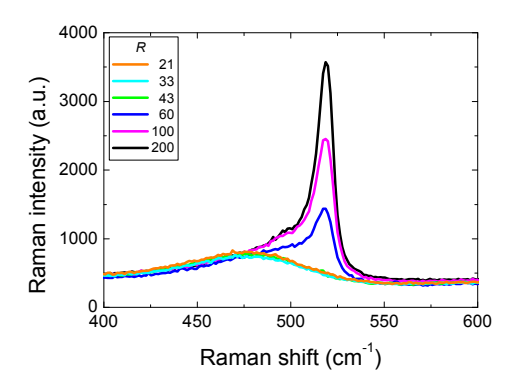
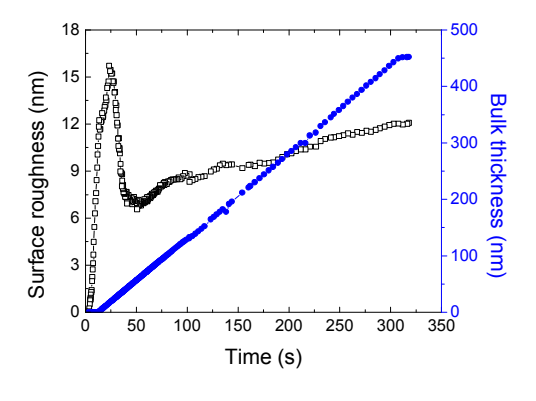


Figure 3-5-a: Optical constants as a function Figure 3-5-b: Results from Raman of R value determined by spectroscopic spectroscopy as a function of R value ellipsometry

From these results we see that both Raman spectroscopy and SE show the presence of crystallinity. In Raman spectroscopy this is evident from the emergence of the 520 cm<sup>-1</sup> peak and in SE this is shown by the emergence of a shoulder in the dielectric constant at low photon energy. In addition to this SE sees a change in the nature of the amorphous material with increasing R that is not immediately apparent from Raman spectroscopy.

In situ analysis of microcrystalline silicon shows the evolution of surface roughness with time (Figure 3-6-a). The characteristic shape of this plot is usually explained with reference to the model shown below (Figure 3-6-b). The material begins as an amorphous "incubation layer" (although in the some microcrystalline material such as that shown in Figure 3-6-a this is often absent) before microcrystalline material begins to nucleate and grow within an amorphous matrix. When these crystallites meet the surface roughness of the material is at its maximum value. The surface roughness then decreases dramatically ("coalescence"). A roughening transition occurs as this process reaches equilibrium and the surface roughness then steadily increases for the remainder of the deposition ("standard roughening behaviour").



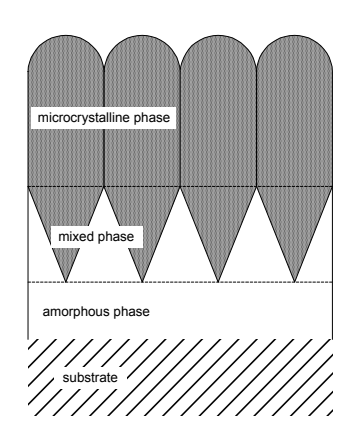
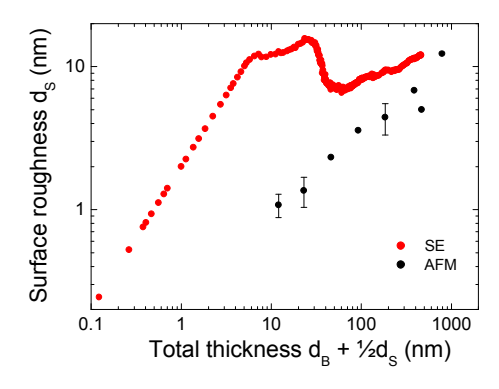


Figure 3-6-a: Fits from SE data obtained from mc-Si:H deposited at an R value of 200.

Figure 3-6-b: Multi-layer model used to model microcrystalline silicon showing phase changes during growth.

Comparison with AFM measurements (*Figure 3-7*) results in two interesting observations. Firstly, the AFM values for surface roughness are significantly lower than those from SE. This was also the case for amorphous silicon as mentioned previously and is of no great concern as long as the trend in the two sets of results is comparable. The second point of note is that the coalescence peak, which is so prominent in the SE results, is not present in the AFM results. This peak is sometimes observed from AFM measurements<sup>4</sup>. The absence of the peak in these results does require an explanation and there are several possibilities.



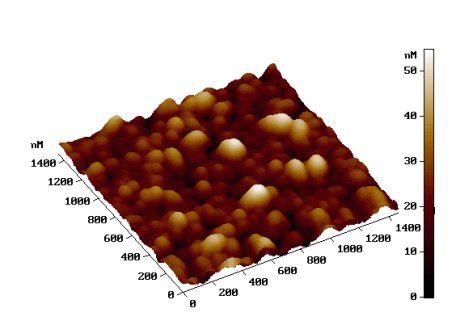


Figure 3-7-a Comparison of SE and AFM Figure 3-7-b AFM scan of 1 micron thick mcdata for mc-Si:H deposited at an R value of Si:H deposited at an R value of 200.

It is possible that the dimensions of the AFM tip (approximately 10 nm wide) mean that it is unable to resolve small enough features to accurately determine the surface roughness. It should also be borne in mind that the SE analysis is derived from the in-situ measurement of a single film whereas the AFM results are from the ex-situ analysis of a thickness series comprising several films. These two measurements may not be equivalent because of the effect of oxidation for example or due to some kind of relaxation effect as the deposition ends.

Another possibility is that the fit to the experimental data is incorrect and the peak is an artefact of this. Perhaps more accurate optical parameters could be obtained and the surface roughness peak removed. However, this would then produce a peak in the values for the optical constants when plotted against time, indicating that a significant change of some kind is taking place. In any case there is no evidence that such a set of optical constants exist. When addressing questions regarding the modelled results it may be of some value to consider the form of the model employed. The surface roughness is modelled by assuming a 50/50 ratio of voids to material in the surface layer. Although it may seem an unnecessary simplification to assume this as constant throughout the deposition there is little alternative as the void component is correlated to the thickness of the surface layer. In principle it is impossible to distinguish between a thin, dense layer and a thick, voidal layer<sup>5</sup>.

The most relevant question regards whether this peak represents a real event, which occurs during the growth that may either be an increase in surface roughness or a change in the void content of the surface layer. This has been addressed by invoking another in-situ technique, ATR-FTIR as shown in Section C.

ECN-C--04-009 37

\_

<sup>[4].</sup> H. Fujiwara, M. Kondo, A. Matsuda, Phys. Rev. B. 63 (2001) 115306.

<sup>[5].</sup> H. G. Tompkins, W. A. McGahan, Spectroscopic ellipsometry and reflectometry: a user's guide. (John Wiley and Sons, U.S.A., 1999) pp.91.

Spectroscopic ellipsometry has given us valuable information regarding the phase changes which occur during the growth of the  $\mu$ c-Si:H. As shown above, for our most crystalline material at R=200 we see that coalescence and roughening occur at 20 nm and 50 nm respectively. Although we have shown that the properties of ETP  $\mu$ c-Si:H are comparable to those of  $\mu$ c-Si:H deposited using other techniques (Houston *et al.*) there is one significant difference when we look at the positions of the phase changes in ETP material. In literature we find that the phase changes occur at a later stage in the deposition. Commonly coalescence and roughening in low rate  $\mu$ c-Si:H (deposited at 0.01-0.1 nm/s) occur at approximately 100 nm and 200 nm respectively<sup>4,6</sup>. This means that ETP  $\mu$ c-Si:H coalesces and roughens at a far earlier stage in the deposition than low deposition rate material and this may explain differences between high-rate  $\mu$ c-Si:H and low-rate  $\mu$ c-Si:H.

SE also confirms results from transmission electron microscopy (TEM). TEM suggests the absence of any incubation layer in the most crystalline material (Houston *et al.*). SE confirms this result as the surface roughness layer appears before any bulk layer is established – as evidenced by the straight line when surface roughness is plotted against bulk roughness in the early stages of deposition. This is an important result as the presence or form of any incubation layer during the initial stages of deposition may exert a great influence over the form of the final film. By analysing a series of depositions of varying R-value it should be possible to observe the emergence of an incubation layer as lower R-values are used. This analysis is shown below (*Figure 3-8*)

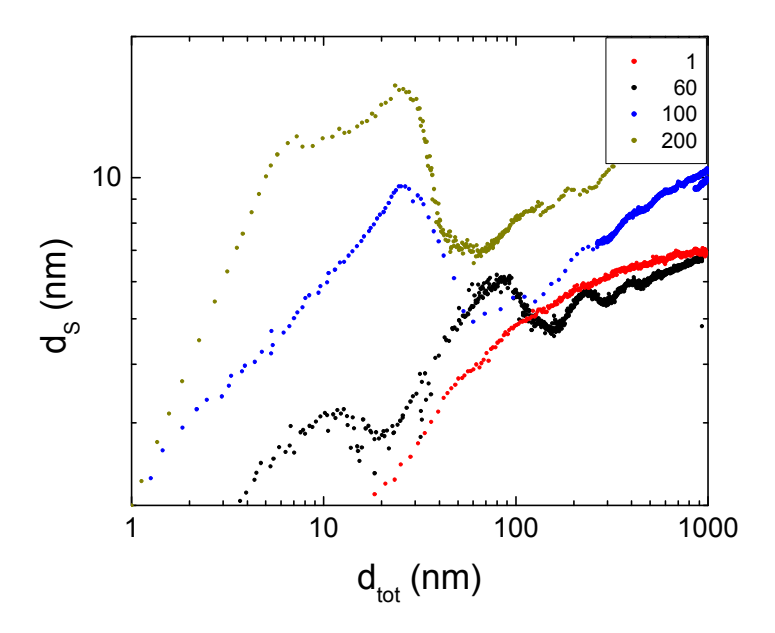


Figure 3-8: Results from spectroscopic ellipsometry showing surface roughness,  $d_s$ , plotted against total thickness,  $d_{tob}$  for several different values of R.

The incubation layer clearly emerges at R-values of approximately 100 and lower. Here we can also observe the transition from  $\mu$ c-Si:H to a-Si:H and we see that coalescence and roughening begin to occur at later stages in the deposition as lower R values are employed. Eventually coalescence and roughening do not occur and the material is entirely amorphous, only displaying standard roughening behaviour.

<sup>[6].</sup> A.S. Ferlauto, R.J. Koval, C.R. Wronski, and R.W. Collins, Appl. Phys. Lett. 80 (2002) 2666.

Previous results on a  $\mu$ c-Si:H have shown that substrate temperature does not have a significant influence on the crystalline content (Houston *et al.*) although it does influence the crystalline orientation and the short-range ordering of the amorphous fraction as well as the atomic composition. SE analysis on a  $\mu$ c-Si:H temperature series would elucidate the effect of temperature on the crystalline nature of the material and may indicate whether substrate temperature affects the presence of an incubation layer.

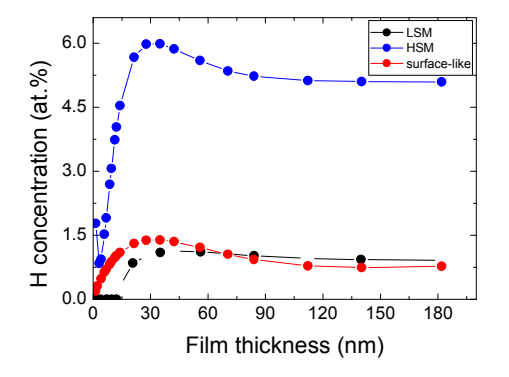
# 3.6 ATR-FTIR

Attenuated total reflection Fourier transform infrared (ATR-FTIR) involves reflecting an infrared beam through the substrate as a layer is deposited. The absorption with wavelength can then be viewed as a function of time during the deposition and a wealth of information can be obtained regarding the elements present within the layer as well as the manner in which they are bonded. When used in isolation this technique can provide unique information regarding the material properties and quality of the growing layer. When ATR-FTIR is combined with SE these two techniques together provide unparalleled insight into the nature and behaviour of the material under examination. Preliminary investigations have already been carried out on microcrystalline and amorphous material using ATR-FTIR (Appendix B) and a brief summary of this work is presented below.

ATR-FTIR was used for in situ measurements of surface and bulk hydrides in a-Si:H and  $\mu$ c-Si:H films. A model was developed to describe these measurements and this was used to establish a data analysis procedure, which has been verified by comparison of the results with results from ex situ transmission FTIR measurements. This model includes interference effects in the film on top of the internal reflection element (IRE) and differs according to the two-polarization state of the incident light. Hence measurements with polarized light are essential to obtain the hydrogen content from the ATR-FTIR measurements.

The procedures developed were used to investigate both the surface composition, in combination with ion-induced desorption, as well as the hydrogen bonding configurations as a function of the film thickness for various deposition conditions. The transition from a-Si:H to  $\mu$ c-Si:H that occurs for increasing flow ratios of hydrogen over silane was investigated. From SE studies it is known that under some conditions  $\mu$ c-Si:H film growth may begin with a thin (approx 6 nm thick) incubation layer, that may contain small crystallites. After the incubation layer the size of the crystallites grows until they make contact at approximately 25 nm. During this stage the amount of grain boundaries and therefore the amount of hydrogen on the grain boundaries increases and for films thicker than 25 nm, columnar growth of the  $\mu$ c-Si:H material is observed. For the transition of a-Si:H to  $\mu$ c-Si:H a decreasing total decreasing hydrogen content in the films was observed. It was also found that the amount of hydrogen in surface-like peaks in the ATR-FTIR spectra of the films is an indication of microcrystallinity.

More extensive investigations using SE and ATR-FTIR in parallel will soon be carried out using the new Depo 2 setup at the TUE, which has been specifically designed with this purpose in mind. However, the results obtained so far using ATR-FTIR have shed new light on the SE analysis described earlier (*Figure 3-9*). By showing ATR-FTIR results which show the evolution of surface like modes in the microcrystalline material (as well as the high-stretching mode (HSM) and low stretching mode (LSM)) in tandem with the SE results described earlier we are forced to conclude that a real physical effect is being shown by the peak in the SE surface roughness. This peak corresponds to the emergence and stabilisation of surface like bonding modes in the material as clearly illustrated by ATR-FTIR. Moreover, the increase, and subsequent decrease, in the number of surface like modes over time is entirely consistent with, and leads us inevitably towards, the model previously proposed for microcrystalline silicon growth. The number of surface-like modes, which are believed to be present at grain boundaries, increases as the microcrystalline material nucleates before reaching a maximum during coalescence. The results from both techniques show this coalescence at approximately 25 nm.



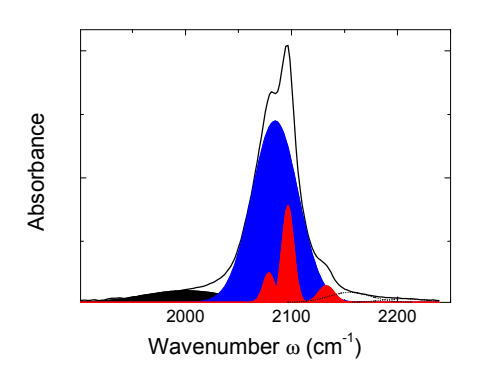


Figure 3-9-a ATR-FTIR results from mc-Si:H deposited at R = 200

Figure 3-9-b: Deconvolution of absorbance peaks showing the areas coresponding to the high-stretching modes, low-stretching mode and surface-like mode.

Through the combination of these two techniques we have established that the  $\mu$ c-Si:H coalescence peak commonly observed in spectroscopic ellipsometry does correspond to a physical effect. In addition, ATR-FTIR shows that this effect is entirely consistent with the assumed model for microcrystalline growth.

# 3.7 Construction of new deposition setup

The specifications of the newly constructed deposition setup are fully described in Appendix C. This setup was constructed to coincide with the relocation of the lab space of the ETP group into a new building. The new setup is similar to that previously used in that it comprises both load lock and reactor. However, the reactor and many other pieces of equipment are entirely new and many improvements and modifications have been made both to the original design and to the controlling software. The most notable of these is the increased number of ports on the reactor that now allows simultaneous measurement using both SE and ATR FTIR.

#### 3.8 Future work

Investigations into the exact role of temperature in the deposition of  $\mu$ c-Si:H material using the ETP technique are currently being conducted using spectroscopic ellipsometry as well as other techniques such as FTIR. These investigations will be complete by September 2003. By employing additional methods of fitting the SE data, such as EMA models, and comparing these to techniques such as Raman spectroscopy and XRD it is also hoped that SE will become a quick and reliable method of measuring crystalline content.

More extensive investigations into the effect of oxidation will also be carried out in the near future in order to ascertain the scale of the challenge that this represents and to determine whether it is possible to use this phenomenon as a diagnostic tool to determine the quality of deposited material.

Over the next year spectroscopic ellipsometry will be carried out in conjunction with ATR-FTIR to elucidate and optimise the growth of high rate  $\mu$ c-Si:H deposited using the ETP technique.

Phase diagrams have been used to determine the exact conditions which could be used to optimise the growth of low rate  $\mu$ c-Si:H<sup>1</sup>. For example, it is possible that by varying silane flow during a deposition a large degree of control can be exerted over the deposited material. By depositing a microcrystalline layer as a seed layer it is possible that the crystallinity of any

subsequent layer will be increased. In the future phase diagrams will be constructed through the evaluation of a wide range of deposition conditions to represent the deposition of  $\mu$ c-Si:H using the ETP technique.

# 3.9 Publications

# Submitted for publication in Thin Solid Films:

Deposition of hydrogenated microcrystalline silicon at growth rates in excess of 1 nm/s using the expanding thermal plasma technique. I.J. Houston, E.A.G. Hamers, W.M.M. Kessels, and M.C.M. van de Sanden.

High rate a-Si:H and mc-Si:H film growth studied by advanced plasma and in situ film diagnostics. W.M.M. Kessels, P.J. van den Oever, J.P.M Hoefnagels, J. Hong, I.J. Houston, and M.C.M. van de Sanden. Mat. Res. Soc. Symp. Proc. 715 (2002) A.25.6.

#### 3.10 Presentations

MRS Spring meeting Symposium A: Amorphous and nanocrystalline Si based films, San Francisco April 2003:

High-rate (> 1 nm/s) microcrystalline silicon film growth studied by in situ spectroscopic ellipsometry - combined with AFM, ATR-FTIR and TEM. I.J. Houston, J. Hong, P.J. van den Oever, W.M.M. Kessels, and M.C.M. van de Sanden

### FLTPD Conference, Lecce, Italy April 2003

Attenuated total reflection infrared spectroscopic study of hydrogenated amorphous and microcrystalline silicon film evolution, P.J. van den Oever, I.J Houston, M.C.M. van de Sanden, and W.M.M. Kessels

# Chelsea meeting, Cambridge April 2003:

High-rate (> 1 nm/s) microcrystalline silicon film growth - Studies using spectroscopic ellipsometry and atomic force microscopy. Iain Houston, J. Hong, P.J. van den Oever, W.M.M. Kessels, and M.C.M. van de Sanden

# WELTPP workshop, Rolduc November 2002:

The deposition of microcrystalline silicon using the remote expanding thermal plasma deposition technique. I.J. Houston, W.M.M. Kessels, M.C.M. van de Sanden

#### AVS International Symposium November 2002:

Plasma and in situ film diagnostic study of amorphous and microcrystalline silicon deposition. W.M.M. Kessels, J.P.M Hoefnagels, P.J. van den Oever, and M.C.M. van de Sanden.

# CPS Symposium, Lunteren March 2002. (Poster presentation):

The deposition of microcrystalline silicon using the remote expanding thermal plasma deposition technique. I.J. Houston, W.M.M. Kessels, C. Smit, M.C.M. Van de Sanden, D.C. Schram

# 4. MICROCRYSTALLINE SILICON FILMS AND SOLAR CELLS DEPOSITED BY ETP

C. Smit, R.A.C.M.M. van Swaaij and M.C.M. van de Sanden, Delft University of Technology & Eindhoven University of Technology

#### **Abstract**

Expanding thermal plasma chemical vapour deposition (ETP-CVD) has been used to deposit thin microcrystalline silicon films. We varied the position at which the silane is injected in the expanding hydrogen plasma: relatively far from the substrate and close to the plasma source, giving a long interaction time of the plasma with the silane, and close to the substrate, resulting in a short interaction time. The material structure is studied extensively. The crystalline fractions as obtained from Raman spectroscopy as well as from x-ray diffraction (XRD) vary from 0 to 67%. We found that when the silane is injected close to the substrate, the microcrystalline-to-amorphous transition occurs at higher silane flows. The deposition rate, however, is hardly influenced by the position of the injection ring, as is the refractive index. The average particle sizes vary from 6 to 17 nm as estimated from the (111) XRD peak using the Scherrer formula. Small angle x-ray scattering (SAXS) and flotation density measurements indicate void volume fractions of about 4 to 6%. When the samples are tilted the SAXS signal is lower than for the untilted case, indicating elongated objects parallel to the growth direction in the films.

Solar cells have been deposited with microcrystalline silicon intrinsic layers deposited by ETP-CVD. The microcrystalline doped layers were made by rf PECVD. The best performance was obtained for solar cells of which the ETP-CVD layer was deposited with the injection ring close to the substrate. At a deposition rate of 0.2 nm/s the best efficiency was 1.86%; at 1.2 nm/s this was 1.52%.

#### 4.1 Introduction and aim

In the previous report we showed that microcrystalline silicon ( $\mu$ c-Si:H) can be deposited at high deposition rates using expanding thermal plasma chemical vapour deposition (ETP-CVD). Deposition rates as high as 4.7 nm/s were achieved, however, the quality of that material was inferior and deemed not suitable for solar cell devices. In this report we will present results of continuing work, in which we aimed to optimise the material quality of  $\mu$ c-Si:H deposited with ETP-CVD.

The report is organised as follows. First we will briefly describe the experimental set-ups and techniques that have been used. Then we will present results on the material optimisation, which is followed by the latest results of solar cells that of which the intrinsic layer has been deposited with ETP-CVD.

# 4.2 Experimental

At TUD the depositions were carried out in the so-called CASCADE machine. This system has been especially built on earlier Novem projects. This machine consists of three connected vacuum chambers: one chamber is for the deposition of doped layers using radio-frequent plasma enhanced chemical vapour deposition (rf PECVD), another chamber for the deposition of intrinsic layers with ETP-CVD, and a third chamber as load lock that connects the PECVD and ETP-CVD chambers. Details of the system have been published elsewhere [1].

Essential for the deposition of  $\mu$ c-Si:H is that the silicon precursor, silane (SiH<sub>4</sub>), is heavily diluted with hydrogen (H<sub>2</sub>). Therefore, a large series of samples have been deposited in which the H<sub>2</sub> dilution was varied. The experiments reported here were all carried out on samples deposited using a 4.0-mm diameter arc channel. This arc allows the use of pure hydrogen (H<sub>2</sub>) instead of an argon-hydrogen mixture. All depositions were carried at a deposition temperature of 300°C. In addition to the hydrogen dilution, also the position of the injection ring with respect to the substrate appeared to be a crucial parameter. This distance has been varied between 470 mm and 55 mm. We think that by varying the ring-to-substrate distance the species that arrive at the growing surface are somewhat controlled. We will elaborate on that in the next section.

Structural analysis was carried out on the layers using Raman spectroscopy, x-ray diffraction (XRD), and small-angle x-ray scattering (SAXS). With Raman spectroscopy the amorphous-to-crystal ratio is determined, using a procedure developed by C. Smit *et al.* [2]. In this procedure the amorphous and crystalline contributions to the Raman spectra of the microcrystalline silicon films are separated by the subtraction of a Raman spectrum of an *a*-Si:H sample. The scaling factor needed in the subtraction to obtain a flat background is related to the fraction of amorphous material and the peak area in the remaining spectrum is related to the crystalline material fraction. XRD was carried out by Prof. D. Williamson at the Colorado School of Mines and analysed using a method described in Ref. 3. In addition to XRD, he also carried out SAXS and flotation density measurements.

The most promising  $\mu c$ -Si:H layers were incorporated as the intrinsic layer in a p-i-n solar cell. These solar cells consist of glass covered with Asahi U-type TCO, a 30-nm rf PECVD  $\mu c$ -Si:H p-layer, a 1000-nm or 2000-nm  $\mu c$ -Si:H i-layer deposited by ETP-CVD, a 30-nm rf PECVD  $\mu c$ -Si:H n-layer, and an Ag/Al back contact. The performance of the solar cells was measured using an Oriel solar simulator. In addition the quantum efficiency of the cells was measured.

<sup>[1].</sup> B. A. Korevaar, Ph. D. Thesis, Eindhoven University of Technology, 2002.

<sup>[2]</sup> C. Smit, R. A. C. M. M. van Swaaij, H. Donker, A. M. H. N. Petit, W. M. M. Kessels, and M. C. M. van de Sanden, J. Appl. Phys. 94(5), 3582 (2003).

<sup>[3].</sup> D. L. Williamson, Mater. Res. Soc. Symp. Proc. 557, 251 (1999).

# 4.3 Results on ETP microcrystalline silicon layers

For the deposition of device-quality amorphous silicon (a-Si:H) with ETP-CVD silane (SiH<sub>4</sub>) is mainly dissociated in SiH<sub>3</sub> radicals [4]. In that case only just sufficient hydrogen is added to the arc to dissociate the SiH<sub>4</sub> to SiH<sub>3</sub>. For µc-Si:H deposition a large amount of hydrogen is added to the precursor gas with the aim to create a high density of atomic hydrogen at the growing surface. We think that this atomic hydrogen preferentially etches the weak bonds thus promoting the growth of uc-Si:H. However, for these uc-Si:H deposition conditions it was suggested that the excess atomic hydrogen abstracts more hydrogen atoms from the SiH<sub>3</sub> radical resulting in SiH<sub>2</sub>, SiH, and even Si [5]. This is schematically shown in Figure 4-1(a). It is generally accepted that these radicals do not contribute to the growth of device-quality material. In order to control the species that arrive at the growing surface, whilst still maintaining a high atomic hydrogen density we investigated the influence of the SiH<sub>4</sub> injection position with respect to the substrate. The idea is that by moving the injection ring towards the substrate we are able to suppress the formation of SiH<sub>x</sub> ( $x \le 2$ ). Doing this simply does not allow hydrogen abstraction reactions to occur as shown in Figure 4-1(b). The high atomic hydrogen density at the growing surface is still guaranteed, as the dilution ratio is not altered. In the remainder of this section we will show results of the material quality for two different ring-to-substrate distances.

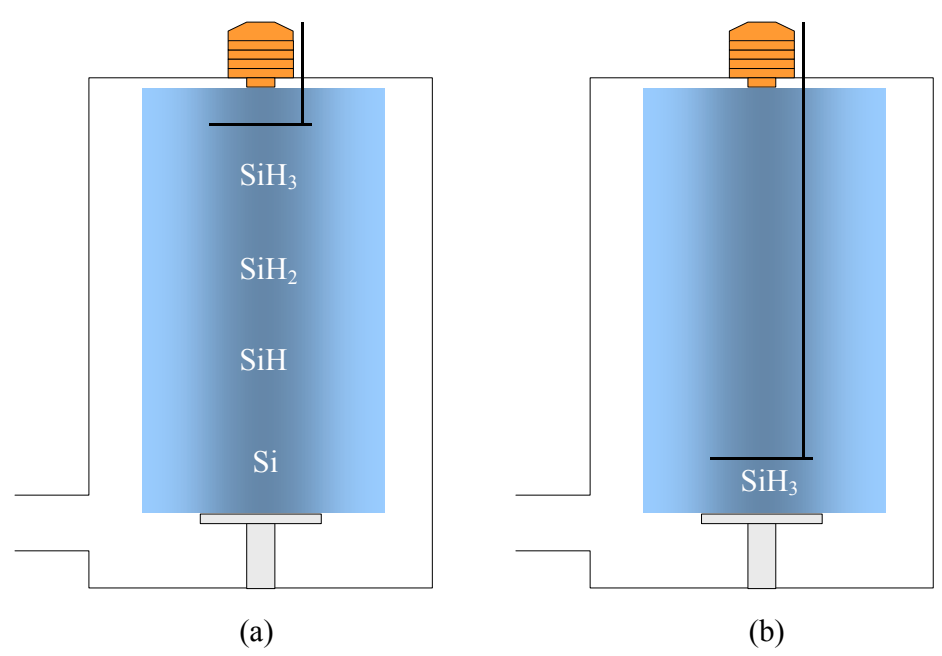


Figure 4-1 Schematic representation of radical formation in a ETP-CVD plasma when using mc-Si:H deposition conditions: (a) high injection ring position and (b) low injection ring position.

In Figure 4-2 the crystalline mass fraction (as determined from Raman measurements), the growth rate, and the refractive index at 2 eV are shown as a function of the SiH<sub>4</sub> flow for two different ring-to-substrate distances. It can be observed that the microcrystalline-to-amorphous transition (taken at 50%) moves to higher SiH<sub>4</sub> flows when the ring-to-substrate distance is reduced. Reducing this distance remarkably has virtually no effect on the growth rate. Furthermore, the refractive index at 2 eV, which is used as a measure of the material density, does not become smaller or even seems to increase. The larger refractive index indicates that the material is denser and suggests that moving the ring towards the substrate improves the material quality.

<sup>[4].</sup> W. M. M. Kessels, M. C. M. van de Sanden, and D. C. Schram, J. Vac. Sci. Technol. A 19(3), 1027 (2001).

<sup>[5].</sup> C. Smit, E. A. G. Hamers, B. A. Korevaar, R. A. C. M. M. van Swaaij, and M. C. M. van de Sanden, J. Non-Cryst. Solids 299-302, 98 (2002).

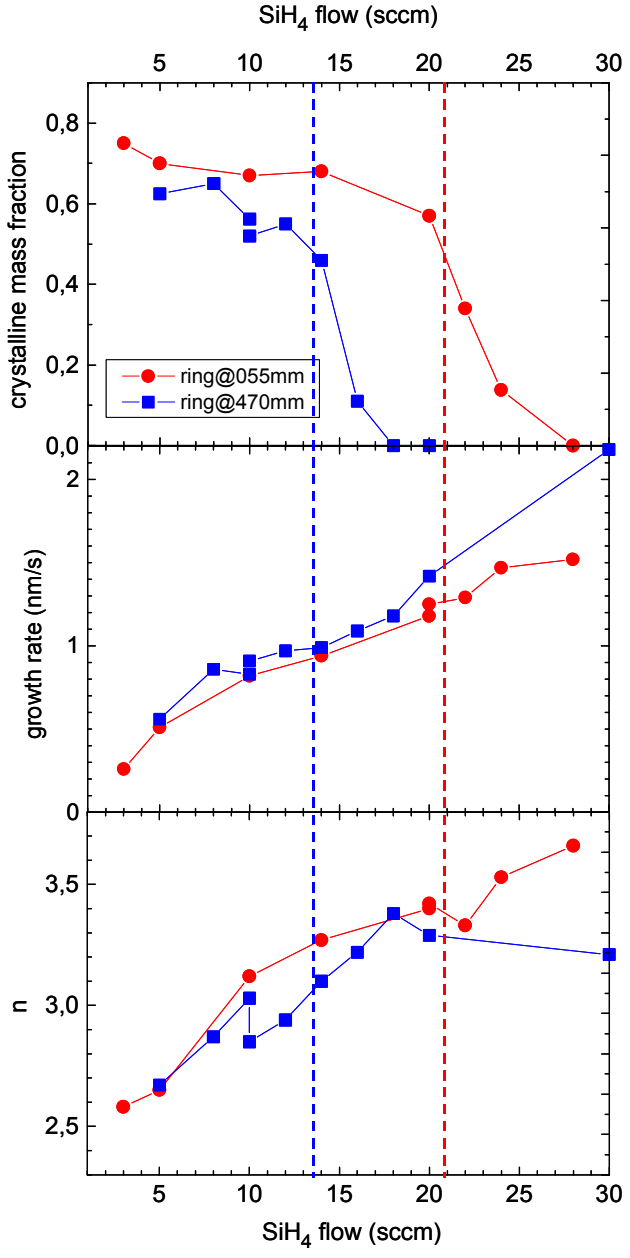


Figure 4-2 The crystalline mass fraction, the growth rate, and the refractive index at 2 eV, n, as a function of the SiH<sub>4</sub> flow for two different ring-to-substrate distances.

Some films were also investigated by XRD, SAXS and flotation density measurements. The results are summarised in *Table 4-1*. The crystalline fractions obtained from XRD and Raman measurement are in good agreement with each other (within 10%). The average crystallite size from the XRD measurements varies depending on which diffraction peak is used for the calculation. No clear trend is visible and the sizes range from approximately 5 to 20 nm. For a film deposited using the conditions of sample #3 a HRTEM analysis was carried out (not shown here). From this image we estimated the average particle size to be  $9.5 \pm 4.5$  nm.

The results of the flotation density measurements are also shown in *Table 4-1*. The films that are deposited with the SiH<sub>4</sub> injected near the substrate generally have a slightly higher mass density, indicating a lower void fraction. The void fractions are calculated from the mass density deficits compared to *c*-Si (2.33 g/cm<sup>3</sup>). The SAXS results, however, show no difference for the two injection positions, as shown in *Figure 4-3*. An important single quantity extracted from the

SAXS data is the integrated intensity [6], which is a good measure of the total inhomogeneity in each sample. The total scattering intensity is high compared to the device quality *a*-Si:H film (*Figure 4-3*(b)). Assuming spherical scattering objects the size distribution can be fitted to the data. The average object sizes obtained from the non-tilted samples are shown as <D> in *Table 4-1*. The significant drop in intensity for the tilted samples shows that oriented scattering objects that are elongated and aligned with the growth direction are found in all samples. This is confirmed by the TEM bright-field image of sample #3 (not shown here). Because of this anisotropic scattering a model based on ellipsoidal scattering objects is used to calculate the void fraction, assuming all scattering intensity is due to voids. Therefore, these values should be interpreted as an upper limit on the void fractions. This could explain the disagreement with the void fractions from the flotation density measurements. However, since the scattering intensities are the same for the amorphous and the microcrystalline samples we assume that the crystallites do not contribute significantly to the SAXS signal. Details on the interpretation of SAXS measurements are described in Ref. 6.

Table 4-1: Experimental results on the material structure. Q is  $SiH_4$  flow,  $f_c$  and  $f_v$  are the crystalline and void fractions, respectively,  $\rho$  the mass density, 'flot.' indicates that this is determined by flotation-density measurements,  $\langle D \rangle$  is the average void size, n the refractive index, L the average crystallite size determined by applying the Scherrer formula to the (111), (220), and (311) peak, respectively. Because a second peak was needed to fit the 220 peaks correctly for the lower sample series, two crystallite sizes are presented.

nr	Q (SiH <sub>4</sub> ) (sccm)	f <sub>c</sub> XRD		ρ (g/cm³) flot.	f <sub>v</sub> flot.	f <sub>v</sub> SAXS	<d></d>	n at 2 eV	c <sub>H</sub> (at%)	L (111)	L (220)	L (311)	rate (nm/s
	Injection @ 365 mm above substrate												
#3	10	0.58	0.57	2.19	0.060	0.084	7.6	2.97	3.1	17.2	6.4	7.0	0.91
#4	14	0.50	0.46	2.20	0.056	0.071	8.1	3.10	5.9	10.1	5.5	7.0	0.99
#1	16	0.12	0.11	2.17	0.069	0.052	8.5	3.22	8.5	6.6	6.9	7.2	1.09
#2	18	0.00	0.00	2.17	0.069	0.063	8.0	3.38	7.8				1.18
	Injection @ 55 mm above substrate												
#5	14	0.60	0.67	2.23	0.043	0.093	7.7	3.12	3.7	14.6	25/4.6	8.0	0.94
#6	20	0.60	0.59	2.22	0.047	0.076	7.6	3.30	4.1	12.3	20/4.7	7.5	1.18
#7	22	0.42	0.47	2.21	0.052	0.105	8.0	3.30	4.0	12.1	11/3.8	6.8	1.29
#8	28	0.00	0.00	2.18	0.064	0.062	7.8	3.65	7.6				1.52

The change of the precursor gas injection position from 365 to 55 mm above the substrate leads to an increase in refractive index for films with comparable crystalline fractions (see *Figure 4-2* and *Table 4-1*). As we noted before, this suggests that the material is denser as the injection position is lowered, which is corroborated by the flotation density measurements. Indeed a drop in void fraction of  $\sim 25\%$  is observed for material deposited with the injection position near the substrate. However, the SAXS measurements indicate an equal void density in case all the scattering intensity is attributed to voids, as discussed above. In the following section we will present some results of solar cells that employ the layers with the most promising properties.

<sup>[6].</sup> D. L. Williamson, Mater. Res. Soc. Symp. Proc. 377, 251 (1995).

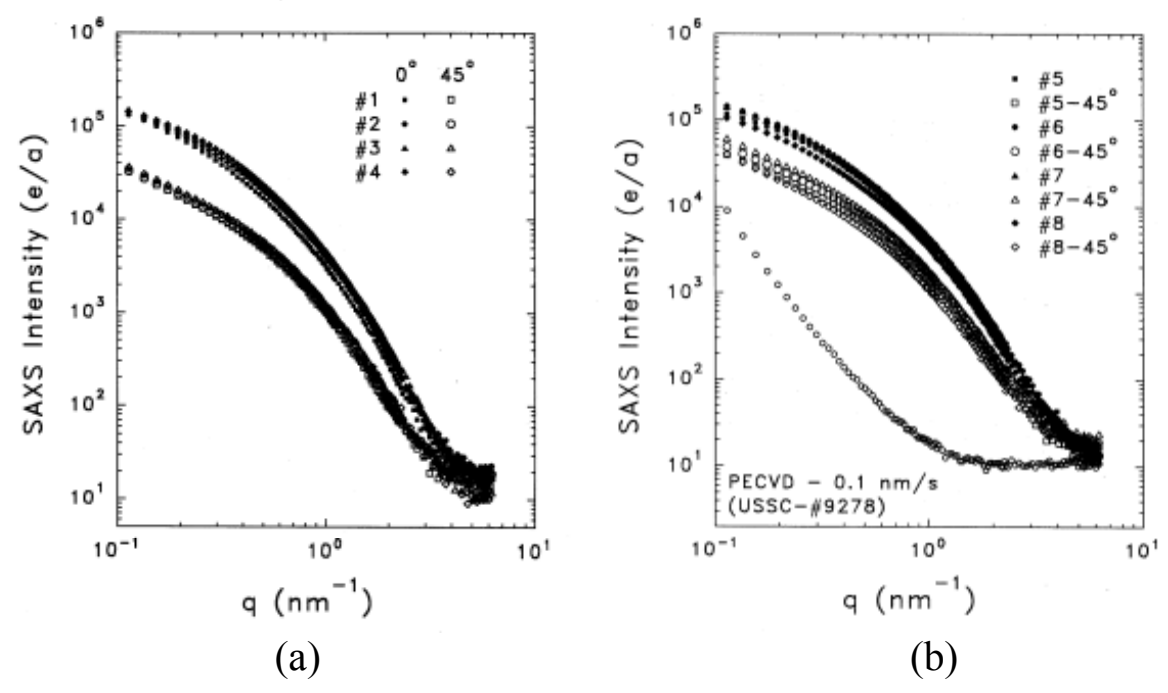


Figure 4-3: SAXS measurement of 5-µm thick silicon films deposited using (a) 10, 14, 16, and 18 sccm  $SiH_4$  (nr. 3, 4, 1, and 2, respectively) injected into the reaction chamber at 365 mm above the substrate and (b) 14, 20, 22, and 28 sccm  $SiH_4$  (nr. 5, 6, 7, and 8 respectively) injected at 55 mm above the substrate. Open symbols represent measurements with the sample tilted 45°. The momentum transfer  $q = (4\pi/\lambda)\sin\theta$ , where  $2\theta$  is the scattering angle and  $\lambda$  is the wavelength (0.154 nm). The unit for the scattering intensity is electrons/atom (e/a). For comparison in (b) the SAXS signal from a device quality a-Si:H sample from USSC is shown.

# 4.4 Results on ETP microcrystalline silicon solar cells

Solar cell results also indicate that the change in injection position leads to a change in material quality. We prepared solar cells using the conditions of sample #3 and #6 (see *Table 4-1*) for the deposition of the intrinsic layer in p-i-n devices. The results are shown in *Table 4-2*. Clearly, the solar cell deposited with the SiH<sub>4</sub> injected close to the substrate performs much better. In particular the low short-circuit current density,  $J_{\rm sc}$ , of these cells is noted. This low current density indicates a very low collection of photogenerated charge carriers, which in turn suggests a high defect density. Also, many cells are shunted when using a high injection position, which is not the case if SiH<sub>4</sub> is injected near the substrate.

In an attempt to increase the  $J_{\rm sc}$ , cells were deposited with a 2000-nm thick  $\mu$ c-Si:H layer at the low SiH<sub>4</sub> injection position. These cells were prepared with the injection ring at 55 mm. Indeed some improvement of the performance is observed; at a deposition rate of 0.2 nm a conversion efficiency of 1.9% was obtained, the highest value obtained for a  $\mu$ c-Si:H solar cell deposited by ETP-CVD. At a deposition rate of 1.2 nm/s an efficiency of 1.5% was found.

The performance of the cells made so far is still too low for implementation in tandem solar cells. However, we must note that the solar cells do not have a ZnO backreflector, which is expected to improve the  $J_{\rm sc}$  of the cell significantly. Nevertheless it is interesting to investigate the discrepancy with well performing  $\mu$ c-Si:H solar cells reported in literature. For this purpose spectral response measurements have been carried out (not shown here). These measurements reveal that in particular for wavelengths higher than 500 nm the response drops dramatically. Comparison of our results with those obtained on VHF-PECVD  $\mu$ c-Si:H solar cells of the

University of Neuchâtel [7] suggests that incorporation of oxygen due to the use of low-purity hydrogen suppresses the performance significantly.

Table 4-2: Solar cells consisting of glass covered with Asahi U-type TCO, a 30-nm  $\mu$ c-Si:H p layer, a  $\mu$ c-Si:H i layer, a 30-nm  $\mu$ c-Si:H n layer, and an Ag/Al back contact. The intrinsic layer is deposited using the conditions of samples #3 and #6 for the high and the low injection position, respectively.

H <sub>2</sub> flow is 2000 sccm, thickness μc-Si:H i layer is 1000 nm								
SiH <sub>4</sub> (sccm)	SiH <sub>4</sub> injection	Dep. rate (nm/s)	$V_{\rm oc}\left(\mathrm{V}\right)$	$J_{\rm sc} ({\rm A/m}^2)$	FF	h (%)		
10	365 mm	0.8	0.22	10.6	0.33	0.10		
20	55 mm	1.2	0.38	75.0	0.44	1.24		
SiH <sub>4</sub> injection at 55 mm, thickness μc-Si:H i layer is 2000 nm								
SiH <sub>4</sub> (sccm)	H <sub>2</sub> (sccm)	Dep. rate (nm/s)	$V_{oc}(V)$	$J_{\rm sc}~({\rm A/m^2})$	FF	h (%)		
9	1500	0.2	0.39	103	0.46	1.86		
20	2000	1.2	0.38	80	0.50	1.52		

<sup>[7].</sup> P. Torres, Ph. D. Thesis, University of Neuchâtel, 1998.

# 5. CHARACTERIZATION OF μC-SI

H.Donker and A. Goossens, Delft University of Technology

#### 5.1 Introduction

The aims of the contributions of TAC to the MissionN and Miracle project were the characterization of and development of new characterization tools for microcrystalline silicon ( $\mu$ c-Si) layers. Some standard techniques (p.e. XRD) were already available at the beginning of the project, for others (Raman, Photoluminescence (PL), Transient Absorption (TA), Time of Flight (TOF)) set-ups have been built and/or modified. Raman and XRD have been used on hundreds of samples throughout the entire project as standard techniques to determine amorphous/crystalline ratio, crystallite size and orientation. For the results of these measurements as a function of growth conditions we refer to previous chapters in this report.

# 5.2 Raman / Photoluminescence spectroscopy

In the first year of the project a flexible Raman and Photoluminescence set-up has been built, which has been extensively described in [1] Since then the set-up has been extended with a closed cycle liquid Helium cryostat (APD Cryogenics) which allows for measurements down to a temperature of ~9 K. Also a polarizing filter (Polaroid type HNB) can be placed in the detection path. Polarized Raman spectra can yield (additional to XRD) information about the orientation of crystallites in the samples

Correction factors for the wavelength dependent throughput of the monochromator and the sensitivity of the CCD chip have been determined by comparing the spectrum of a calibrated tungsten halogen lamp measured on our set-up with the known output of this lamp.

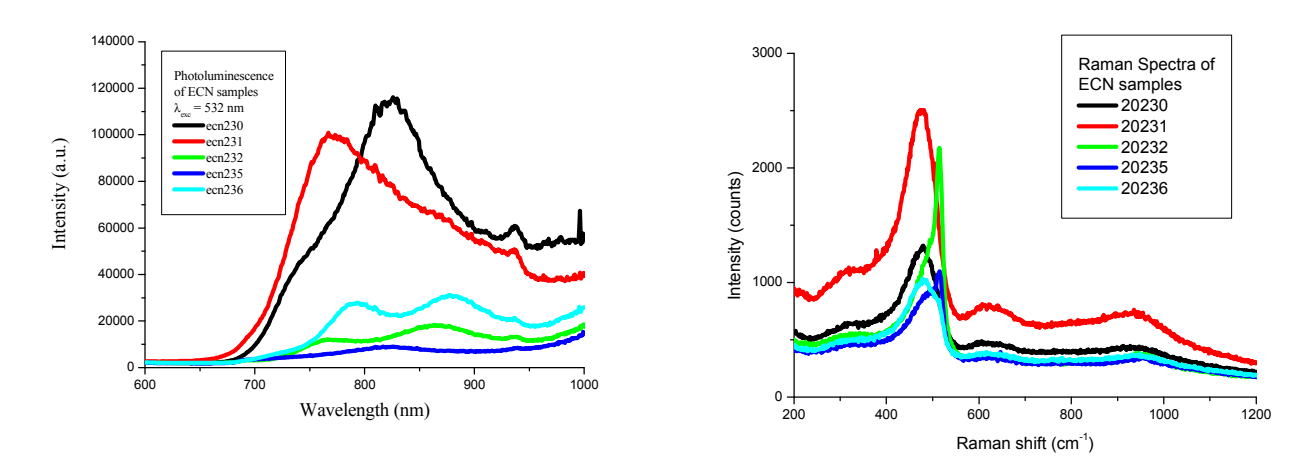


Figure 5-1(a) Photoluminescence spectra of several ECN samples at 9K, spectra have been corrected for throughput of the monochromator and sensitivity of the CCD camera (b) Raman spectra of these samples.

A few typical luminescence spectra obtained for ECN samples are shown in *Figure 5-1*, together with the Raman spectra obtained for the same samples. For samples from Utrecht and Dimes with comparable a-Si/c-Si fraction ratios, similar luminescence spectra have been observed. Comparison of Raman and PL spectra shows that effective luminescence is only observed for samples in which the 520 cm<sup>-1</sup> Raman peak of crystalline Si is not or hardly

ECN-C--04-009 51

-

<sup>[1].</sup>W.J. Soppe, C. Devilée, A.C.W. Biebericher, S.E.A. Valster-Schiermeier, A.M.H.N. Petit, C. Smt, R.A.C.M.M. van Swaaij, I. Houston, M.C.M. van de Sanden, A. Gordijn, J.K. Rath, R.E.I. Schropp, H. Donker, a. Goossens, Progress Report Missionn & Miracle, Period 1 july 2001 to 30 june 2002, ECN-CX-02-116

observable. The observed luminescence is similar to that observed for Si nanoparticles in a  $SiO_2$  matrix [2] and porous Si[3]. The luminescence of the latter is also ascribed to Si nanoparticles. Due to the quantum size effect these particles show luminescence at energies above the bandgap of bulk Si. The luminescence in *Figure 5-1* is therefore also ascribed to Si nanoparticles in the amorphous Si matrix. Although difficult to quantify, the presence of this luminescence indicates that not too many quenching defects are present in these crystallites or at their boundary with the amorphous fraction. The fact that the luminescence of sample 20230 is red shifted compared to sample 20231 indicates that in the former sample the nanocrystalites are slightly larger. The presence of weak luminescence in the other samples might indicate a small fraction of  $\sim$ 3-6 nm crystallites in them.

An interesting question is whether there is energy/exciton transfer from the amorphous phase to the crystalline phase in these samples. The samples were excited with 532 nm laser light, i.e. a wavelength where the amorphous Si is strongly absorbing. The observed high intensity of the luminescence suggests that energy/exciton transfer might be present. Solid evidence for the suggested exciton/energy transfer process might be found in photoluminescence excitation (PLE) spectra or with time resolved luminescence measurements. PLE measurements are however not possible with our equipment. A time resolved PL set-up has been built recently, but unfortunately no measurements on Si samples have been performed yet.

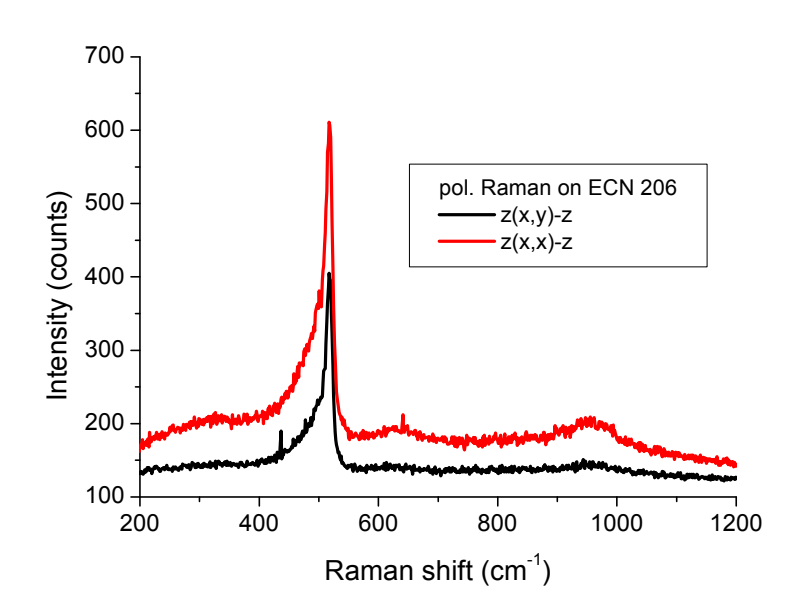


Figure 5-2: Polarized Raman spectra of ECN sample 20206.

In *Figure 5-2* an example of polarized Raman spectra is given. XRD data on this sample indicate a preferred (111) orientation of the crystallites. However, in XRD spectra the expected intensity for the (004) reflection is very low, for some samples this intensity is so low that it can not be distinguished from the noise in the spectra, and in the (011) direction no reflections are observed at all. The spectra shown in *Figure 5-2* exclude the possibility of a preferred (001) or (011) orientation of the crystallites. In fact the observed intensity ratio of the 520 cm<sup>-1</sup> peaks, in the spectra shown (1.7), is very close to that expected for (111) oriented crystallites (1.5) [4] and thus confirms the conclusion drawn from the XRD results.

52 ECN-C--04-009

<sup>[2].</sup>S. Furukawa, T. Miyasato, Jpn. J. Appl. Phys. 27, L2207, (1989), D. Zhang, R.M. Kolbas, P.D. Milewski, D.J. Lichtenwalner, A.I. Kingon, J.M. Zavada, Appl. Phys. Lett. 65, 2684 (1994).

<sup>[3].</sup>L.T. Canham, Appl. Phys. Lett. 57, 1046 (1990), V. Lehmann, U. Gösele, Appl. Phys. Lett. 58, 856 (1991)

<sup>[4].</sup>F.H. Pollak in Chemical Analysis, Vol. 114 Analytical Raman Spectroscopy, New York, Wiley, 1991, Chapter 6.

# 5.3 Transient Absorption spectroscopy

An important parameter for the performance of a solar cell material is the lifetime of the free carriers generated upon illumination. Free carriers give rise to an absorption in the NIR region of the optical spectrum. Transient spectroscopy in this region can thus in principle give information about the lifetime of the free carriers. For this purpose a transient absorption set-up already available in Delft at the beginning of the project has been modified and optimised for use with  $\mu$ c-Si samples [1].

In [1] we already reported that the magnitude and sign of the transient signal for the µc-Si samples depends strongly on probe wavelength, layer thickness and orientation of the sample. To calibrate the set-up, silicon nitride coated float-zone Si samples with known lifetimes (in the range of 1 ms) were tried as a reference first. However, these SiN layers transmitted hardly any NIR probe light and no transients could be measured. As an alternative reference sample we used a double polished uncoated Si-wafer. The lifetime of the free carriers in this wafer was measured at the ECN with two techniques, i.e. Quasi Steady State Photo Conductance (QSSPC), which gave a lifetime of 15 µs, and Modulated Free Carrier Absorption (MFCA), 22 µs. The latter technique is closely related to the presently described Transient Absorption technique, the main difference being that MFCA works in the frequency domain, while TA works in the time domain. In TA a bi-exponential decay with lifetime components of 3 and 30 us were found. These results are in good agreement with the values found with OSSPC and MFCA. The results found for this wafer on our set-up were independent of sample orientation (0-70 degrees), probe wavelength (1200-1600 nm) or pump wavelength (532-1072 nm) used, contrary to the results for the uc-Si samples. For these samples the magnitude and even the sign of the transient absorption signal was strongly dependent on these parameters. The measurements on the Si wafer show that these results are not due to an artefact in our set-up. The only logical explanation for them is that they are due to the interplay of changes of the complex dielectric constant and interference effects in the Si layers studied. (The thickness of the layers is of the same order of magnitude as the wavelength of the probe light used). Due to these effects it is not possible to determine whether the observed signal is in deed caused by absorption of free carriers or a bleaching of localized states within the mobility gap of the amorphous fraction.

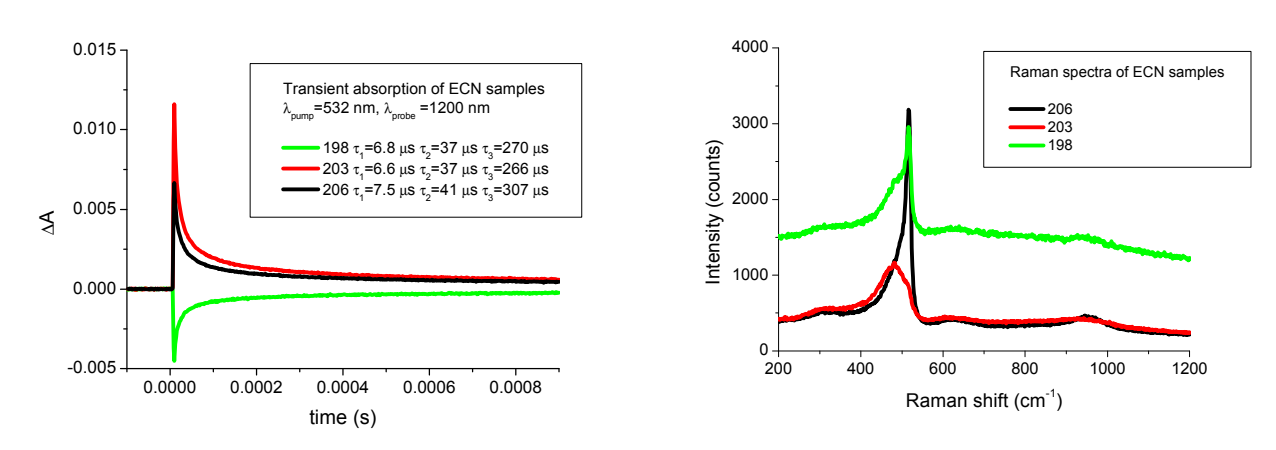


Figure 5-3: a) Transient absorption measurements on some ECN samples. The life times in the insert are the best fit results to a three-exponential decay function (b) Raman spectra of these samples.

A detailed analysis of the transient absorption signals measured showed that the time dependence of the signal could best be fitted with a three exponential decay function.(with  $\tau = 7$ , 40 and  $\sim 300~\mu s$ , respectively) Not only the lifetimes but also the ratio of the pre-exponential factors was found to be independent of the a-Si/c-Si fraction in the samples made with the same deposition technique. Small differences between ECN and Dimes samples were found,

however. This strongly suggests that the observed signal is coming from the amorphous fraction in the layers only. The long lifetimes observed cannot be ascribed to free carrier lifetimes, but have to be related to either trapping and de-trapping of charge carriers at defect sites in the layer or a bleaching of localized states within the mobility gap.

Measurements at longer probe wavelengths might resolve these interpretation problems. Not only is free carrier absorption expected to be much stronger there, theoretically it increases with the square of the wavelength, but at much longer wavelengths the alleged interference effects will be suppressed also. Modifications on the set-up to extend the measurement range up to 5000 nm are still in progress, however.

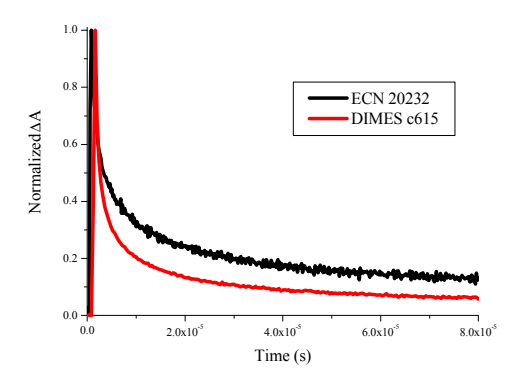


Figure 5-4: Comparison of transient absorption for a ECN and a DIMES sample. The change in absorbance has been normalized for both measurements.

Measurements made at nanosecond timescales did not show any build up slower then the half width of the laser pulse, i.e. no evidence for a possible (excitation) energy or electron transfer process was found.

Contrary to the Si wafer, for  $\mu$ c-Si samples, no transient signals between 1200 and 1600 nm probe wavelength, could be observed for pump wavelengths ranging from 710 - 1100 nm, using the idler beam of the MOPO. These pump wavelengths are assumed to mainly excite the crystalline fraction in the samples. The absence of any observable signal might be due to the fact that the intensity of the laser and/or the absorption in these thin samples is too weak. However the intensity of our laser in this region is only about a factor two or three lower than at 532 nm, and for the Si wafer the difference in signal was not very big at these wavelengths. Probably, the lifetime of free carriers in the crystalline fraction is too short (< 2 ns) to be observable with our set-up, which might form an indication for the poor performance of these layers in a device.

# 5.4 Time of Flight measurements

A time of flight (TOF) set-up as shown schematically in *Figure 5-5* has been built. This set-up is integrated with the Transient Absorption set-up, described above. When sample are equipped with transparent or semi-transparent contacts TOF and TA measurements can in principle be performed simultaneously. The laser system and digital oscilloscope are the same as in the TA set-up. An Agilent 3325GA, 80MHz Function/Arbitrary Waveform Generator is used to put a square wave bias pulse on the sample several µs before the laser pulse arrives. This ensures a homogeneous field in the sample during the measurement. A continuous DC bias would result into a non-homogeneous field due to dielectric relaxation [5].

<sup>[5].</sup> G.F. Seijnhaeve, R.P. Barclay, G.J. Adriaenssens, J.M. Marshall, Phys. Rev. B 39, 10196 (1989)

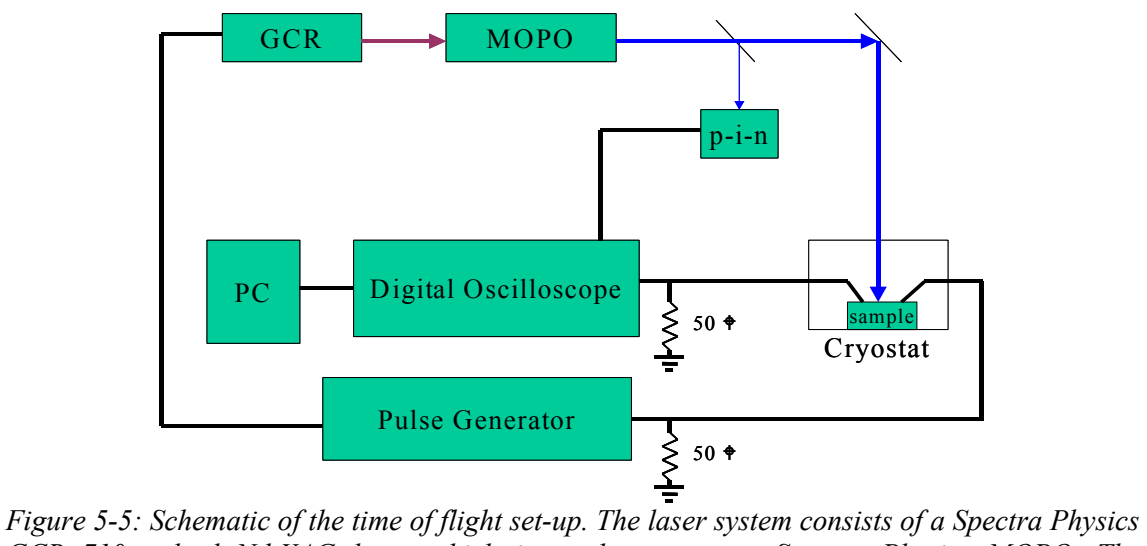


Figure 5-5: Schematic of the time of flight set-up. The laser system consists of a Spectra Physics GCR 710 pulsed Nd:YAG laser which is used to pump a Spectra Physics MOPO. The oscilloscope is a Tektronix TDS 744, 500 MHz Digitizing Oscilloscope and the pulse generator an Agilent 3325GA, 80MHz Function/Arbitrary Waveform Generator. The sample is placed in a grounded Oxford Instruments Liquid Nitrogen Cryostat, which also functions as a Faraday cage to shield the sample from RF noise of the laser [6].

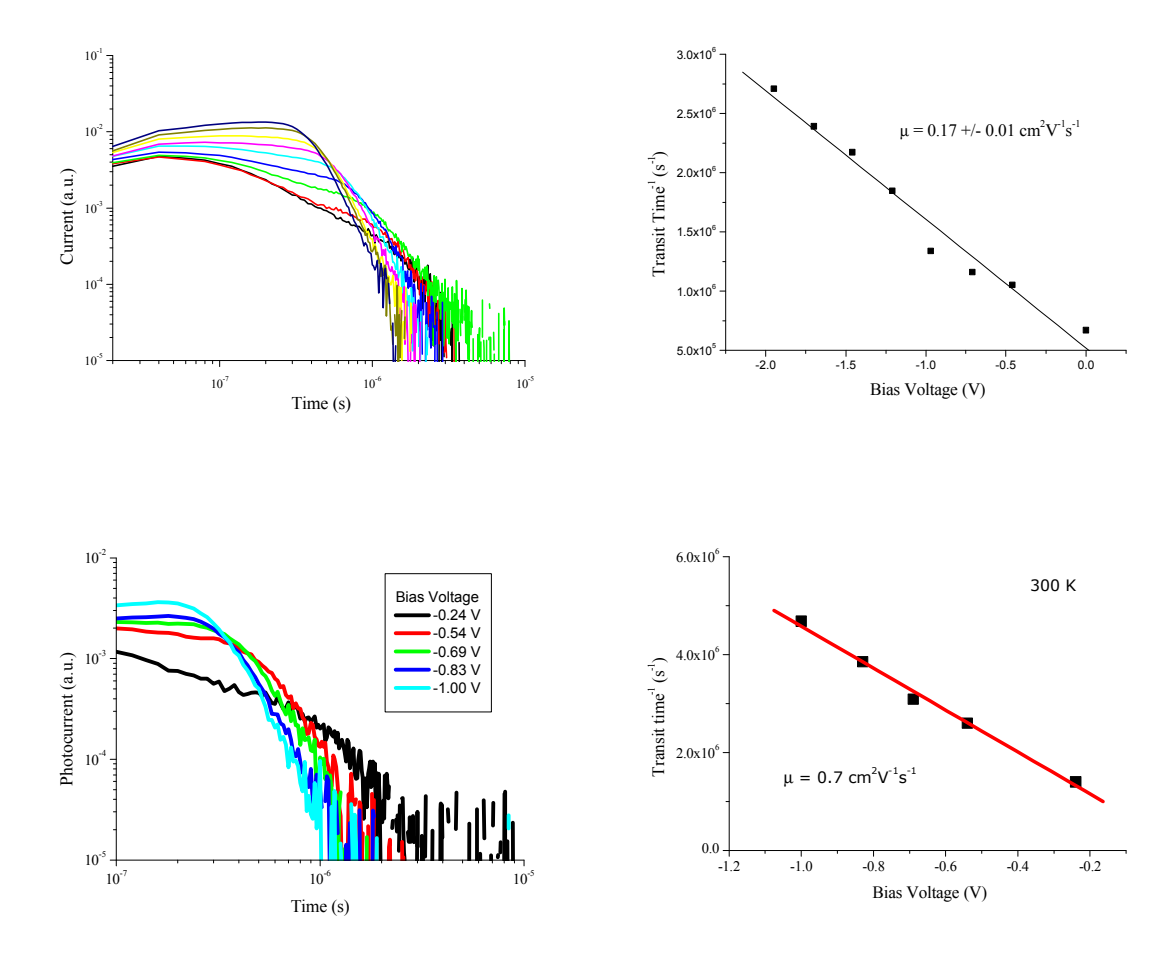


Figure 5-6: a) Time of flight electron transients for a 5  $\mu$ m thick amorphous Si sample at 240 K (b) Reciprocal transit time as a function of applied bias voltage at 240 K. (c)&(d) idem at 300K.

<sup>[6]</sup> T. Tiedje in Semiconductors and Semimetals, Vol 21 Hydrogenated amorphous silicon, Part C Electronic and transport properties, R.K. Willardson, A.C. Beer, J.I. Pankove eds., Orlando, Academic Press, 1984, Chapter 6.

Sample thickness is a critical parameter for TOF measurements. For Si samples a thickness of at least several microns is necessary. Up till now we have only been able to do measurements on a 5 micron thick and completely amorphous Si sample. Some preliminary results are shown in Figure 5-6. At room temperature an electron mobility of 0.7 cm<sup>2</sup>V<sup>-1</sup>s<sup>-1</sup> was found for this sample. This is in good agreement with values reported in literature for amorphous Si (0.9 - 1 cm<sup>2</sup>V<sup>-1</sup>s<sup>-1</sup>). Several samples provided by the partners in the project only had a thickness of about 1 micron. For these samples the RC time of the measuring circuit was of the same order of magnitude as the transit time, and therefore, TOF measurements on these samples were not possible. A deconvolution method proposed by Donovan [7] is being studied.

<sup>[7].</sup> K.J. Donovan, T. Kreouzis, J. Appl. Phys. 88, 918 (2000)

# 6. LBL DEPOSITIONS OF DOPED MICROCRYSTALLINE SI LAYERS

Aad Gordijn, J.K.Rath, Ruud Schropp, Utrecht University

# 6.1 Introduction

The aim is to develop thin microcrystalline silicon n- and p-type doped layers in a broad range of temperatures using the Layer-by-Layer (LbL) deposition method in order to obtain doped layers that are compatible with high growth rate microcrystalline i-layers in n-i-p or p-i-n solar cells. We had understood the need of such layers during our development of HWCVD grown poly-Si cell where standard PECVD grown microcrystalline doped layers (n and p layers) were used along with HWCVD grown poly-Si i-layer in an n-i-p cell configuration [1,2]. The main requirements for the doped layers are temperature stability and resistant to high atomic hydrogen fluxes. LbL method is promising because the growth and nucleation (by chemical annealing/etching) processes are separated, due to which the process can be tuned well. By this deposition technique we were able to develop special doped layers which otherwise cannot be made by the continuous (CW) growth method. Characterization techniques used are Raman spectroscopy, X-ray diffraction, Fourier transformed infrared spectroscopy (FTIR) and crosssectional transmission electron microscopy (X-TEM), UV-VIS spectroscopy, and temperature dependence of dark conductivity measurements (activation energy measurements). Plasma conditions are monitored by optical emission spectroscopy (OES) and Mass Spectroscopy (MS). Depositions are done in the ASTER deposition system. All the layers are grown using VHF (50 MHz) PECVD. In the LbL process, amorphous layers are grown by a normal silane and hydrogen mixed gas plasma, followed by a chemical annealing step with a hydrogen plasma. Adding trimethylboron (TMB or B(CH<sub>3</sub>)<sub>3</sub>)) to the aforesaid gas mixture, p-type doping is achieved, whereas n-type doping is obtained by adding phosphine (PH<sub>3</sub>).

# 6.2 Development of the µc-Si doped layers

LbL and CW doped layers have been deposited in the temperature range between 200 and 400 °C. The results can be summarized as follows:

- 1. Whereas in the CW case it is difficult to obtain crystalline doped layers at high temperatures, with LbL it is possible to develop a crystalline fraction that is high enough for percolation conduction (see *Figure 6-1* and *Figure 6-4*).
- 2. It has been possible by LbL method to obtain crystalline films even at high dopant concentrations. For the CW deposition, for example, increasing boron content has a severe effect on the nucleation. However, by the LBL deposition it is observed (*Figure 6-2*) that, by tuning the hydrogen treatment period, it is possible to increase the boron content in the film without any loss of crystallinity. This is possible because the boron incorporation and nucleation in the silicon matrix occurs at different stages of growth.
- 3. One of the important requirements for doped layers in device applications, that is met by the LbL growth, is low optical absorption. It is very clear from *Figure 6-3* that optical absorption of the doped LbL grown p-\muc-Si layer is better than that of the standard amorphous p-layer (a-SiC:H(B)) and the CW grown p-\muc-Si layer. This is an essential requirement of a window layer of the solar cell.

<sup>[1].</sup> J.K. Rath, F.D. Tichelaar and R.E.I. Schropp, Solid State Phenomena 67-68, 465 (1999).

<sup>[2].</sup> K.F. Feenstra, J.K. Rath, and R.E.I. Schropp, Proceedings of the 2<sup>nd</sup> World Conference on Photovoltaic Solar Energy Conversion, p. 956 (1998).

- 4. The percolation threshold for the doped LbL microcrystalline layers occurs at very small crystalline fractions; for n-type LbL microcrystalline silicon layer it is ~7-8 % crystalline fraction, whereas the threshold for p-type LbL microcrystalline silicon layer is ~12 %. The percolation threshold is observed from the transition of the conductivity path (as a sharp change of the conductivity value) as a function of the crystalline fraction in the film. This result is very significant, because this allows for very thin doped layers to be used in the solar cell.
- 5. The doping efficiency of the LbL high temperature grown p- $\mu$ c-Si layer is 39 % (the boron concentration of  $3.0 \times 10^{19}$  cm<sup>-3</sup>, measured by ERD, as compared with the hole concentration obtained from Hall measurement). This doping efficiency value is much higher than that of conventional continuous wave RF PECVD deposited p-type  $\mu$ c-Si, which is only in the order of 1 % [3]. We speculate that in the Layer-by-Layer material, there is hardly any segregation of dopant atoms from the crystallites to the grain boundaries.
- 6. The properties for the high-temperature deposited doped layers (see *Table 6-1*) show good device quality.

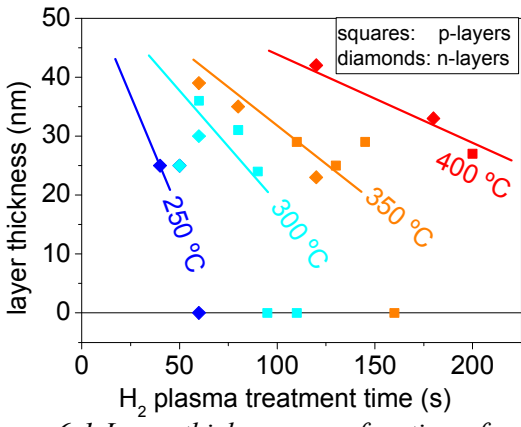


Figure 6-1 Layer thickness as a function of hydrogen treatment time. ( $H_2$  etching rate is decreasing with temperature).

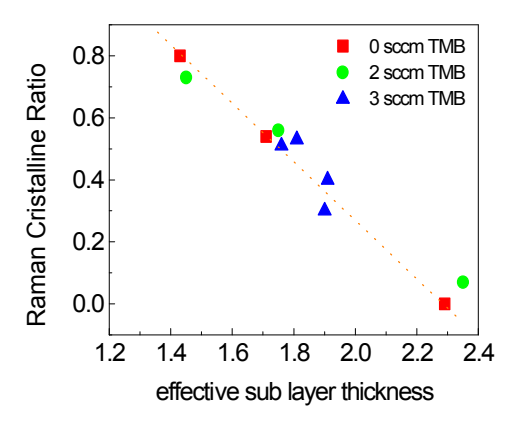


Figure 6-2 Crystalline content of the LBL p-type microcrystalline silicon film at different TMB flows. (Effective sub-layer thickness is defined as the layer thickness divided by the number of cycles.)

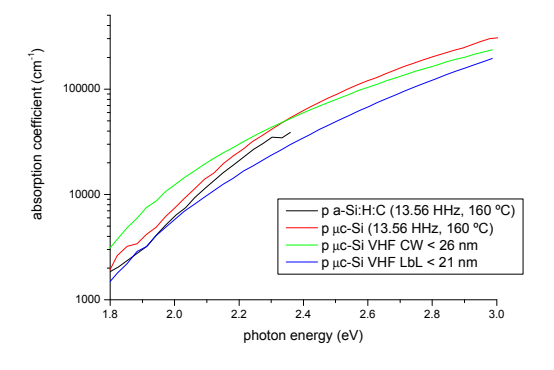


Figure 6-3 Optical absorption of thin doped p-type layers used as window layers in solar cells.

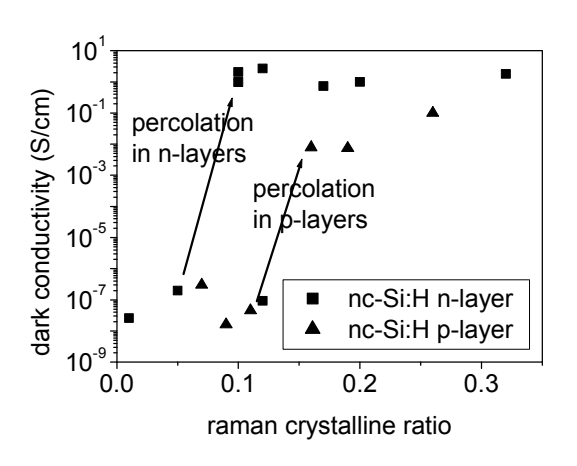


Figure 6-4: Percolation limit in LbL grown

[3].J.K. Rath and R.E.I. Schropp, Solar Energy Materials and Solar Cells 33 (1998) 189-203. n-layers

Table 6-1: properties of the high temperature grown LBL mc-Si doped layers.

type	р	n
$T_s$ (°C)	350	400
d (nm)	29	31
Raman R <sub>c</sub>	0.26	0.12
$E_a$ (eV)	0.11	0.056
$\sigma_{\rm d}  (\Omega^{\text{-1}} { m cm}^{\text{-1}})$	0.1	2.7
$\mu$ (cm <sup>2</sup> /Vs)	0.13	0.35
carrier con. (c	$cm^{-3}$ ) 1.2 × 10 <sup>19</sup>	$1.0 \times 10^{20}$

A number of measurement and analysis concepts has been developed in connection with the LbL depositions, which not only allows for the improvement of the LbL technique but also contributes considerably to the Ph.D. work of Aad Gordijn (junior researcher in this project). The new concepts are listed below.

- 1. For LbL deposition, the processes during the hydrogen plasma treatment that are responsible for the crystallization, change with temperature. The etching rate, for example, decreases with temperature (see Figure 1). At 400 °C, the etching rate is close to 0 but still crystallization takes place.
- 2. The thickness and quality of the first sub-layer in the LbL process has appeared to be one of the most important parameters, especially for deposition at high temperatures. Under certain hydrogen treatment conditions, the first sublayer does not sustain the etching effect and is thus removed completely. In case this first sub layer does not sustain the first hydrogen treatment step, then all subsequent sub layers can be considered as the first sub layer and will disappear as well. This problem is overcome by doubling the growth time of the first growth cycle. By changing the thickness of the first sub layer, the first sub layer itself and consequently all subsequent sub layers sustain the hydrogen treatment cycle. In *Figure 6-5*, it is shown that with a thicker initial sub layer, microcrystalline silicon layers can be made at a substrate temperature of 350 °C with longer hydrogen treatment times and therefore with higher crystalline fractions.
- 3. The kinetics of hydrogen reactions on the growing film have been evaluated using Mass Ion Spectroscopy (Hyden EQP 300). Within the H<sub>2</sub> plasma treatment time, two separate phases can be distinguished. In the initial phases (the first 50 seconds of hydrogen exposure), hydrogen incorporation into the film takes place. The subsequent phase of the hydrogen treatment is predominantly etching. Both hydrogen incorporation and etching processes are exponential functions of time. Whereas the etching rate has a maximum at a temperature between 200-250 °C, abstraction shows a monotonic increase with increasing temperature. Though a full deposition model has not been worked out yet, the above result guides the optimization of the hydrogen treatment process for attaining high crystallinity at various temperatures.
- 4. There is a substantial difference in the surface texture between CW and LbL grown microcrystalline layers. Cross-sectional transmission electron microscopy images show that the CW layers have a significant surface roughness, whereas the LBL layers have a rather smooth surface. This has an advantage for the subsequent growth of i-layers (for making a solar cell), especially when columnar poly-Si is grown. The smooth surface will lead to soft coalescence of the grain columns. The low temperature LbL films have no amorphous incubation phase, however, the high temperature grown films do show some incubation phase. However, this phase is not completely amorphous (a mixed phase) in nature and thus may not have any serious consequences, such as creating interface barriers.

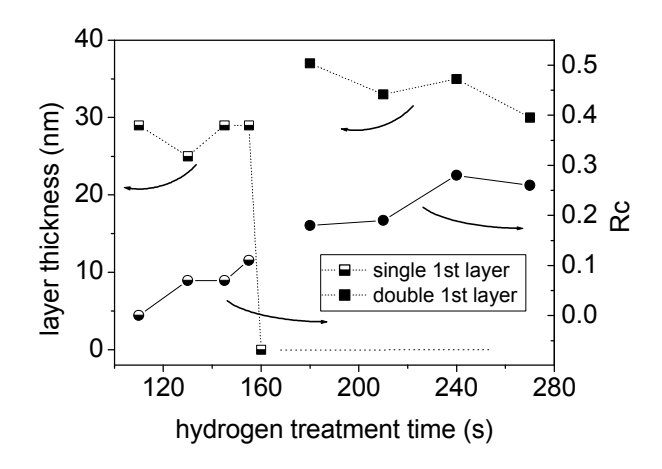
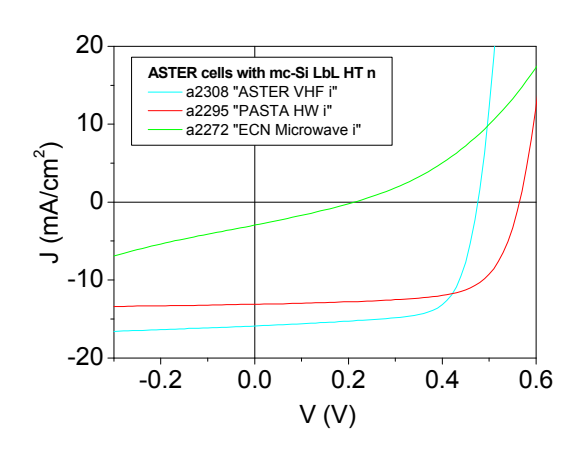


Figure 6-5: improvement in stability of the first sub-layer

# 6.3 Applications in Solar cells

Solar cells have been made to prove the suitability of the high temperature grown doped layers. The structure is as follows: SS/LBL n-layer/VHF or HW i-layer (250 °C)/CW p-layer/ITO/Ag grid (all Si layers are micro-crystalline). For the VHF i-layer, the  $V_{oc}$  of the cell is 0.48 V (which is a high value considering the high crystallinity of the i-layer) and the fill factor is 70 %. These values show that the high temperature doped n-layer have a high doping efficiency. The efficiency of 5.6 % is a moderate value that is mainly due to the low Jsc of 16.78 mA/cm2 (layer thickness is only ~1000nm). It has the potential to be 40 % higher in the presence of efficient light trapping by means of a back reflector. For the HW i-layer, the efficiency is 5.1 % without back reflector. The Voc is 0.564 V and the fill factor is 68 %. The  $J_{sc}$  for this cell is 13.1 mA/cm2. These values demonstrate that the high temperature n-layer maintains its good properties when exposed to the atomic hydrogen rich deposition of a HWCVD  $\mu$ c-Si i-layer.

I-V results of a cell in the same configuration as *Figure 6-7*, but employing microcrystalline ilayer made by MWCVD at ECN is also shown in *Figure 6-6*. It has to be noted that after the n-layer was made at UU by LBL method, the sample was sent to ECN for the i-layer deposition. The rest of the layers were again made at UU. So the air breaks between n-μc-Si layer(UU) and i-μc-Si layer(ECN) and between i-μc-Si layer(ECN) and p-μc-Si layer(UU) have to be taken into account. However, it has to be also noted that the reference cell with VHF PECVD i-μc-Si layer was also made with air breaks between n- and i-layer and between i- and p-layer to simulate the situation. This infers that the air breaks do not have any significant effect. (At least, that is true for the VHF grown i-layer).



1TO contact
20 nm p-type nc-Si:H

1000 nm i-type mc-Si:H

50 nm n-type nc-Si:H

SS substrate

Figure 6-6: Solar cells made with the HT LbL n-layer

Figure 6-7: Cell configuration

# 6.4 Characterization: Collaboration with partners

# 6.4.1 PDS

We performed PDS measurements (*Figure 6-8*) on microwave PECVD grown  $\mu$ c-Si i-layers (developed at ECN) in order to optimize the process for minimal defect density

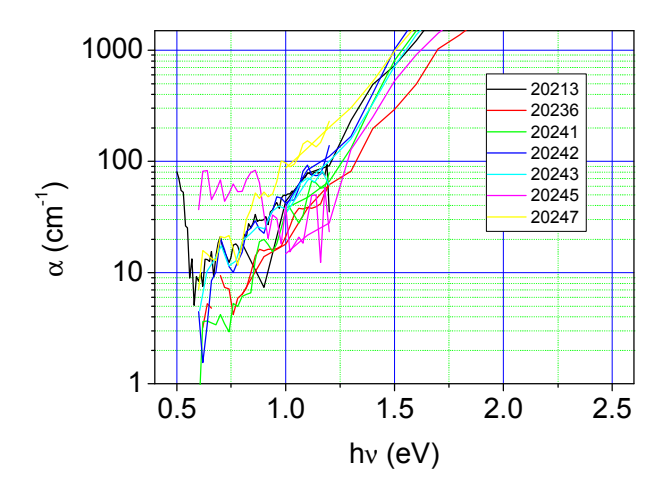


Figure 6-8: PDS spectra of MWPECVD grown mc-Si i-layers from ECN.

# 6.4.2 Raman spectroscopy

A number of µc-Si samples from ECN have been characterized by Raman Spectroscopy (*Figure 6-9*) and analyzed at UU. The results have been published at IEEE and MRS conferences. A number of samples from UU have also been analyzed at TAC.

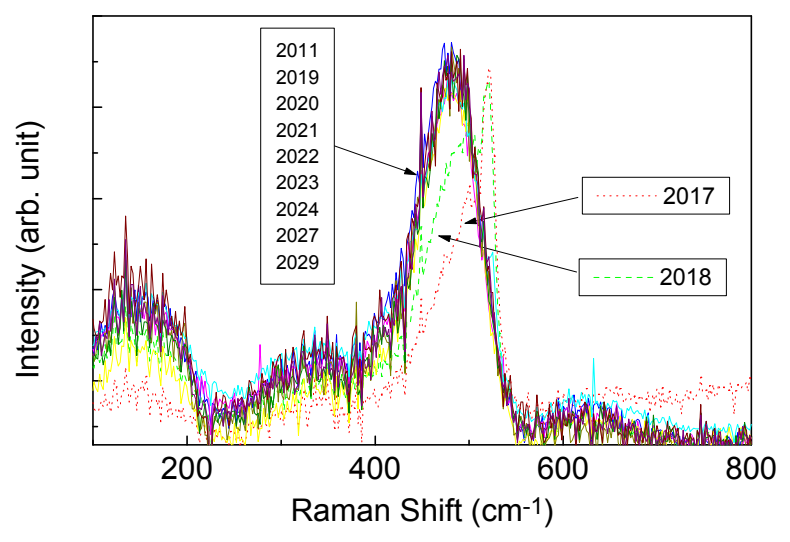


Figure 6-9: Raman spectra of MWPECVD samples made at ECN

#### New calculation method:

The different project partners have chosen to use a simple model for the interpretation of Raman spectra: the ratio of the contributions to the spectrum of the different phases is taken as a characteristic property that quantifies the crystallinity. The fitting procedures to determine these distributions used in Utrecht and Delft is different; however, the two methods are providing almost similar output. In Utrecht, as a first step the complete amorphous contribution is fitted in the range < 480 cm<sup>-1</sup> with 3 Gaussians: the LA peak at 330 cm<sup>-1</sup>, the LO peak at 440 cm<sup>-1</sup> and the TO peak at 480 cm<sup>-1</sup>. The mentioned range is chosen such that no crystalline features are included. Subsequently, this amorphous contribution is subtracted from the original full spectrum, after which a flat spectrum remains in the low energy region, apart from the crystalline contribution around 510 and 520 cm<sup>-1</sup> in the high-energy region. These remaining peaks are fitted with two Gaussians, representing the contributions from different crystallite sizes Due to this two-step fit method, the crystalline contribution is well defined, even at low crystalline ratios. The correlation of the obtained crystalline ratios between Utrecht and Delft (determined on the basis of a broad range of sample deposited and measured at the different places) show a one to one correlation with little noise (*Figure 6-10*).

#### 6.4.3 Electrical conductivity

UU provided reference standard samples and regular consultations to ECN on electrical conductivity and activation energy measurement. The exchange of ideas between ECN and UU on this matter took place regularly.

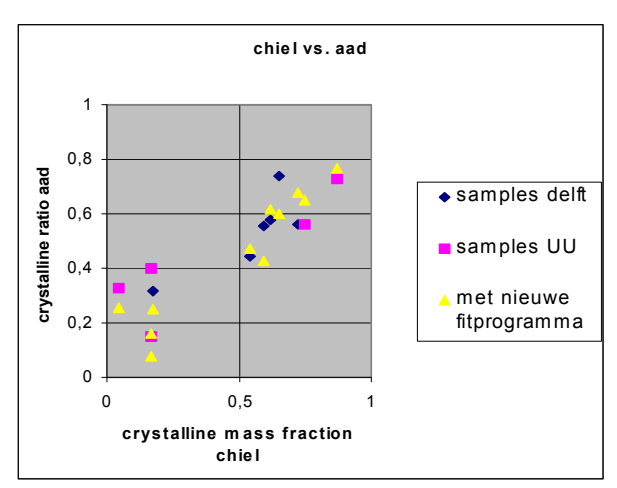


Figure 6-10: Comparison between the crystalline ratios obtained from Raman spectra analyzed by the two methods proposed by Chiel Smith (TU Delft) and Aad Gordijn (UU).

#### 6.4.4 Optical properties

A new experimental method and measurement of the thickness and the optical absorption coefficient (from reflection/transmission measurements) of very thin samples (~10nm) have been developed. This was presented at the aSiNet workshop at Lisbon, May 2003.

# 6.5 Characterization of cells

Only cells grown internally have been analyzed. Characterizations of cells from ECN, TUD and their comparison to cells from UU could not take place, due to the lack of significantly high values for the efficiencies.

### 6.6 Comparison of ETP and MWPECVD cells with reference cells and advice:

Advice in the context of poly-Si deposition and solar cell fabrication (based on our extensive experience on HWCVD poly-Si development) has been given regularly, both informally as well as during formal meetings.

# 6.7 Published/presented articled related to this projects:

- 1. Microcrystalline Silicon Growth in the Presence of Dopants: Effect of High Growth Temperatures. A. Gordijn, J.K. Rath and R.E.I. Schropp, ICAMS20, Campos do Jordao, Brazil (2003), J. Non-Cryst, Solids (in print).
- 2. High Temperature n- and p-type Doped Microcrystalline Silicon Layers Grown by VHF PECVD Layer-by-Layer Deposition, A. Gordijn, J.K. Rath, and R.E.I. Schropp, Mat. Res. Soc. Symp. Proc. Vol. 762 (2003) A6.8.1.
- 3. High temperature thin p- and n doped μc-Si layers deposited with continuous wave and Layer by Layer PECVD at VHF, A. Gordijn, J.K. Rath and R.E.I. Schropp, aSiNet workshop, Lisbon (Feb 2003).
- 4. Interpretation of optical characterization of thin (10 nm) amorphous and microcrystalline (doped) layers, A. Gordijn, J. Löffler, J.K. Rath and R.E.I. Schropp, aSiNet workshop, Lisbon (Feb 2003).
- 5. Nanocrystalline Silicon p and n doped thin layers deposited by Layer-by-Layer PECVD deposition. A. Gordijn, J.K. Rath, and R.E.I. Schropp, FOM Dagen 2002, Veldhoven.
- 6. Mechanism of hydrogen interaction to the growing silicon film, Jatindra K. Rath, Lennaert Klerk, Aad Gordijn, and Ruud E. I. Schropp, 14th PVSEC, Bangkok, January 2004 (accepted oral presentation).

# 7. CONCLUSIONS

The projects Miracle and MissionN have been very ambitious in their targets. Main aims of the projects were:

- 1) definition of criteria for 'device quality' µc-Si,
- 2) evaluation of alternative deposition technologies with respect to their potential for high rate, industrial scale deposition of µc-Si: ETP and MWPECVD,
- 3) creation of a national forum for Dutch R&D on µc-Si solar cells,
- 4) development of 'Layer by Layer' method for deposition of P- and B-doped µc-Si layers,
- 5) development of new, advanced characterization techniques for µc-Si layers,
- 6) insight in growth mechanisms of µc-Si layers,
- 7) fabrication of single junction  $\mu$ c-Si solar cells with efficiencies larger than 8 %.

Critical evaluation of the results obtained during the projects infers that the majority of the targets have been achieved but that for some of the targets the project partners have been too optimistic.

We may conclude that we have succeeded in:

- consensus on criteria for 'device quality' of μc-Si. This consensus was achieved already in the very first phase of the project, and is practically identical to Table 3.2 in the book of Schropp and Zeman<sup>1</sup>.
- development of 'Layer by Layer' method for deposition of doped  $\mu$ c-Si layers. See Chapter 6.
- development of new, advanced characterization techniques for  $\mu$ c-Si layers. See Chapters 3 and 5.
- gaining insight into the growth mechanisms of  $\mu$ c-Si layers. It has to be noted, though, that the interaction between the fundamental research on this subject and the practical research on solar cells has not been optimal, mainly because of phase differences between the two elements of the projects.
- extensive exchange of experience and knowledge between partners. Beyond the regular progress meetings, there has been frequent informal consultation of students and technicians involved in the project, by which a vast amount of practical experience has been exchanged. This resulted e.g. in a new standard for interpretation of Raman spectra of μc-Si (a paper on this subject by C. Smit et al. has been accepted by J. Appl. Phys.), and to a method to determine the thickness of very thin layers (~10 nm) combining an optical model and reflection/transmission measurements.

# And we conclude that we have not succeeded in:

- obtaining μc-Si layers with full device quality, by using ETP or MWPECVD. Main bottleneck here was the porosity of the layers grown by these methods. The porosity results in a fast post-oxidation that in its turn hinders a number of characterization methods to establish the electronic quality. Optical absorption measurements, which are not hindered by post-oxidation show that the defect density of layers grown by MWPECVD is reasonably well, with values below 10<sup>-17</sup> cm<sup>-3</sup>. The weak electronic quality of the μc-Si layers grown by ETP and MWPECVD so far caused that some other aims of the projects could not be achieved as well:
- evaluation of alternative deposition technologies: ETP and MWPECVD with respect to employability for (industrial) fabrication of μc-Si solar cells. Since for both methods we have not been able to deposit μc-Si layers with the desired quality, such an evaluation could not been carried out yet. Owners of the deposition systems (TU/e & Dimes, and

ECN-C--04-009 65

\_

<sup>[1].</sup> R.E.I. Schropp and M. Zeman, Amorphous and Microcrystalline Silicon Solar Cells, Kluwer, Boston, 1998.

- ECN), however, are still convinced of the potential of their respective systems and will therefore continue their research on  $\mu$ c-Si solar cells with these systems.
- fabrication of μc-Si solar cells with efficiencies of 8 %. Since the realization of intrinsic μc-Si layers with certain electronic quality took more time than planned, fabrication of cells started in a late stage of the project. The defect density of the intrinsic layers grown by both ETP and MWPECVD, however, remained too high to obtain good cell efficiencies. We fabricated cells with an efficiency of 1.9 %, with an i-layer grown by ETP at 0.2 nm/s, and with an efficiency of 0.5 % with an i-layer grown by MWPECVD at 0.9 nm/s. The efficiencies of cells fabricated with i-layers deposited by MWPECVD severely suffered from vacuum-interruption since the doped layers of the cells had to be deposited at other locations. Reference cells, fabricated in Utrecht have efficiencies of 5.6 % (VHF deposition at 0.1 nm/s) and 5.1 % (HW deposition at 0.4 nm/s). The reference cells are made on stainless steel as substrate, and are not equipped with a back reflector. Applying a back reflector would enhance the efficiency of these cells to approximately 8 % and more.

The overall conclusion is that - despite the fact that some important aims were not achieved - the projects MissionN and Miracle have been very fruitful and inspiring for all partners. Since we are confident about the potential of both the  $\mu$ c-Si cell concepts and the deposition methods investigated in these projects we will pursuit in continuation of the research carried out in these projects.

# APPENDIX A

# DEPOSITION OF HYDROGENATED MICROCRYSTALLINE SILICON AT GROWTH RATES IN EXCESS OF 1 NM/S USING THE EXPANDING THERMAL PLASMA TECHNIQUE

I.J. Houston, E.A.G. Hamers<sup>†</sup>, W.M.M. Kessels, and M.C.M. van de Sanden

Department of Applied Physics, Eindhoven University of Technology, P.O. Box 513, 5600 MB

Eindhoven, The Netherlands

#### **Abstract**

Hydrogenated microcrystalline silicon films have been deposited using the expanding thermal plasma (ETP) technique at growth rates in excess of 1 nm/s and at substrate temperatures as low as 200 °C. From Raman spectroscopy, X-ray diffraction analysis, and transmission electron microscopy, the conditions necessary for the deposition of microcrystalline silicon have been systematically identified by varying the dilution ratio  $R = [H_2]/[SiH_4]$  from 20 to 200 and the substrate temperature from 200 °C to 450 °C. The investigations show that silicon thin films with a crystalline character ranging from amorphous to nearly polycrystalline can be deposited by the ETP technique at growth rates of up to 2.9 nm/s. The atomic composition of the films has been studied by infrared transmission spectroscopy and the combination of elastic recoil detection and Rutherford backscattering. The hydrogen concentration of the films is discussed in detail.

Keywords: Microcrystalline silicon, plasma deposition, high-rate deposition

#### 1. Introduction

The demand for clean energy sources has resulted in much interest in the deposition of hydrogenated amorphous and microcrystalline silicon for use in thin film solar cells. Hydrogenated amorphous silicon (a-Si:H) based thin film solar cells take advantage of the high absorption coefficient for sunlight offered by a-Si:H as a direct band gap material. The thickness of the a-Si:H can hence be as thin as ~400 nm in single-junction solar cells. However, light-induced defect creation in a-Si:H reduces the efficiency of the solar cells considerably. It is for this reason that hydrogenated microcrystalline silicon ( $\mu$ c-Si:H) has recently emerged as a promising material for use in thin film solar cells as it does not suffer from this light-induced degradation. Furthermore, the combination of a-Si:H and  $\mu$ c-Si:H in multi-junction solar cells offers the possibility of more efficient usage of the solar spectrum and results in increased energy conversion efficiency of the cells.

One consideration when using  $\mu$ c-Si:H is that the material has a lower absorption coefficient in the visible region of the spectrum than a-Si:H. This means that much thicker layers (typically 2-4  $\mu$ m) are required for the incorporation of the  $\mu$ c-Si:H into solar cells. Hence a key element in improving the competitiveness of silicon thin film based solar cells is whether it is possible to deposit material with suitable properties at very high growth rates (preferably >1 nm/s).

However, most techniques used in the deposition of  $\mu$ c-Si:H report growth rates of less than 1 nm/s. The conventional radio frequency plasma enhanced chemical vapour deposition (rf-

<sup>&</sup>lt;sup>†</sup> Current address: AKZO-NOBEL Central Research, P.O. Box 9300, 6800 SB Arnhem, The Netherlands

PECVD) method typically results in deposition rates of 0.01 - 0.1 nm/s [1,2]. Similarly, the electron cyclotron resonance chemical vapour deposition technique (ECR-CVD) has been used to achieve deposition rates of 0.3 nm/s [3] and the hot wire chemical vapour deposition (HWCVD) technique typically yields growth rates ranging from 0.1 nm/s to 1 nm/s [1.4.5.6.7] although deposition rates as high as 5 nm/s have recently been reported [8]. The fact that most commonly used techniques produce growth rates of less than 1 nm/s has initiated the exploration of novel techniques which are capable of achieving much higher growth rates and the diversity of the methods that have been explored is a reflection of the significance which is attached to obtaining high quality uc-Si:H at (very) high growth rates. For example, Kondo et al. have adapted their PECVD setup into a triode configuration and have employed very high frequencies (VHF, 60 MHz) to achieve very high growth rates of ~5 nm/s for μc-Si:H [9]. Revolutionary new methods to deposit uc-Si:H at very high growth rates have also been explored by Franz et al. [10] and Chae et al. [11]. Using a dc plasma CVD reactor, in which a non-thermal plasma column is maintained between a tungsten filament cathode and copper anode, Franz et al. were able to obtain growth rates of up to 10 nm/s for uc-Si:H although this was at short distances from the plasma column where it is known that the substrate temperature rises considerably (up to 450 °C) [10]. Chae et al. have achieved ultra-fast growth rates of 1000 nm/s through their thermal plasma chemical vapour deposition (TPCVD) method using a hybrid plasma torch operated on both dc and rf power. By employing this method, which is already a well-established technique for the deposition of non-electronic materials (hard diamond coatings, ceramics, etc.), uc-Si:H films have been obtained with a reasonably low defect density [11].

One further method which has been employed in the deposition of silicon-based thin films at high growth rates is the expanding thermal plasma (ETP). The ETP technique has been used to deposit silicon nitride films at rates as high as 20 nm/s for use as bulk passivating antireflection coatings on crystalline silicon solar cells [12,13] and the ETP technique has recently become an established technique as regards the high rate deposition (10 nm/s) of a-Si:H for thin film solar cells [14]. The fact that good (electronic) material properties can be obtained at very high growth rates with the ETP technique is a result of the combination of effective plasma creation at subatmospheric pressure in a plasma source and the dissociation of the precursor gases by mono-radical reactions in a low-pressure reactor. In this article the ETP technique is investigated as a method of depositing  $\mu$ c-Si:H at very high growth rates [15,16] and the conditions for the deposition of µc-Si:H are identified. In order to extend this technique from the deposition of a-Si:H to the deposition of  $\mu$ c-Si:H high dilutions of SiH<sub>4</sub> in H<sub>2</sub> are employed. In addition to this the substrate temperature is varied in order to investigate whether this can be used to improve the quality of the resultant material. The ratios of hydrogen and silane (SiH<sub>4</sub>) which are used to produce microcrystalline silicon using the ETP technique are between 20 and 200 times higher than those used to deposit amorphous silicon. The crystalline character of the resultant films is investigated using Raman spectroscopy, X-ray diffraction (XRD) and transmission electron microscopy (TEM). Fourier transform infrared (FTIR) spectroscopy and the nuclear profiling techniques of Rutherford backscattering (RBS) and elastic recoil detection (ERD) are used to investigate the atomic composition of the resultant films. The results of these techniques will be used to show the potential for the deposition of µc-Si:H at growth rates of >1 nm/s using the ETP technique.

#### 2. Experimental

The ETP technique, schematically illustrated in Fig. 1, is a remote plasma assisted deposition technique in which a thermal Ar- $H_2$  plasma is created in a dc arc discharge operating at subatmospheric pressure (approximately 40 kPa). This Ar- $H_2$  plasma expands into a reactor chamber pumped by a set of roots blowers yielding a pressure of ~20 Pa in the reactor. The argon flow is 55 sccs (standard cm<sup>3</sup>s<sup>-1</sup>) and the  $H_2$  flow can be varied from 0 to 30 sccs. Si $H_4$  is admixed by means of an injection ring at a distance of 6 cm from the arc exit at a flow of up to 10 sccs. No power is coupled into the downstream region leading to a low electron temperature (typically 0.2 eV) in the expansion region. As a consequence of this, when  $H_2$  is admixed to the

arc it essentially acts as an efficient atomic hydrogen source particularly when the  $H_2$  flow is 30 sccs as is used to deposit  $\mu$ c-Si:H [17,18]. Therefore the admixed SiH<sub>4</sub> is mainly dissociated by this atomic hydrogen and dissociation caused by ions and electrons is virtually negligible. At reasonably low  $H_2$  to SiH<sub>4</sub> ratios, such as those used for the deposition of a-Si:H, this leads predominantly to SiH<sub>3</sub> radicals due to the abstraction of H from SiH<sub>4</sub> by atomic hydrogen [19]. When the SiH<sub>4</sub> is heavily diluted, as is the case for the deposition of  $\mu$ c-Si:H, this reaction may be followed by other reactions which also produce significant fractions of other silane radicals [20].

The films are deposited on substrates clamped onto a substrate holder  $(10\times10 \text{ cm}^2)$  which is positioned at a distance of 35 cm from the plasma source. The temperature of the substrate holder, which can hold several small-sized substrates at a time, is actively controlled by Ohmic heating and a helium back flow is used to improve the thermal contact between substrate holder and substrates [12]. The setup is also equipped with an automatic shutter and a loadlock chamber which prevents the reactor being exposed to the air each time the substrates need to be changed. The base pressure in the reactor is  $10^{-4}$  Pa when pumped by the 450 l/s turbo pump.

A rigorous approach has been used to identify and optimise the conditions for the deposition of μc-Si:H films. A series of films was deposited in which deposition parameters, the dilution ratio and substrate temperature, were varied. All samples were deposited using a H<sub>2</sub> flow of 30 sccs and an Ar flow of 55 sccs. Initially a constant substrate temperature of 250 °C was used and the SiH<sub>4</sub> flow was altered from 1.4 sccs to 0.15 sccs. This means that the dilution ratio *R* of H<sub>2</sub> flow to SiH<sub>4</sub> flow (=[H<sub>2</sub>]/[SiH<sub>4</sub>]) was varied from approximately 20 to 200. The substrate temperature was then varied from 200 °C to 450 °C, while maintaining a constant *R* value of 60. All deposition conditions are summarised in Table 1. All films were 1000 nm thick unless otherwise stated. For each deposition a set of 3 samples with a size of 2.5×2.5 cm<sup>2</sup> were deposited. The films were deposited on crystalline silicon (c-Si) and Corning 7059 glass substrates. These substrates were cleaned prior to deposition but no extra treatment was performed on the c-Si to remove the native surface oxide.

Analysis was conducted on all c-Si samples using Fourier transform infrared transmission spectroscopy (FTIR) to determine the growth rate as well as the hydrogen content. These results were obtained using a Bruker Vector 22 Fourier Transform Spectroscope and the infrared spectra are measured from  $\omega = 370 \text{ cm}^{-1}$  to  $7500 \text{ cm}^{-1}$  with a resolution of 4 cm<sup>-1</sup>. The film thickness was determined from the interference fringes of the resulting background spectrum in the non-absorbing spectrum ranges, as described elsewhere [21]. The hydrogen content is determined by integrating the 640 cm<sup>-1</sup> Si-H absorption peak and applying the calibration factor  $(1.6\times10^{19} \text{ cm}^{-2})$  as determined for a-Si:H deposited by the ETP and other techniques [22]. The hydrogen content  $C_H$  of the films is defined as  $C_H = N_H/N_{tot}$  where  $N_H$  is the hydrogen atomic density and  $N_{tot}$  is the total film density. It is assumed that  $N_{tot} = 5\times10^{22} \text{ cm}^{-3}$  [22].

The results obtained by FTIR in this study were compared with results from elastic recoil detection (ERD) and Rutherford backscattering (RBS) measurements on 300 nm thick films which provide information regarding the atomic density of elements within the samples [23,24]. In FTIR transmission spectroscopy only hydrogen atoms which are bonded to Si atoms are detected. The FTIR method is therefore insensitive to  $H_2$ , unlike ERD which measures all of the hydrogen atoms in the film. Some ERD/RBS measurements were conducted at the Philips CFT Materials Analysis Lab using 2 MeV  $^4$ He $^+$  ions although more extensive investigations were carried out at Utrecht University using 54 MeV  $^{65}$ Cu $^{8+}$  ions. The higher energy of the  $^{65}$ Cu $^{8+}$  ions as compared to the  $^4$ He $^+$  ions allows the measurement of a wider range of elements by ERD within the sample. The absolute density scale in the measurements is obtained by assuming a total atomic density of  $5\times10^{22}$  cm $^{-3}$  for a standard ( $H_2=10$ , R=1) a-Si:H sample [22]. The atomic densities for the other films have been scaled to this density. As hydrogen in the films can easily desorb from the film during ion dosing the hydrogen yield was also monitored as a function of the ion dose. Extrapolation then provides the yield at zero ion dose. FTIR has shown that oxidation is heavily time-dependent in  $\mu$ c-Si:H and for this reason the ERD and ERD/RBS measurements were deliberately carried out less than 1 day after deposition in order

to limit the impact of any post-deposition oxidation. Hence the data cannot be considered a quantitative indication of oxygen content in the long term.

The crystalline nature of the samples was investigated using Raman spectroscopy and X-ray diffraction (XRD) measurements. The degree of crystallinity within a given sample is measured by means of Raman spectroscopy and the crystallite size is found using XRD [25]. These parameters were used to quantify the effect of the variation in deposition conditions on the amorphous/microcrystalline character of the material.

The Raman measurements were performed at the Delft University of Technology using a home-built setup. This setup consists of a continuous Nd:YVO<sub>4</sub> laser (Spectra Physics Millenia), the output of which is frequency doubled to 532 nm and reduced to a power of 2 mW. The spectra were measured in a  $180^{\circ}$  backscatter geometry. The collected Raman signal is separated from the signal caused by Rayleigh scattering and focussed on a optical fiber connected to a monochromator. The monochromator (Spex 340E) is equipped with a 1800 grooves/mm grating blazed at 500 nm, and a liquid nitrogen cooled CCD camera (LN/CCD-1100PB, Princeton Instruments). The crystalline content was estimated from the measurements through comparison of the results with those from a-Si:H samples. A Raman spectrum is first obtained from an a-Si:H reference sample. This spectrum is then subtracted from the spectrum of a  $\mu$ c-Si:H sample to leave only the crystalline contribution. The relative strengths of the amorphous and microcrystalline contributions are then compared to produce a value for the crystalline fraction. A full description of this method can be found elsewhere [26].

The crystallite size within the  $\mu$ c-Si:H films was determined through XRD measurements on 1000 nm thick films deposited on c-Si. These measurements used a Bruker-Nonius theta-theta diffractometer with a diffracted-beam graphite monochromator. Cu-K $_{\alpha}$  radiation with a wavelength of 0.154 nm was used in the analysis. The XRD results were analysed by first subtracting the background obtained from a blank c-Si substrate. A resulting diffractogram of a  $\mu$ c-Si:H film is given in Fig. 2. The diffractogram shows four peaks and the three main peaks at approximately 28.4°, 47.3° and 56.1° correspond to the (111), (220) and (311) crystal orientations which are present within  $\mu$ c-Si:H [25]. The first peak, at approximately 27°, is known as the "first scattering peak" (FSP) and derives from the amorphous fraction within the material. This peak may be significantly influenced by the medium range order of the amorphous fraction and becomes more pronounced with increasing structural ordering of the material [25]. The full-width-half-maximum (FWHM) of each of the three crystalline peaks was used to estimate the crystallite size for each orientation while the FWHM of the FSP was used to determine the so-called correlation length (L) within the amorphous material. These parameters were determined using the Scherrer equation [27]

$$L = \frac{0.9\lambda}{W\cos\theta}.$$
 (1)

Where W is the FWHM of the peak in radians,  $\theta$  is the peak position and  $\lambda$  is the wavelength of the X-ray radiation employed. The preferential growth direction, which is the direction in which the crystallites within the  $\mu$ c-Si:H are predominantly oriented, can be determined by comparing the relative intensity of the peaks after correcting for finite thickness. This method and the correction which is applied to the peak area is described by Birkholz *et al.* [28,29] and takes the form:

$$I = \frac{A}{1 - \exp(-\frac{2\mu d}{\sin \theta})}.$$
 (2)

Where A is the integrated area of the diffraction peak, d is the thickness of the sample and  $m = 148 \text{ cm}^{-1}$  accounts for the X-ray absorption coefficient of Si under Cu-K<sub>\alpha</sub> radiation. The ratios of these corrected intensities of the different diffraction peaks provide information regarding the preferential growth direction. In randomly orientated silicon powder the intensity ratio is found to be  $I_{111}$ : $I_{220}$ : $I_{311} = 1:0.55:0.30$  [4]. A clearer way of presenting results is to derive percentages from these ratios. This should not be regarded as representing percentage fractions within the material, but rather as a more readily understandable way of presenting the calculated ratios. By

considering each crystalline orientation as a fraction of the whole we find that the expected fractions of the (111), (220) and (311) crystalline orientations for a randomly orientated sample as described above are 54.1 %, 29.7 % and 16.2 %, respectively.

The crystallinity and the crystallite morphology of the microcrystalline silicon deposited in the course of this study were also investigated by transmission electron microscopy (TEM). This was carried out at the Philips CFT Materials Analysis lab in Eindhoven using a FEI/Philips Tecnai F30ST Transmission Electron Microscope operated at 300 kV. Cross-sectional samples were prepared using mechanical tripod polishing. Dark field images of a 250 nm thick µc-Si:H film were produced and a high resolution image was used to examine the lower 30 nm.

#### 3. Results

#### 3.1 Influence of the dilution ratio R on microcrystallinity

The  $SiH_4$  dilution ratio R has been shown to be an important parameter in the deposition of  $\mu$ c-Si:H. For this reason a number of samples were deposited using different dilution ratios and analysed using the abovementioned techniques to determine the deposition rate and investigate the crystalline nature of the material.

The deposition rate has been determined using thicknesses obtained from the interference fringes in the FTIR spectra in conjunction with the deposition time. The deposition rate of the samples obtained for different R values is given in Fig. 3 and varies from 1 to 7 nm/s. It is apparent that the deposition rate is higher at lower R values. In fact, the deposition rate increases linearly with the SiH<sub>4</sub> flow. It is however clear that very high growth rates (> 1 nm/s) are obtained at all of the R values which were used.

In order to determine whether the samples are amorphous or microcrystalline, the crystalline nature of the films was investigated by means of Raman spectroscopy and XRD. Figures 4 and 5 show the results from these experiments and the transition from amorphous to microcrystalline material as the dilution ratio R increases can be clearly seen. The crystalline peaks from Raman spectroscopy and XRD increase in intensity with increasing dilution ratio R, indicating an increase in the crystallinity of the films. In the Raman spectra, a peak emerges at 520 cm<sup>-1</sup> for values of  $R \ge 60$ . This is consistent with the XRD results which show a first indication of crystallinity at R = 60.

The Raman spectroscopy results were used to calculate the crystallite fraction within the material and the results are given in Table 2. This again illustrates that depositions using  $R \ge 60$  result in  $\mu$ c-Si:H material. This sharp transition from amorphous to microcrystalline silicon is consistent with other studies of  $\mu$ c-Si:H films [30,31]. For each of the XRD diffraction peaks in Fig. 5 the FWHM was also calculated to estimate the crystallite size using Eq. 1. The analysis of these peaks indicates that the average crystallite size varies from ~4 to 20 nm (Table 2) which is broadly consistent with the values reported in literature [11,25,32,33]. Table 2 also reveals that the correlation length calculated from the FSP increases as the material becomes more crystalline. This indicates that the medium range order of the amorphous material in the  $\mu$ c-Si:H films also increases. The crystallite size increases with increasing crystallite fraction and the largest crystallite sizes are obtained for the grains with (111) orientation.

In Table 2, percentage values are given which are representative of the proportion of material which is found in each crystalline orientation. For the films deposited at R = 60 and R = 100, the percentage values indicate that the crystallites in these films have grown preferentially in the (220) and (311) directions. However, as the crystalline fraction increases these values approach those for random orientation.

# 3.2 Influence of substrate temperature on microcrystallinity

Although very high growth rates (10 nm/s) have previously been achieved for the deposition of a-Si:H using the ETP technique it was necessary to use relatively high substrate temperatures (>350 °C) to obtain solar grade quality material [14]. As the substrate temperature may have a comparable influence on the properties of the  $\mu$ c-Si:H films deposited at very high growth rates, the influence of the substrate temperature on the crystallinity of the films has been considered

and a range of samples were deposited using substrate temperatures from 200 to 450  $^{\circ}$ C and a constant dilution ratio of R = 60.

The FTIR results showed that the substrate temperature has no significant influence on the deposition rate which remained constant at  $\sim$ 2.9 nm/s for all substrate temperatures. Raman spectroscopy revealed that the substrate temperature also has no significant effect on the crystalline content of the deposited material as shown in Table 3. The crystalline content of approximately 58 % is comparable with the value for the R = 60 film deposited in the dilution series as discussed in Sec. 3.1. As shown in Table 3, the correlation length increases with substrate temperature and this indicates a greater degree of order within the amorphous fraction at high substrate temperatures. The values related to the crystalline orientations show that the preference for (220) orientation decreases slightly as the substrate temperature is increased. This is accompanied by a small increase in the number of crystallites in the (111) orientation. The results obtained by varying the substrate temperature show that this has almost no effect on the crystalline content of the films. However, an increase in substrate temperature does result in increased ordering of the amorphous fraction. Elevated substrate temperatures also mean that the crystalline orientation of the film approaches that expected for sample containing randomly orientated crystallites.

# 3.3 Atomic composition of the films

The atomic composition of the a-Si:H and µc-Si:H films produced in this investigation has been examined in order that conclusions can be drawn regarding the value of the films for future applications. In particular the hydrogen concentration in the material is of interest as it can have a significant influence on the material structure and its properties. For these reasons the hydrogen content of the deposited films was analysed by FTIR transmission spectroscopy and the results were compared with those from the combination of ERD/RBS measurements. The latter also provide valuable information regarding the atomic density of the different types of atoms present within the material.

From the FTIR measurements, the hydrogen content is determined from the integrated area of the absorption peak at  $\sim$ 640 cm<sup>-1</sup> which is due to the SiH<sub>x</sub> wagging modes. Figure 6 shows that the hydrogen content determined by this method decreases with increasing R such that the µc-Si:H films have a lower H concentration than the a-Si:H films. The ERD results show a consistently higher value of the hydrogen concentration than FTIR. This difference is in marked contrast to previous results from a-Si:H samples, deposited with R = 1, in which no significant discrepancy between FTIR and ERD is apparent [22]. This is illustrated in Fig. 6 by showing results from a standard a-Si:H sample (deposited using an  $H_2$  flow of 10 sccs and R = 1) which was analysed at the same time as the other samples deposited during the course of this investigation. In this case the FTIR value is actually slightly higher then the value obtained through ERD, appearing to preclude any possibility that an inherent systematic difference exists between the two techniques. Furthermore, the ERD result for the sample deposited at R = 200obtained with the 54 MeV <sup>65</sup>Cu<sup>8+</sup> beam has been checked by an independent measurement using the 2 MeV <sup>4</sup>He<sup>+</sup> beam. Although Fig. 6 shows some difference between the two results (performed on two different samples), the ERD results consistently yield a considerably higher hydrogen concentration than that determined with FTIR.

One possible reason for the discrepancy between the FTIR and ERD results could be that the calibration constant used in the FTIR analysis is not valid for the films studied in this work. The trend within the two sets of results is almost identical and a higher value of the calibration constant could account for the difference between FTIR and ERD. The results of Kroll *et al.* [34] also show that ERD results produce consistently higher values than FTIR results. Despite this, Kroll *et al.* have shown that the calibration constants for a-Si:H are also valid for  $\mu$ c-Si:H films except for a narrow transition region from amorphous to microcrystalline material. In fact, the difference between the ERD and FTIR results was ascribed to the presence of unbonded hydrogen in the material as ERD, unlike FTIR, is sensitive to both bonded and unbonded hydrogen. The data presented in Fig. 6 are certainly not all within a transition region and therefore we do not expect that the invalidity of the calibration constants alone can account for the discrepancy. For this reason, the difference between the FTIR and ERD results obtained

from films deposited using the ETP technique can be (partly) attributed to the presence of molecular hydrogen, H<sub>2</sub>, in the films presented in Fig. 6. Therefore we conclude that the ERD measurements suggest the presence of a considerable amount of molecular hydrogen in the μc-Si:H films. More evidence for this is also found through closer examination of the ERD results. It is well known that hydrogen in silicon films can easily desorb from the film under the heavy ion irradiation used in the ERD measurements. For this reason, the ERD analysis with the energetic 54 MeV <sup>65</sup>Cu<sup>8+</sup> beam in particular is always performed as a function of the ion dose. For the films in Fig. 6, the effect of hydrogen desorption was particularly strong which may be a further indication of the presence of molecular hydrogen within the films and even the analysis with the 2 MeV <sup>4</sup>He<sup>+</sup> ion beam showed a clear variation in hydrogen yield as a function of ion dose despite its relatively low ion irradiation. This is illustrated in Fig. 7. The hydrogen concentration in these ERD measurements is therefore estimated from the extrapolation of the hydrogen yield to zero ion dose.

The presence of a relatively large amount of  $H_2$  in the  $\mu$ c-Si:H films is probably not beneficial for the material properties of the  $\mu$ c-Si:H when used in solar cell devices. Furthermore, the a-Si:H films deposited with  $R \ge 21$  contain a considerable amount of molecular hydrogen whereas for the a-Si:H films deposited under the standard conditions for the ETP setup (*i.e.*, R = 1) there is no evidence for the presence of molecular hydrogen in the film. Therefore the a-Si:H films deposited under standard conditions are probably denser than the a-Si:H films deposited with  $R \ge 21$ . The latter also have a higher hydrogen concentration than the film deposited with R = 1. Both ERD and FTIR show that the hydrogen content decreases with increasing crystallinity. This has also been observed for  $\mu$ c-Si:H films deposited with other techniques [5,34] and the total H concentration for the films deposited with the ETP is similar to that found in such material.

Information about the atomic density of the different atoms in the films has also been obtained with ERD using the 54 MeV 65Cu<sup>8+\*</sup> ion beam and the results are given in Fig. 8. The absolute number of the atomic densities is estimated by assuming a total atomic density of 5×10<sup>22</sup> cm<sup>-3</sup> for a-Si:H deposited under standard conditions. Figure 8 also shows the atomic densities for a uc-Si:H film deposited with R = 200 which were obtained by the combination of ERD and RBS using the 2 MeV <sup>4</sup>He<sup>+</sup> ion beam. This measurement has yielded absolute values and the reasonable agreement between data points of the two methods for R = 200 appears to justify the abovementioned assumption regarding the density of the samples. Figure 8 shows therefore that the silicon atomic density in the films decreases as the R value, and hence the crystalline fraction, increases and the films become more microcrystalline. After this initial decrease the silicon atomic density appears to stabilise at approximately R = 60, the point at which a significant crystalline fraction is present within the film. This is indicative of an increase in film porosity as the films become microcrystalline. The films also contain some oxygen and, although the oxygen concentration appears to remain constant as the films become more microcrystalline, no definite conclusions regarding the oxygen content can be drawn as the oxidation of the uc-Si:H is time dependent as mentioned earlier in Sec. 2. The ERD and ERD/RBS measurements also show that a small amount of carbon is present in the films. The precise origin of this carbon is still unknown but one plausible explanation is that carbon is etched from the SiH<sub>4</sub> injection ring as a result of the very large H<sub>2</sub> flows (i.e., 30 sccs) employed in these depositions. No carbon contamination is usually observed when hydrogen flows of 10 sccs are employed. This issue will be addressed in future investigations.

ERD and FTIR measurements were also carried out to assess the influence of substrate temperature as the use of high substrate temperatures has previously been employed to decrease the hydrogen content and increase the silicon atomic density in a-Si:H films [22,35]. This has been found to be particularly important for a-Si:H films deposited at high growth rates for which solar grade film properties could only be obtained at substrate temperatures of over 350 °C [14,35]. The hydrogen content obtained by the FTIR and ERD analysis is given in Fig. 9 as a function of the substrate temperature and the data show the same discrepancy as was observed when *R* was varied (Fig. 6). Nevertheless, the trends in the data are similar as the FTIR data reveal a decreasing H concentration with increasing substrate temperature. The ERD data show

the same trend although at very high substrate temperatures ( $400\,^{\circ}$ C) the hydrogen content does appear to have increased slightly. However, this increase may be within the experimental error of this measurement and it is possible that no definitive conclusion can be drawn on the basis of this increase.

The results for atomic density obtained from ERD are given in Fig. 10 and show a slight increase in silicon atomic density with increasing substrate temperature. Although the effect is small (<5 % for silicon atomic density), this indicates that the density of the material can be increased through the use of elevated substrate temperatures. The oxygen atomic density in the film shows almost no dependence on substrate temperature.

These ERD and FTIR results imply that substrate temperature could be used to reduce the hydrogen content of the material without significantly influencing the microcrystalline character. This could also have the advantage of slightly increasing the silicon density. Even a relatively small increase in substrate temperature from 250 °C to 300 °C could have a significant beneficial influence on the hydrogen content.

#### 3.4 Transmission electron microscopy

Transmission electron microscopy (TEM) measurements have been performed on a 250 nm thick film deposited on a Si (100) substrate covered with native oxide using a dilution ratio R = 200 and a substrate temperature of 250 °C. Raman and XRD measurements (see Table 2) have shown that these conditions should result in a large crystalline content and Fig. 11 clearly shows the microcrystalline nature of this material as determined by TEM measurements. The cross-section of the substrate is relatively thick and not electron transparent and hence appears dark in the TEM images. In the dark field image [Fig. 11(a)] crystallites are clearly visible and the columnar morphology of the material is evident. The periodic contrast variation is caused by twinning or stacking faults within the crystallites. Columns of 15-20 nm width are found as well as some of 30-50 nm. This is broadly consistent with values for crystallite size found using XRD (Table 2) as well as those for column widths reported in literature [29,33]. The almost polycrystalline character of the film is in agreement with the high crystalline fraction revealed by the Raman measurements in Table 2.

Figure 11(b) shows a high resolution image which shows a smaller area in the lower 30 nm of the  $\mu$ c-Si:H film in greater detail. This image shows the crystalline orientations of the individual lattice fringes and reveals that the film is already microcrystalline at the interface with the substrate. This shows that, under these conditions, no significant amorphous interface layer has been formed during the deposition.

#### 4. Discussion

The results presented here show that it is possible to deposit microcrystalline silicon with growth rates as high as 2.9 nm/s. Comparison with existing results, especially those obtained using novel high rate techniques, shows that the properties of the material deposited in the course of this investigation are consistent with those previously found for microcrystalline silicon. For example, the magnitude of the grain size within the material is comparable with that found in previous investigations using both standard and very high rate deposition techniques [3,11,25,32,33] and the most crystalline material exhibits the columnar structure which is generally observed for microcrystalline silicon.

Comparison with results from other novel techniques which are capable of very high deposition rates [9-11] are of particular relevance to this investigation. It should be noted that the material's predisposition towards the (220) crystalline orientation for most conditions is in line with the results of both Franz *et al.* [10] and Chae *et al.* [11]. Although Chae *et al.* found much greater grain sizes this could possibly be ascribed to the incorporation into the material of clusters which are formed in the gas phase. A sharp transition from amorphous to microcrystalline material has been observed for the ETP material and this is also seen by Kondo *et al.* [9]. Both Franz *et al.* [10] and Chae *et al.* [11] show that no 2000 cm<sup>-1</sup> peak is present in the FTIR absorption spectra obtained for their µc-Si:H silicon material and Franz *et al.* also found a shoulder on the 640 cm<sup>-1</sup> peak in the same material. Both of these effects were also observed for µc-Si:H deposited using the ETP technique. It is clear from these comparisons that

the ETP technique is capable of depositing  $\mu$ c-Si:H which has structural properties comparable to those obtained using other techniques.

The results obtained in this study are of significant importance when considering the optimal conditions, i.e. substrate temperature and dilution ratio, for the deposition of microcrystalline silicon for use in solar cells. The substrate temperature has been known to significantly increase the grain size within microcrystalline silicon [36,37,38] as well as the crystalline content [3,36,37] but it has been found that the substrate temperature has no significant effect on the crystalline fraction within the material deposited using the ETP technique. However, it has been shown that elevated substrate temperatures reduce the hydrogen content of the films and this is of particular interest as substrate temperature has been shown to have no detrimental effect on deposition rate. Nevertheless, it should be considered that it is desirable to minimise the substrate temperature during the deposition of solar cells. The use of lower substrate temperatures reduces the economic cost of the deposition process and allows for a wider choice regarding the substrate material and manufacturing process used in the deposition of the cell. With this in mind, it is clear from Fig. 9 that a relatively small increase in substrate temperature from 250 to 300 °C would provide for a significant decrease in hydrogen content. Increases of a similar magnitude beyond this point do not provide the same degree of improvement. This minor increase in substrate temperature would also result in an increase in silicon atomic density as shown in Fig. 10.

Increasing the dilution ratio leads to an increase in crystalline content and a decrease in growth rate. These two effects must be balanced to achieve the optimum growth conditions. For solar cell applications high crystalline contents are not usually required. Silicon films deposited close to the transition between amorphous and microcrystalline material are often more suitable [8,39]. The ETP technique is capable of depositing  $\mu$ c-Si:H which is almost polycrystalline at growth rates of > 1 nm/s and material close to the amorphous to microcrystalline transition can be deposited at growth rates as high as 2.9 nm/s. These results show that the ETP technique is a promising technique for the very high rate deposition of  $\mu$ c-Si:H and is suitable for the deposition of silicon films with a wide range of material properties.

#### 5. Conclusions

Microcrystalline silicon has been deposited using the ETP technique and the resultant material has been extensively analysed using various techniques to characterise both the structure and the atomic composition. It has been shown that it is possible to use very high growth rates to deposit  $\mu$ c-Si:H films using the ETP technique. Microcrystalline silicon films are obtained by using values for dilution ratios  $R \ge 60$  and Raman spectroscopy has revealed that crystalline fractions greater than 60 % are obtained at growth rates higher than 2 nm/s. In addition to the a-Si:H which has previously been investigated it is clear that the ETP technique is capable of depositing silicon thin films with a wide range of crystalline contents and material properties. It is possible to deposit both  $\mu$ c-Si:H material which is close to the amorphous/microcrystalline transition as well as almost polycrystalline material.

XRD shows that the resultant  $\mu$ c-Si:H material exhibits a preferential crystalline orientation in the (220) direction although the material becomes randomly orientated at high crystalline contents. The results from TEM show the characteristic columnar structure typical of microcrystalline growth and confirm results from Raman which show that material grown at 250 °C with a dilution ratio R=200 is almost polycrystalline. It was found that the substrate temperature had almost no effect on the crystalline content of the  $\mu$ c-Si:H although the crystallites within the  $\mu$ c-Si:H material became more randomly orientated at high substrate temperatures.

The atomic composition of the films has been investigated by FTIR and ERD/RBS and it has been demonstrated that high R values result in a decrease in silicon density and hydrogen concentration. A large discrepancy in hydrogen concentration as obtained by FTIR and ERD has been observed as ERD results produce consistently higher values for hydrogen content than FTIR. This has been attributed to the presence of a significant amount of molecular hydrogen in the films. Although the substrate temperature has been shown to have no significant effect on

crystalline content within the temperature range of 250 - 450 °C it has been shown that the atomic composition is affected by the substrate temperature and the results from FTIR and ERD/RBS suggest that the use of a substrate temperature of 300 °C could slightly increase the silicon density and significantly reduce the hydrogen content.

The results presented here show the potential of the ETP technique for the very high rate deposition of  $\mu$ c-Si:H films and provide a strong foundation for further investigation to elucidate the optoelectronic material properties and the performance of the material in solar cells.

#### Acknowledgements

The authors gratefully acknowledge Dr. Y. Tamminga and T. Dao (Philips CFT Materials Analysis Lab) and Dr. W. Arnoldbik (Utrecht University) for conducting the RBS/ERD measurements, J.G.M. van Berkum (Philips CFT Materials Analysis Lab) for carrying out the TEM analysis, H. Donker and C. Smit (Delft University of Technology) for providing Raman measurements and analysis and N. van der Pers (Delft University of Technology) for conducting XRD measurements. This work has been carried out within the NOVEM "Mission-N" and E.E.T. "Helianthos" programs of the Netherlands Ministry of Economic Affairs, the Ministry of Education, Culture and Science and the Ministry of Public Housing, Physical Planning, and Environment. The research of Dr. W.M.M. Kessels has been made possible by a fellowship of the Royal Netherlands Academy of Arts and Sciences (KNAW). M.J.F. van de Sande, J.F.C. Jansen, A.B.M. Hüsken and H.M.M. de Jonge are thanked for their technical assistance.

#### References

7610076

- [1] P. Alpuim, V. Chu, and J.P. Conde, J. Appl. Phys. 86 (1999) 3812.
- [2] H. Fujiwara, M. Kondo, and A. Matsuda, Phys Rev B. 63 (2001) 115306.
- [3] M. Mars, M. Fathallah, E. Tresso, and S. Ferrero, J. Non-Cryst. Sol. 299-302 (2002) 133.
- [4] S. Yu, S. Deshpande, E. Gulari, and J. Kanicki, Mater. Res. Soc. Symp. Proc. 377 (1995) 69.
- [5] S. Klein, J. Wolff, F. Finger, and R. Carius, Jpn. J. Appl. Phys. 41 (2002) L10.
- [6] D.H. Levi, B.P. Nelson, and J.D. Perkins, Mater. Res. Soc. Symp. Proc. 715 (2002) A25.2.
- [7] S.Klein, F. Finger, R. Carius, H. Wagner, and M. Stutzmann, Thin Solid Films 395 (2001) 305.
- [8] R.E.I. Schropp, Y. Xu, E. Iwaniczko, G.A. Zaharias, and A.H. Mahan, Mat. Res. Soc. Symp. Proc. 715 (2002) A.26.3.
- [9] M. Kondo, S. Suzuki, Y. Nasuno, and A. Matsuda, Mater. Res. Soc. Symp. Proc. 664 (2001) A4.3.1.
- [10] D. Franz, F. Grangeon, T. Delachaux, A.A. Howling, Ch. Hollenstein, and J. Karner, Thin Solid Films 383 (2001) 11.
- [11] Y. K. Chae, H. Ohno, K. Eguchi, and T. Yoshida, J. Appl. Phys. 89 (2001) 8311.
- [12] W.M.M. Kessels, J. Hong, F.J.H. van Assche, J.D. Moschner, T. Lauinger, W.J. Soppe, A.W. Weeber, D. C. Schram, and M.C.M. van de Sanden, J. Vac. Sci. Technol. A 20 (2002) 1704.
- [13] J. Hong, W.M.M. Kessels, F.J.H. van Assche, H.C. Rieffe, W.J. Soppe, A.W. Weeber, and M.C.M. van de Sanden, Prog. Photovolt. Res. Appl. 11 (2003) 125.
- [14] W.M.M. Kessels, R.J. Severens, A.H.M. Smets, B.A. Korevaar, G.J. Adrianssens, D.C. Schram, and M.C.M. van de Sanden, J. Appl. Phys. 89 (2001) 2065.
- [15] E.A.G. Hamers, A.H.M. Smets, C. Smit, J.P.M. Hoefnagels, W.M.M. Kessels, and M.C.M. van de Sanden, Mat. Res. Soc. Symp. Proc. 664 (2001) A.4.2.
- [16] C. Smit, E.A.G. Hamers, B.A. Korevaar, R.A.C.M.M. van Swaaij, and M.C.M. van de Sanden, J. Non-Cryst. Sol. 299-302 (2002) 98.
- [17] W.M.M. Kessels, M.C.M. van de Sanden, and D.C. Schram, J. Vac. Sci. Technol. A 18 (2000) 2153.
- [18] M.C.M. van de Sanden, R.J. Severens, W.M.M. Kessels, R.F.G. Meulenbroeks, and D.C. Schram, J. Appl. Phys. 84 (1998) 2426; J. Appl. Phys. 85 (1999) 1243.

- [19] W.M.M. Kessels, M.G.H. Boogaarts, J.P.M. Hoefnagels, D.C. Schram, and M.C.M. van de Sanden, J. Vac. Sci. Technol. A 19 (2001) 1027.
- [20] W.M.M. Kessels, P.J. van den Oever, J.P.M. Hoefnagels, J. Hong, I.J. Houston, and M.C.M. van de Sanden, Mater. Res. Soc. Symp. Proc. 715 (2002) A.25.6.
- [21] R.J. Severens, G.J.H. Brussard, M.C.M. van de Sanden, and D.C. Schram, Appl. Phys. Lett. 67 (1995) 491.
- [22] W.M.M. Kessels, M.C.M. van de Sanden, R.J. Severens, L.J. van Ijzendoorn, and D.C. Schram, Mater. Res. Soc. Symp. Proc. 507 (1998) 529.
- [23] L.J. van IJzendoorn, Anal. Chem. Act. 297 (1994) 55.
- [24] W.M. Arnoldbik and F.H.P.M. Habraken, Rep. Prog. Phys. 56 (1993) 859.
- [25] D.L. Williamson, Mater. Res. Soc. Symp. Proc. 552 (1999) 259.
- [26] C. Smit, R.A.C.M.M. van Swaaij, H. Donker, A.M.H.N. Petit, W.M.M. Kessels, and M.C.M. van de Sanden, submitted for publication.
- [27] B.E. Warren, X-Ray Diffraction. (Addison-Wesley, Reading MA, 1969).
- [28] M. Birkholz, B. Selle, E. Conrad, K. Lips, and W. Fuhs, J. Appl. Phys. 88 (2000) 4376.
- [29] M. Birkholz, S. Fiechter, A. Hartmann and H. Tributsch, Phys. Rev. B. 43 (1991) 11926.
- [30] F. Finger, S. Klein, A.L. Baia Neto, O. Vettrl, and R. Carius, Mater. Res. Soc. Symp. Proc. 715 (2002) A.16.3.
- [31] A.L. Baia Neto, A.L. Lambertz, R. Carius, and F. Finger, Phys. Stat. Sol. (a) 186 (2001) R4-R6.
- [32] L. Houben, M. Luysberg, P. Hapke, R. Carius, F. Finger, and H. Wagner, Phil. Mag. A. 77 (1998) 1447.
- [33] F. Finger, P. Hapke, M. Luysberg, R. Carius, and H. Wagner, Appl. Phys. Lett. 65 (1994) 20.
- [34] U. Kroll, J. Meier, A. Shah, S. Mikhailov, and J. Weber, J. Appl. Phys. 80 (1996) 4971.
- [35] W.M.M. Kessels, R.J. Severens, M.C.M. van de Sanden, and D.C. Schram, J. Non-Cryst. Sol. 227-230 (1998) 133.
- [36] S. Hamma and P. Rocca I Cabarrocas, J. Non-Cryst. Sol. 227-230 (1998) 852.
- [37] J. Kondo, A. Tabata, T. Kawamura, and T. Mizutani, Vacuum 66 (2002) 409.
- [38] T. Kamei, Mater. Res. Soc. Symp. Proc. 638 (2001) F.13.5.
- [39] J. Koh, Y. Lee, H. Fujiwara, C.R. Wronski, and R.W. Collins, Appl. Phys. Lett. 73 (1998) 1526.

Table 1: The SiH<sub>4</sub> flow, the corresponding dilution ratio  $R = [H_2]/[SiH_4]$  and the substrate temperature for the deposition conditions described in this article. The other fixed parameters are an Ar flow of 55 sccs, a H<sub>2</sub> flow of 30 sccs, a pressure of 19 Pa, and an arc current of 45 A.

SiH <sub>4</sub> flow	$R = [H_2]/[SiH_4]$	Substrate temperature			
(sccs)		(°C)			
1.44	21	250			
0.9	33	250			
0.7	43	250			
0.5	60	250			
0.3	100	250			
0.15	200	250			
0.5	60	200			
0.5	60	250			
0.5	60	300			
0.5	60	350			
0.5	60	400			
0.5	60	450			

Table 2: Results from Raman spectroscopy and XRD analysis for different values of the dilution ratio *R*. The crystalline fraction has been calculated from Raman measurements. The crystallite size and correlation length given for each crystalline orientation have been obtained from XRD measurements. The percentage values for each crystalline orientation do not represent absolute percentage fractions within the material but are derived from the ratios of the intensities of the individual peaks to show how the crystalline orientation varies with deposition conditions.

R	Crystalline	Correlation	Crystallite size			(111)	(220)	(311)
	fraction	length	(nm)			fraction*	fraction*	fraction*
	(%)	(nm)	(111)	(220)	(311)	(%)	(%)	(%)
21	0	1.3	0	0	0	-	-	-
33	0	1.2	0	0	0	-	-	-
43	0	1.4	0	0	0	-	-	-
60	59	3.2	14.0	3.6	4.8	26.2	50.5	23.3
100	70	4.4	15.5	6.2	6.3	44.6	34.4	21.0
200	77	4.9	19.0	12.6	6.8	54.1	27.6	18.4

<sup>\*</sup>Random orientation would result in values of 54.1 %, 29.7 % and 16.2 % for the (111), (220) and (311) directions respectively.

Table 3: Results from Raman spectroscopy and XRD analysis for different substrate temperatures and a dilution ratio R = 60. The crystallite fraction has been calculated from Raman measurements. The crystallite size, correlation length and the percentage values given for each crystalline orientation have been obtained from the XRD measurements (see Table 2).

Substrate	Crystalline	Correlation	Crystallite size		(111)	(220)	(311)	
temperature	fraction	length (nm)	(nm)		fraction*	fraction*	fraction*	
(°C)	(%)		(111)	(220)	(311)	(%)	(%)	(%)
250	58	2.8	13.8	4.9	7.4	33.7	47.1	19.2
300	60	3.4	14.2	5.6	6.2	36.1	39.4	24.5
350	58	7.8	11.6	10.3	7.2	47.6	33.8	18.6
400	56	7.1	12.1	9.5	7.0	49.3	30.5	20.2
450	56	6.1	12.0	6.9	7.0	45.7	33.8	20.5

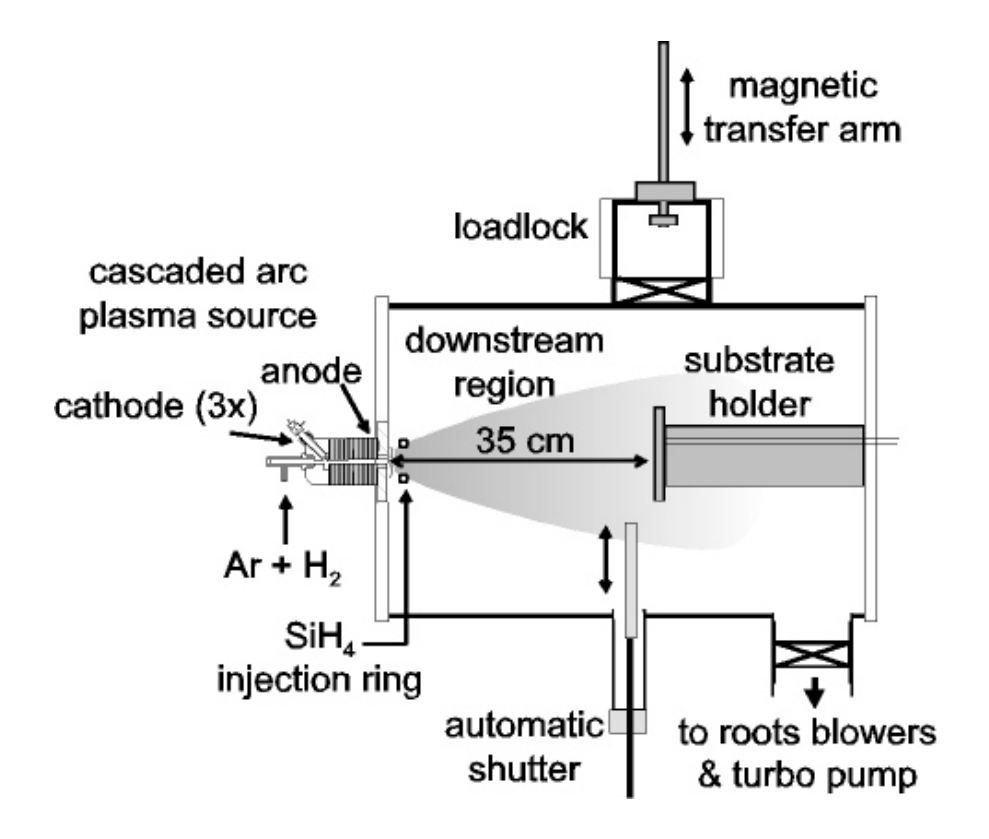
<sup>\*</sup>Random orientation would result in values of 54.1 %, 29.7 % and 16.2 % for the (111), (220) and (311) directions respectively.

#### Figure captions:

- FIG. 1: The expanding thermal plasma (ETP) setup used for fast deposition of hydrogenated amorphous and microcrystalline silicon.
- FIG. 2: Typical XRD spectrum for hydrogenated microcrystalline silicon showing the three peaks corresponding to the (111), (220) and (311) crystalline silicon orientations as well as the first scattering peak (FSP) at approximately 27°.
- FIG. 3: Deposition rate as a function of the ratio R (=[H<sub>2</sub>]/[SiH<sub>4</sub>]) for a substrate temperature of 250 °C. The error bars are derived from the reproducibility of the results.
- FIG. 4: Raman results for different values of the dilution ratio R. The amorphous peak at 480 cm<sup>-1</sup> is visible in all results and a microcrystalline peak at 520 cm<sup>-1</sup> emerges when the dilution ratio R is increased. The substrate temperature is 250 °C.
- FIG. 5: XRD spectra for different values of the dilution ratio R. The crystalline peaks clearly appear when the dilution ratio R is increased. The spectra have been shifted vertically for clarity. The substrate temperature is 250 °C.
- FIG. 6: Elastic recoil detection (ERD) and Fourier transform infrared spectroscopy (FTIR) results giving hydrogen content as a function of dilution ratio *R*. These results are obtained using a hydrogen flow of 30 sccs. Previous results from a-Si:H obtained using a hydrogen flow of 10 sccs are also shown and indicate the typical agreement found between ERD and FTIR measurements. ERD results obtained by a 2 MeV <sup>4</sup>He<sup>+</sup> beam are shown for comparison and are consistent with the results of ERD measurements obtained using a 54 MeV <sup>65</sup>Cu<sup>8+</sup> beam. The error bars shown represent the typical reproducibility of the measurements. The substrate temperature is 250 °C.
- FIG. 7: Elastic recoil detection results showing yield of recoiled H atoms as a function of the measured 2 MeV  ${}^{4}\text{He}^{+}$  ion dose. The film considered has been deposited with a dilution ratio R = 200 and at a substrate temperature of 250 °C. The dotted line is used to determine the yield at zero ion dose.
- FIG. 8: Atomic densities of Si, H, C and O as a function of the dilution ratio R as obtained from elastic recoil detection (ERD) analysis using  $^{65}$ Cu<sup>8+</sup> ions. The absolute number of the atomic densities is estimated by assuming a total atomic density of  $5\times10^{22}$  cm<sup>-3</sup> for the standard a-Si:H material (R=1). A typical error is indicated for R=60 (based upon the reproducibility of the measurement). Results are also included from ERD and Rutherford backscattering (RBS) measurements using  $^{4}$ He<sup>+</sup> ions. These are absolute values derived directly from the experiment.
- FIG. 9: Hydrogen concentration as a function of substrate temperature as obtained from Fourier transform infrared spectroscopy (FTIR) and elastic recoil detection (ERD) analysis. A typical error is indicated for a substrate temperature of 250 °C and is based upon the reproducibility of the measurement. All results were obtained using a dilution ratio *R* of 60.
- FIG. 10: Atomic densities of Si, H, C and O as a function of the substrate temperature as obtained from elastic recoil detection (ERD) analysis using  $^{65}$ Cu<sup>8+</sup> ions. The absolute number of the atomic densities is estimated by assuming a total atomic density of  $5\times10^{22}$  cm<sup>-3</sup> for standard (R=1) a-Si:H material. A typical error is indicated for a substrate temperature of 250 °C and is based upon the reproducibility of the measurement. All results were obtained using a dilution ratio R=60.

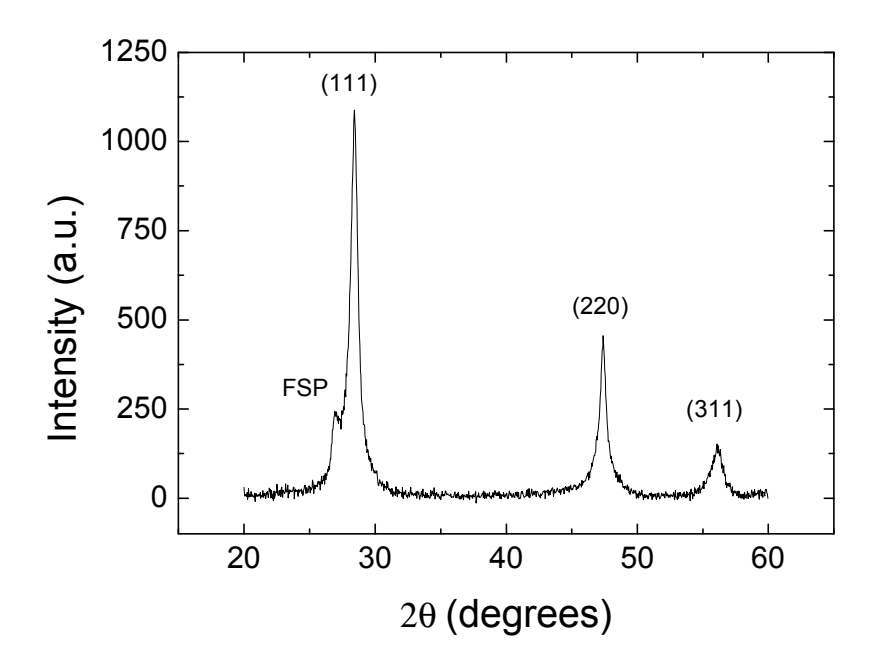
FIG. 11: Cross-section transmission electron microscopy results from a  $\mu$ c-Si:H sample showing (a) a dark field image and (b) a high resolution image. The sample was deposited using a dilution ratio R = 200 and a substrate temperature of 250 ° C.

Figure 1 of 11



I.J. Houston *et al*. Thin Solid Films

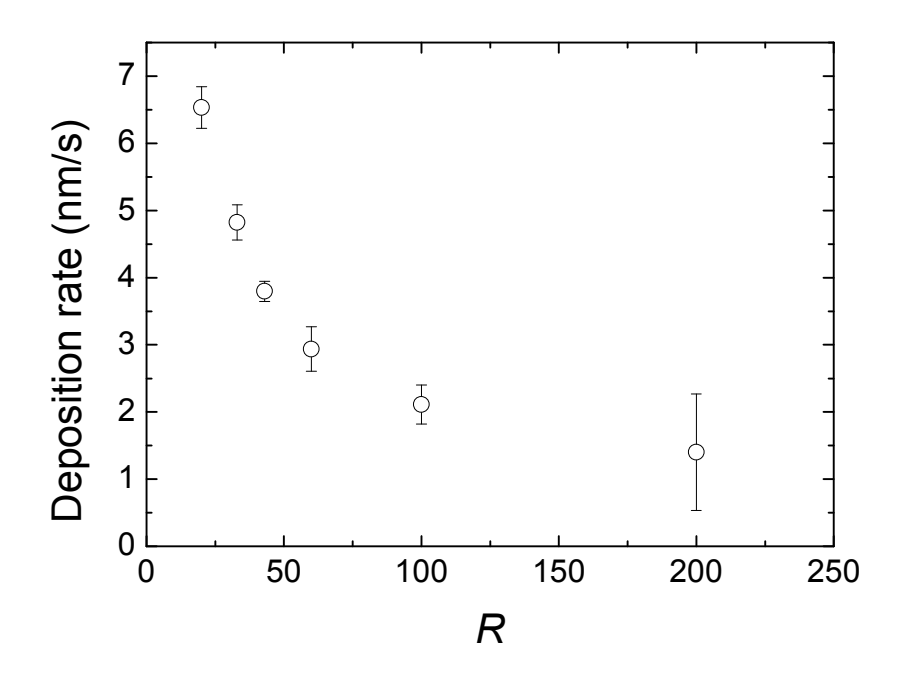
Figure 2 of 11



### I.J. Houston et al.

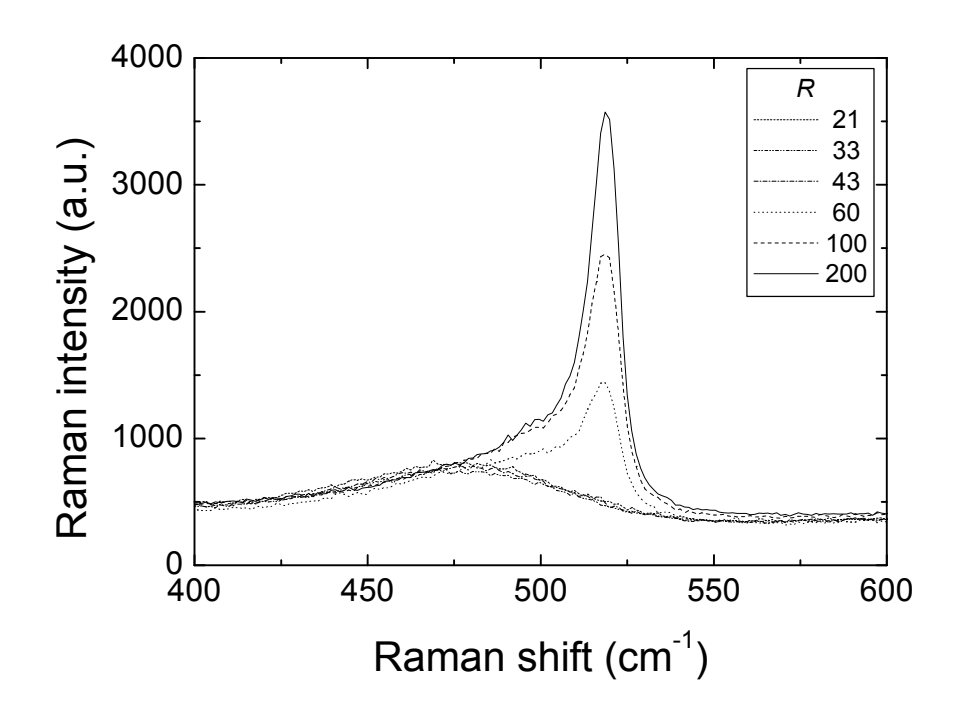
Thin Solid Films

Figure 3 of 11



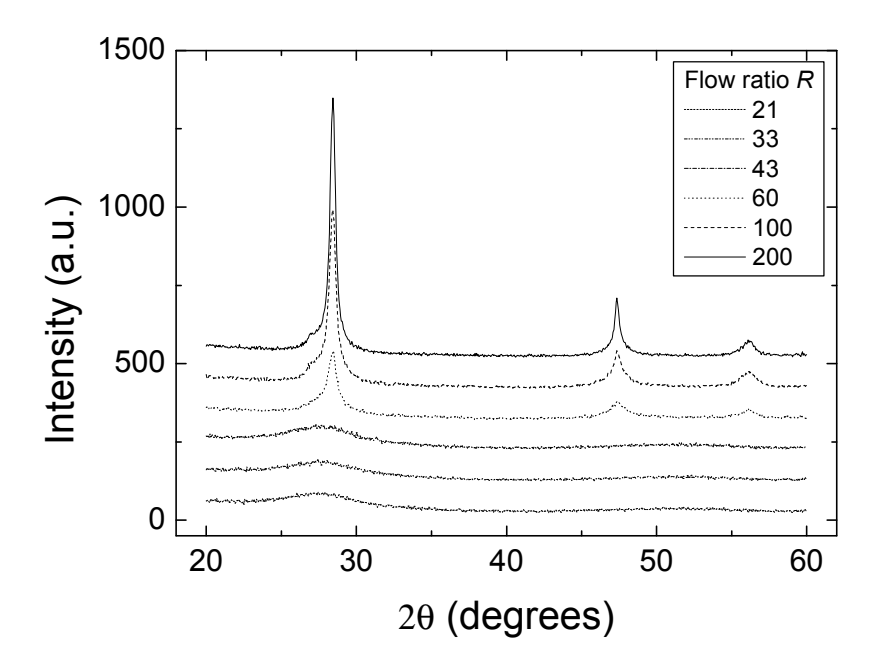
I.J. Houston *et al*. Thin Solid Films

Figure 4 of 11



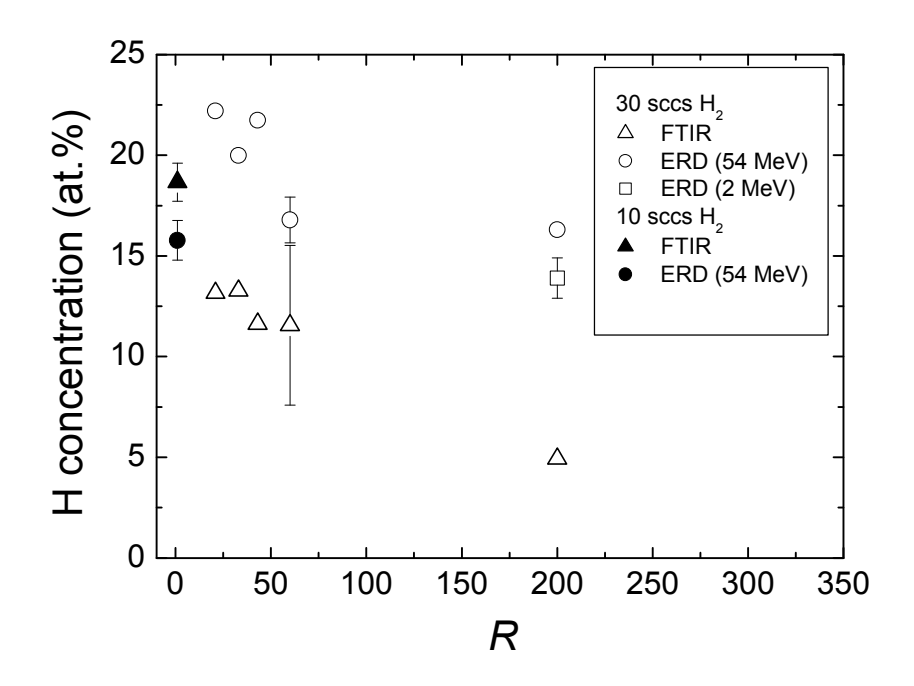
I.J. Houston *et al*. Thin Solid Films

Figure 5 of 11



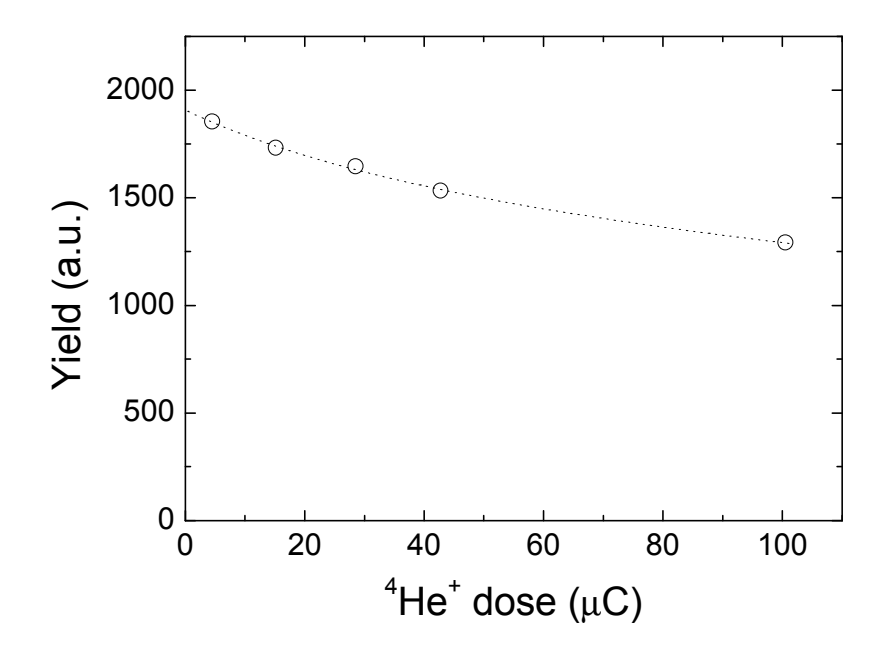
I.J. Houston *et al*. Thin Solid Films

Figure 6 of 11



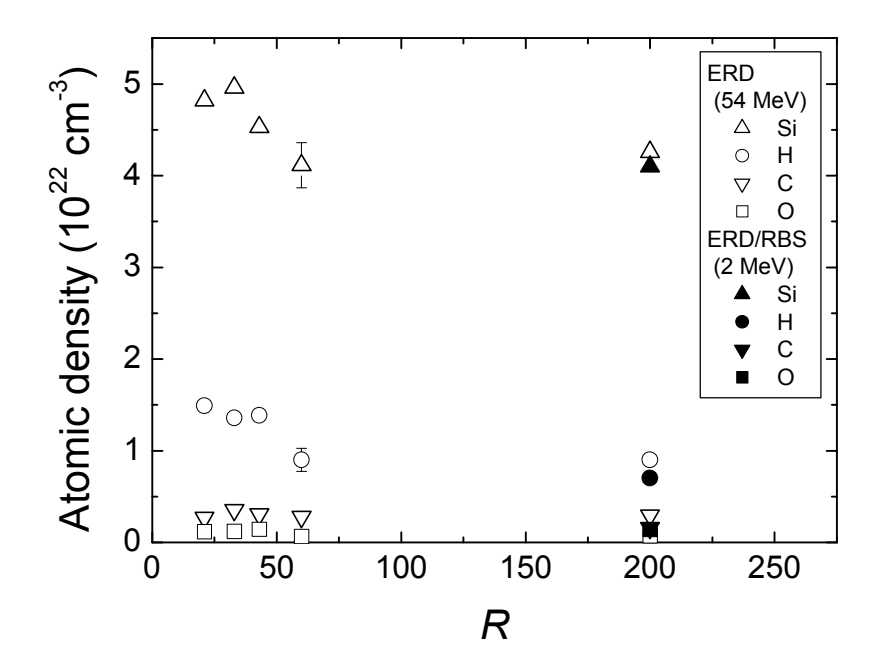
## I.J. Houston *et al*. Thin Solid Films

Figure 7 of 11



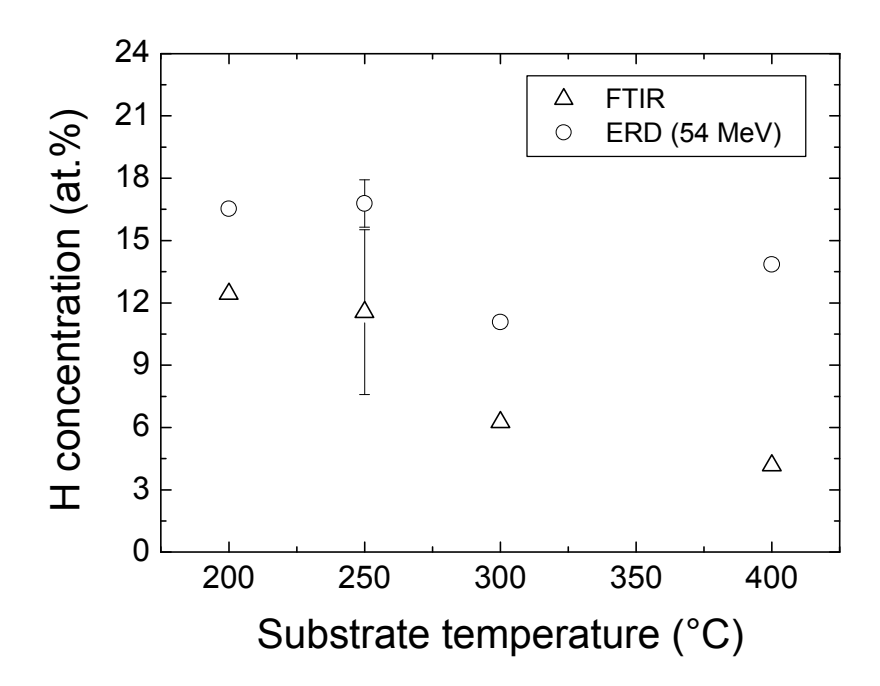
I.J. Houston *et al*. Thin Solid Films

Figure 8 of 11



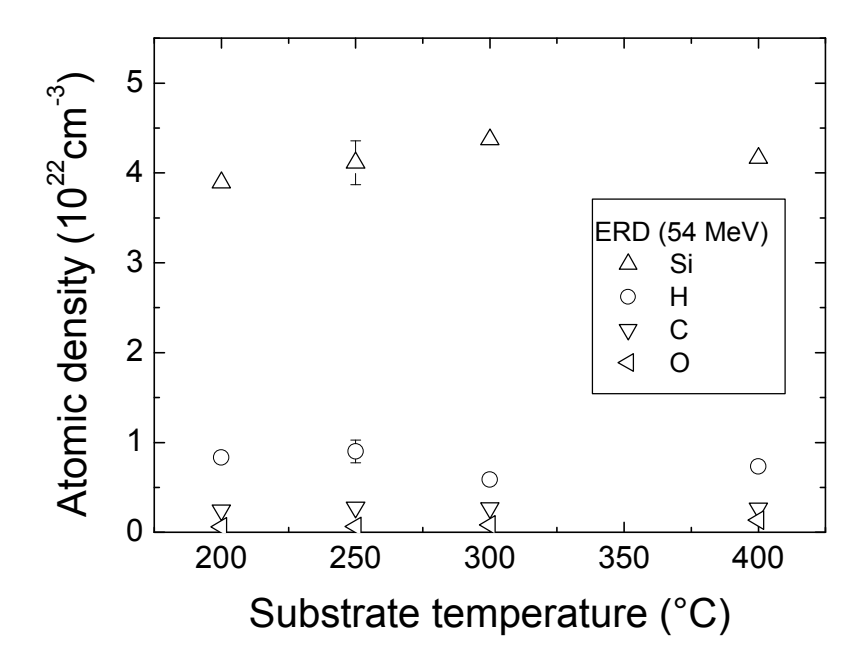
# I.J. Houston *et al.*Thin Solid Films

Figure 9 of 11



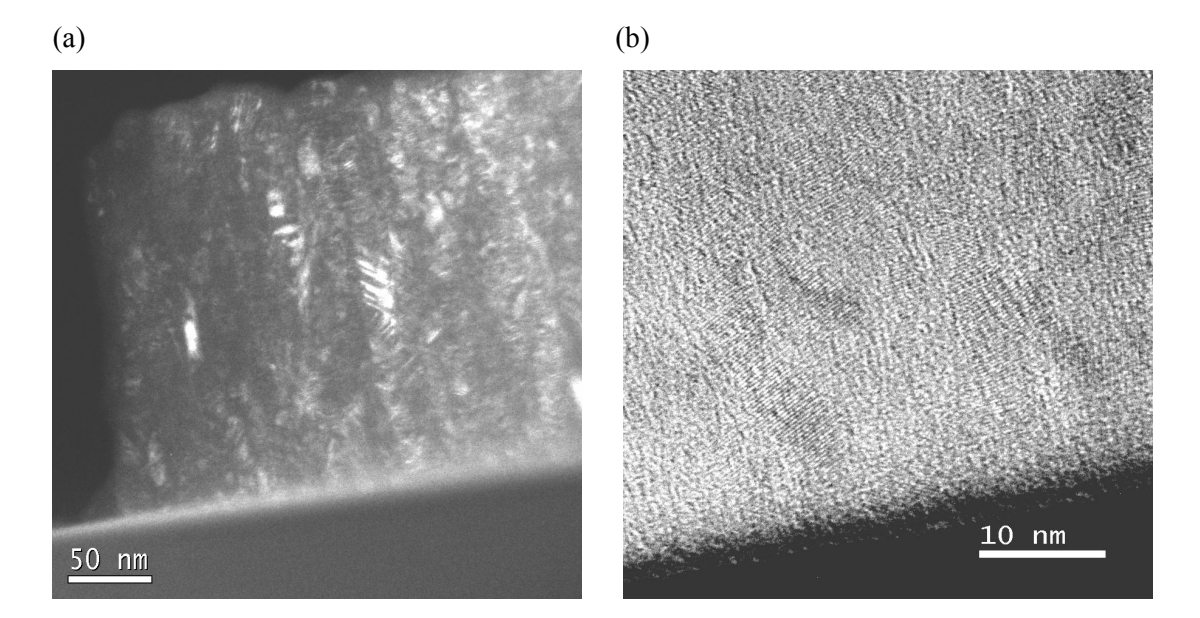
I.J. Houston *et al*. Thin Solid Films

Figure 10 of 11



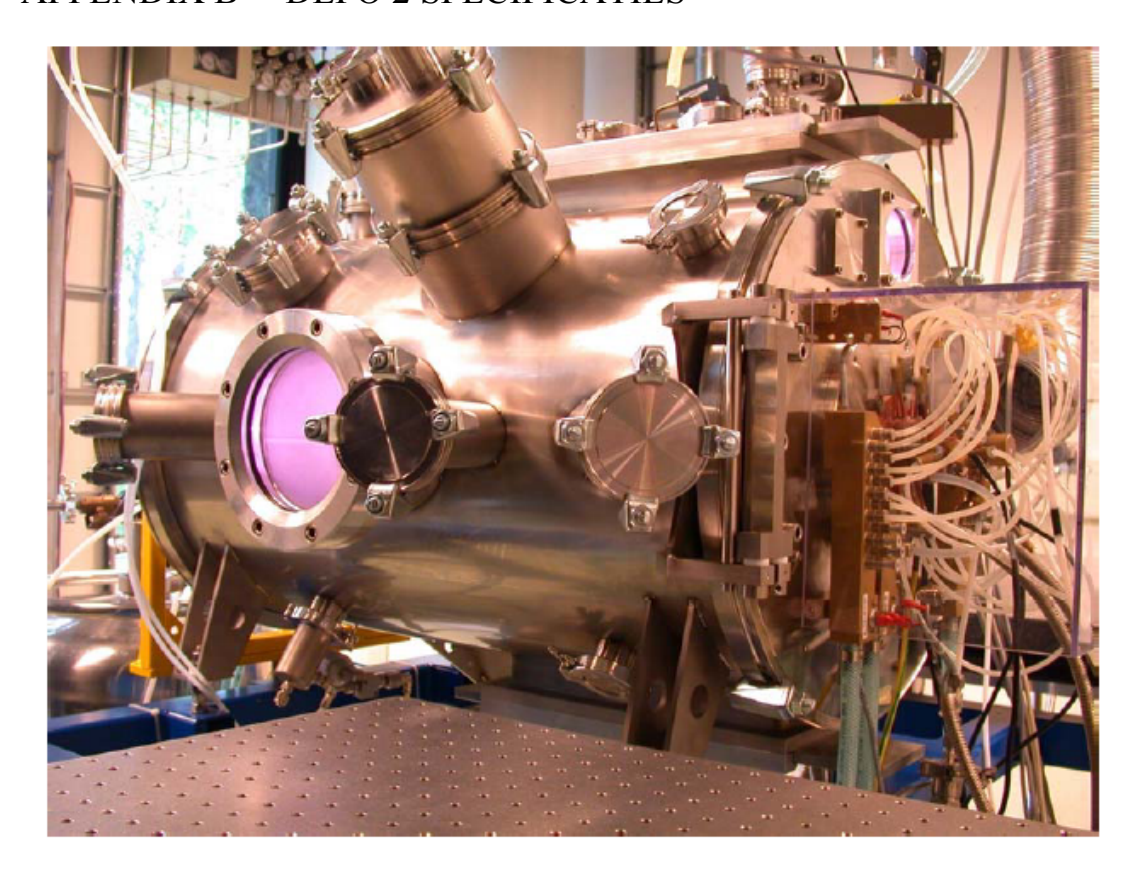
I.J. Houston *et al*. Thin Solid Films

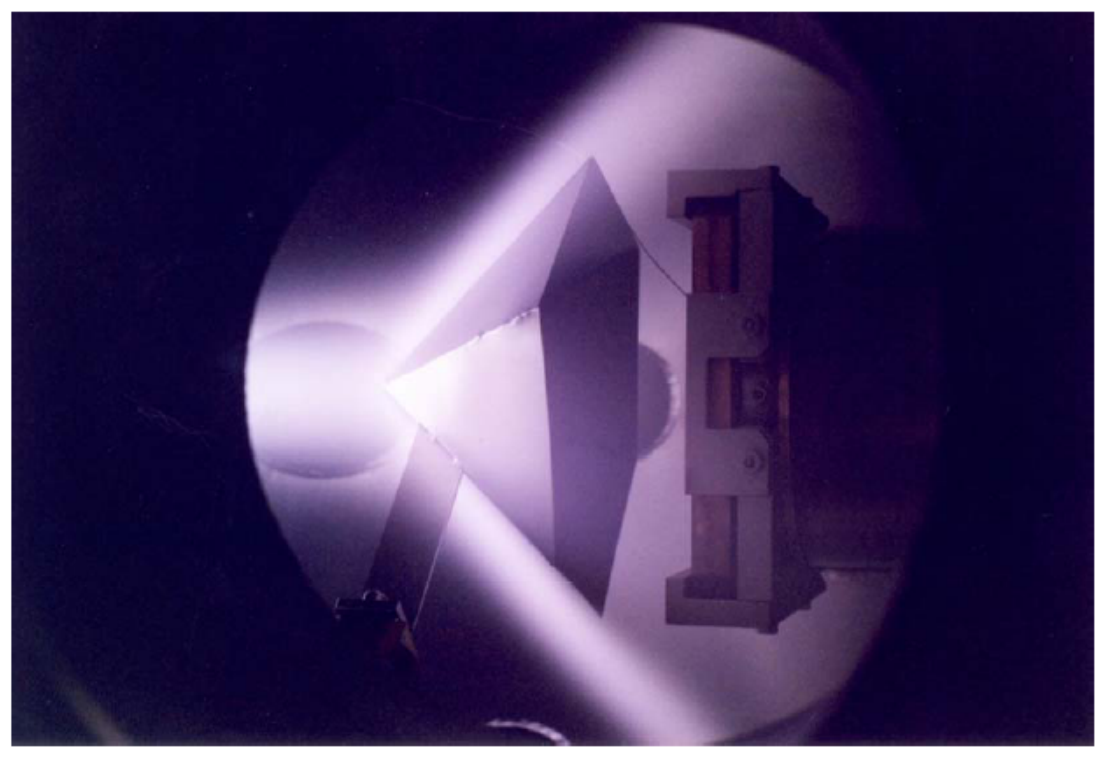
Figure 11 of 11



I.J. Houston *et al*. Thin Solid Films

# APPENDIX B DEPO 2 SPECIFICATIES





#### Algemeen:

De aansturing van de opstelling is compleet computer based. Een PLC (Siemens Siteop 10) met externe 24 V voeding controleert en beveiligt de opstelling. De gebruikte software is Wonderware Intouch in combinatie met de Wonderware window viewer. In Fig. 1 is een schematische weergave van de opstelling gegeven. Grofweg kunnen we de volgende onderdelen onderscheiden (indeling gebaseerd op groepen indeling uit aansturingsprogramma):

- plasmabron
- gas systeem
- reactor
- turbo reactor
- roots reactor
- turbo loadlock
- loadlock

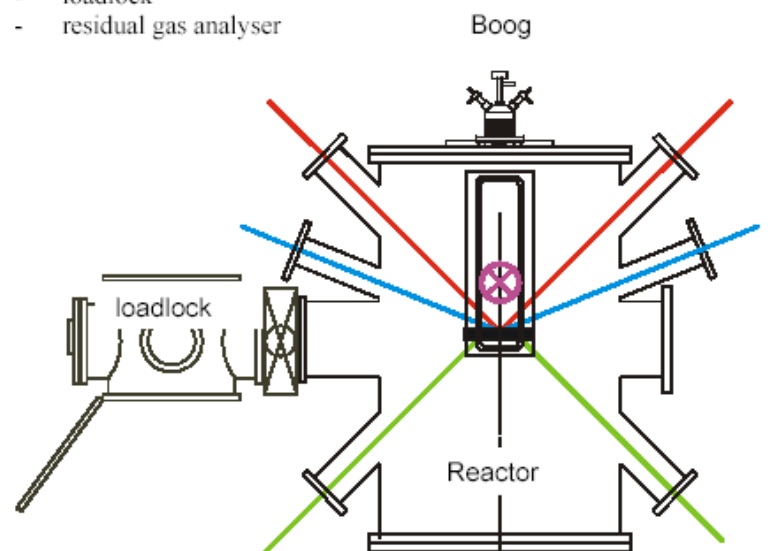


Fig. 1: Bovenaanzicht van de opstelling. Getekend zijn het reactor vat, het loadlock, de boog en de vier verschillende optische toegangen (rood, blauw, groen en loodrecht op het vlak van tekening paars).

#### Plasmabron:

- Diameter kanaal 4 mm
- 4 koperen cascade platen
- O-ringen voor vacuum afsluiting
- 3 cathode tips W/La (2%)
- Waterkoeling voor cascade platen en cathodehuis uitgevoerd met een snelkoppelingsysteem dat makkelijk demonteren en monteren mogelijk maakt
- Diverse nozzle designs, met en zonder nozzle injectie mogelijkheid
- Drukmeter in de gasleiding naar de boog
- Typische spanning 40-70 V afhankelijk van de gebruikte gassen
- Stroom: 12.5 25 A per cathode (Typisch 15 A)
- Veiligheidscover van perspex gekoppeld aan besturingsysteem van de opstelling (zonder cover is het niet mogelijk de boog aan te zetten)

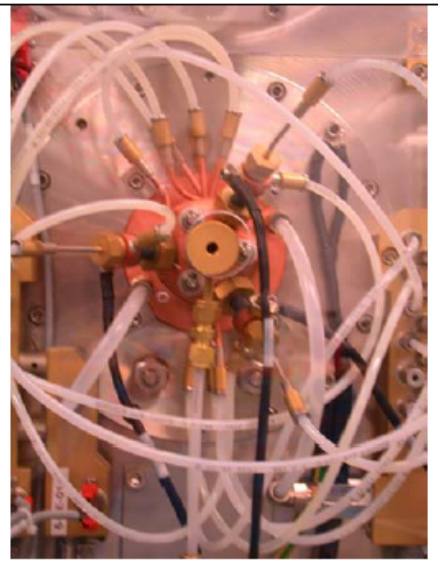


Fig. 2: Foto van de cascade boog.

#### Gassysteem:

Alle gasleidingen zijn volledig uitgevoerd in RVS.

Bronkhorst El-Flow® Digital Mass Flow Controllers (MFC) met profibus aansturing voor Ar, H<sub>2</sub>, D<sub>2</sub>, N<sub>2</sub>, O<sub>2</sub>

Bronkhorst Digital Low ΔP Mass Flow Controllers (MFC) met profibus aansturing voor SiH<sub>4</sub>, NH<sub>3</sub>, CF<sub>4</sub>

Gassen kunnen geinjecteerd worden op drie verschillende plaatsen:

- Cascade boog:
  - ◆ Ar (0.1..5 slm)
  - H<sub>2</sub> (0.04..2 slm)
  - D₂ (0.04..2 slm)
  - N₂ (0.02..1 slm)
- 2. Injectie ring:
  - SiH<sub>4</sub> (0.02..1 slm)
  - H<sub>2</sub> (0.04..2 slm)
  - D<sub>2</sub> (0.04..2 slm)
  - ← CF<sub>4</sub> (0.02..1 slm)

#### Via bypass:

- O₂ (0.02..1 slm)
- NH₃ (0.02..1 slm)
- 3. Injectie nozzle:
  - O₂ (0.02..1 slm)
  - NH₃ (0.02..1 slm)

#### Via bypass:

- SiH<sub>4</sub> (0.02..1 slm)
- H<sub>2</sub> (0.04..2 slm)
- D₂ (0.04..2 slm)
- CF<sub>4</sub> (0.02..1 slm)

He backflow (0.01..0.5 slm)

#### Reactor

Substraat houder en substraat temperatuur controle:

De maximale afmetingen van een substraat, zodat het nog op de houder past, is  $10 \times 10 \text{ cm}^2$ . Meestal worden echter drie samples van  $2.5 \times 2.5 \text{ cm}^2$  op de substraat houder bevestigd. Het juk voor de substraat houder bevat een nauwkeurige temperatuur controle, die bestaat uit  $4 \times 250 \text{ W}$  verwarmingselementen en een vloeibare stikstof leiding voor de koeling, waardoor de depositie temperatuur goed gecontroleerd kan worden. Een helium backflow draagt zorg voor een goed thermisch contact tussen juk en substraathouder en tussen substraat houder en sample. Deze temperatuur controle is geverifieerd middels een directe meting op het sample substraathouder interface. De resultaten hiervan zijn samengevat in Fig 2. In het verleden is een uitgebreide controle van de substraat temperatuur onder plasma condities uitgevoerd en de afwijkingen in de sample temperatuur zijn kleiner dan 15 °C voor alle condities (Kessels *et al.* JVSTA, 20 (5), 1704-1715, 2002).

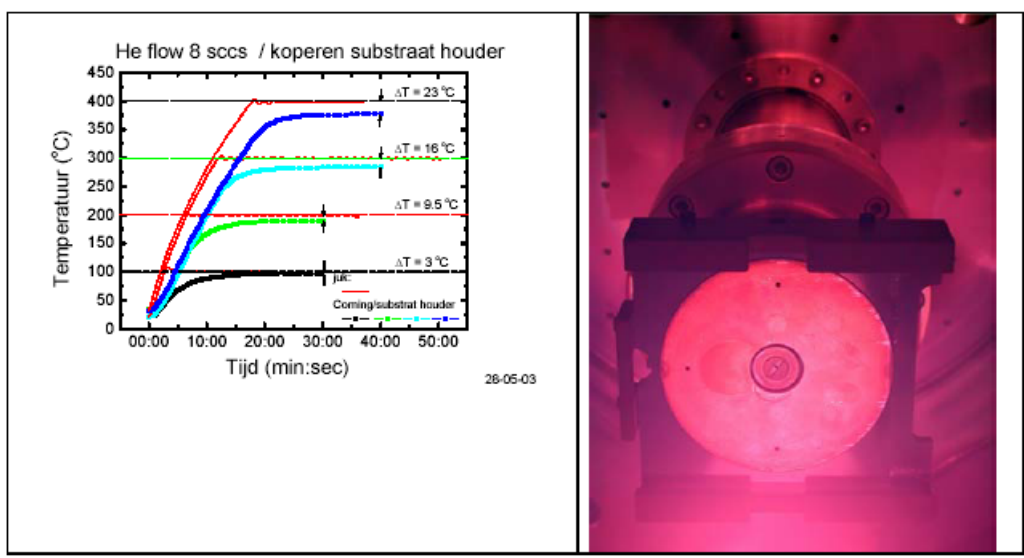


Fig. 3: (a) Verificatie van de temperatuur controle van de opstelling. De temperatuur van het corning sample is gemeten middels een thermokoppel dat is ingeklemd tussen de substraathouder en het corning. Er is gebruik gemaakt van een helium backflow van 8 sccs. (b) Foto van het juk. Hierin wordt de substraathouder met substraaten vast gezet.

#### Optische toegang:

90 graden: \* bv. Emissie spectroscopie

70 graden: \* bv. Spectroscopische Ellipsometrie

45 graden: \* bv. Attenuated Total internal Reflection Fourier Transform Infrared spectroscopie

Kan tegelijk met Spectroscopische Ellipsometrie worden uitgevoerd.

0 graden: \* verticaal, verschuifbaar over de as van de cascade boog naar het substraat toe

by. Cavity Ringdown Spectroscopie en probe metingen

#### Automatische shutter:

Het systeem beschikt over een automatische shutter die het substraat beschermt tijdens het opstarten van de cascade boog. Bovendien draagt de shutter zorg voor een nauwkeurige controle over de depositie tijd.



#### Drukmeters:

Pfeiffer PKR 251 Full range MKS baratrons 122a 0-10 mbar MKS baratron 127a 0-1000 mbar

Rf biasing:

Mogelijkheid tot het aanleggen van een rf bias op de substraathouder. Een rf schild zorgt ervoor dat het merendeel van het rf vermogen aan de voorkant van de substraathouder wordt afgegeven.

#### Turbo reactor:

Pfeiffer Duo 10 voorpomp Pfeiffer TIC 520 turbopomp controller met profibus aansturing Pfeiffer TMH 521 turbo pomp (300 l/s)

Onder normale condities is de einddruk in het reactor vat met deze pomp < 10.6 mbar.

#### Roots reactor:

Twee roots blowers met een eentraps voorpomp.

Leybold Trivac D65B

Pomp capaciteit (volgens fabrikant): 65 m3h-1

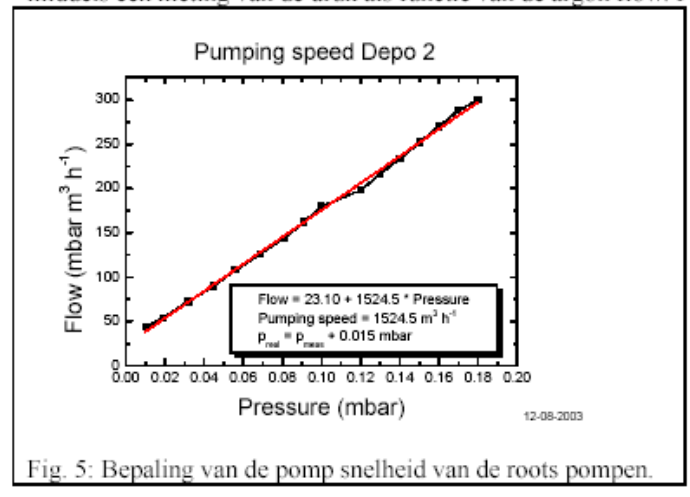
Pfeiffer WKP 500 SP

Pomp capaciteit (volgens fabrikant): 500 m3h-1

3. Edwards EH2600 rootsblower

Pomp capaciteit (volgens fabrikant): 1900 m3h-1

Voor de effectieve pompsnelheid geldt de volgende relatie: Q = S p. Hierin is Q de gas belasting [mbar  $m^3 h^{-1}$ ], S de pomp snelheid  $[m^3 h^{-1}]$  en p [mbar] de druk is. De effectieve pomp snelheid is bepaald middels een meting van de druk als functie van de argon flow. Fig. 5 laat het resultaat zien:



De effectieve pompsnelheid is 1525 m<sup>3</sup> h<sup>-1</sup>. Tevens zien we een off-set in de drukmeter van 0.015 mbar.

Onder normale condities is de einddruk in het reactor vat met deze pompen < 10<sup>-4</sup> mbar.

#### Turbo Loadlock:

Edwards RV8 voorpomp Pfeiffer TCP 200 controller Pfeiffer TPH 200 Turbo pomp (200 1/s)

#### Loadlock:

Het loadlock is uitgerust met een aparte turbopomp met voorpomp en kan in korte tijd afgepompt worden naar lage druk (p < 10<sup>-5</sup> mbar) omdat het volume van het loadlock klein is. Middels een magnetische schuif arm kan een substraat houder onder vacuüm condities ingeluisd worden in de reactor.

#### Massa spectrometer

De opstelling is standaard uitgerust met een Residual Gass Analyser (RGA), die middels een klep of een pinhole met het reactor vat verbonden is. Met deze RGA word iedere meetdag de kwaliteit van het vacuum gemonitored.

Technische gegevens:

Balzers Prisma 200 Quadrupool RGA

Uitgerust met:

- Edwards RV3 voorpomp
- Pfeiffer TCP 015 Turbo pomp controller
- Balzers TMU 065 Turbo pomp

#### Procedures:

Verwisselen van substraten middels het loadlock:

- 1. Pomp zowel de reactor als het loadlock met de turbo pomp totdat de druk p < 10<sup>-5</sup> mbar.
- Open de klep tussen reactor en loadlock (Turbo reactor blijft pompen)
- 3. Verschuif de substraat houder van de reactor naar het loadlock
- 4. Sluit de klep tussen reactor en loadlock
- 5. Belucht het loadlock
- 6. Verwissel de substraathouder
- 7. Pomp het loadlock weer af tot  $p < 10^{-5}$  mbar
- 8. Open de klep tussen loadlock en reactor (Turbo reactor blijft pompen)
- Verschuif de substraat houder van loadlock naar reactor
   Sluit de klep tussen loadlock en reactor
- 11. Zet de turbo van het loadlock weer aan

#### Depositie procedure:

- 1. Zet de substraat temperatuur op de gewenste depositie temperatuur en wacht tot deze zich heeft gestabiliseerd (zie substraat temperatuur controle)
- 2. Zet de shutter voor de substraat houder
- 3. Start de cascade boog op 55 sccs Argon en 45 A stroom
- 4. Voeg andere gassen toe via boog, ring of nozzle
- 5. Stel de timer in op de gewenste depositie tijd en start de depositie (shutter gaat automatisch open
- 6. Stop de cascade boog
- 7. Zet alle gaskleppen dicht